Japanese Journal of Applied Physics **54**, 04DH05 (2015) **REGULAR PAPER**
http://dx.doi.org/10.7567/JJAP.54.04DH05

# Influence of rhenium on the structural and optical properties of molybdenum disulfide

Mula Sigiro[1], Ying-Sheng Huang[1]*, Ching-Hwa Ho[2]*, Yung-Chang Lin[3], and Kazu Suenaga[3]

[1]*Department of Electronic and Computer Engineering, National Taiwan University of Science and Technology, Taipei 106, Taiwan*
[2]*Graduate Institute of Applied Science and Technology, National Taiwan University of Science and Technology, Taipei 106, Taiwan*
[3]*National Institute of Advanced Industrial Science and Technology (AIST), Tsukuba, Ibaraki 305-8565, Japan*
E-mail: ysh@mail.ntust.edu.tw; chho@mail.ntust.edu.tw

Received August 22, 2014; revised October 9, 2014; accepted November 4, 2014; published online February 10, 2015

We report on the extensive structural and optical studies of Re-doped molybdenum disulfide ($MoS_2$) grown by the chemical vapor transport (CVT) method using $Br_2$ as a transport agent. To evaluate the influence of Re on the structural properties of crystals, we have conducted X-ray diffraction (XRD) and transmission electron microscopy (TEM) experiments. For optical characterization, we carried out piezoreflectance (PzR) and electrolyte electroreflectance (EER) measurements. The Re dopant clearly caused a structural change in $MoS_2$ from a two-layer hexagonal (2H) structure to a three-layer rhombohedral (3R) structure, which has been clearly verified and identified herein.


## 1. Introduction

Molybdenum disulphide belongs to the family of transition-metal dichalcogenides,[1)] $MX_2$ where M = Mo or W and X = S or Se. In particular, the as-crystallized two-dimensional layered-type structure can impart substantial anisotropy to most of the physical properties of these compounds and has attracted investigators aiming to acquire a better insight into the fundamental physics of these compounds.[1–3)] The materials have also been extensively investigated because of their possible practical applications such as efficient electrodes in photoelectrochemical solar cells,[4–6)] catalysts in industrial applications and in secondary batteries,[7–9)] and solid-state lubricants.[10–12)] The successful application of this semiconductor compound originates largely from its sandwich interlayer structure, loosely bound by the weak van der Waals forces, as evidenced by easy cleavage perpendicular to the *c*-direction along which the S–Mo–S layers are stacked to form a crystal. There are two known polytypes of $MoS_2$;[1,13)] two-layer hexagonal and three-layer rhombohedral termed 2H and 3R, respectively. Naturally occurring 3R-$MoS_2$ has been found to be consistently rich in certain minor elements such as Re and Nb.[14)] The incorporation of the impurity elements will essentially influence the structural symmetry of $MoS_2$, that is, the adoption of the polytype 3R-$MoS_2$. Zelikman et al. reported that the 3R modification of $MoS_2$ is a result of substitution of some part of the Mo atoms by Re in the $MoS_2$ lattice, which made the three layer 3R packing more stable than the two-layer 2H polytype.[15)] In the previous work, we investigated the electrical properties of Re-doped $MoS_2$ by temperature-dependent resistivity and Hall coefficient measurements; the optical absorption measurements indicated that Re-doped $MoS_2$ is an indirect semiconductor and its energy gap shows a red-shift with increasing dopant concentration.[16)] Herein, we have also undertaken a series of experiments to analyze the structural and optical properties of undoped and Re-doped $MoS_2$.

In this study, both $MoS_2$ samples with and without the Re dopant were prepared by the chemical vapor transport (CVT) method. To determine the structural and optical properties of both samples, X-ray diffraction (XRD), scanning transmission electron microscopy (STEM), piezoreflectance (PzR), and electrolyte electroreflectance (EER) measurements were carried out. A series of experimental results confirmed the Re dopant effect on the fundamental material properties, which could provide guidance for further electronics and optoelectronics production of $MoS_2$.

## 2. Experimental methods

Single crystals of the Re-doped $MoS_2$ were grown by the CVT method with $Br_2$ as a transport agent. The total charge used in each growth experiment was about 10 g. A stoichiometrically determined weight of the doping material was added in the hope that it would be transported at a rate similar to that of Mo. Before the crystal growth, the powdered compounds were prepared from the elements by reaction at 1,000 °C for 10 days in an evacuated quartz ampoule. Prior to the crystal growth, a quartz ampoule (22 mm OD, 17 mm ID, 20 cm length) containing $Br_2$ ($\sim$5 mg/cm$^3$) and the elements (purity: Mo, 99.99%; Re, 99.99%; S, 99.999%) was evacuated to $10^{-6}$ Torr and sealed. It was shaken well for uniform mixing of the powder. The ampoule was placed in a three-zone furnace and the charge prereacted for 24 h at 800 °C with the growth zone at 950 °C, preventing the transport of the product. The temperature of the furnace was increased slowly. The slow heating was necessary to avoid any possibility of explosion due to exothermic reaction between the elements. The furnace was then equilibrated to give a constant temperature across the reaction tube and programmed over 24 h to produce the temperature gradient at which single crystal growth took place. Optimal results were obtained with the temperature gradient of approximately 960 → 930 °C. After 240 h, the furnace was allowed to cool slowly (40 °C/h) to about 200 °C. The ampoule was then removed and wet tissues were applied rapidly to the end away from the crystals to condense the $Br_2$ vapor. When the ampoule reached room temperature, it was opened and the crystals were removed. The crystals were then rinsed with acetone and deionized water. Single crystalline platelets up to 10 × 10 mm$^2$ in surface area and 2 mm in thickness were obtained.

XRD patterns of single crystals were obtained using a Rigaku RTP300RC X-ray with Ni-filtered Cu K$\alpha$ radiation ($\lambda$ = 1.5418 Å), and a silicon standard was used to calibrate the diffractometer. The morphologies of the samples were investigated by STEM at a high magnification. A JEOL 2100F STEM equipped with a delta corrector and a cold field

 

emission gun was employed at 60 kV in these experiments. Single-layer and few-layer Re-doped $MoS_2$ samples were mechanically exfoliated from the CVT synthesized crystals using scotch tape and transferred onto a silicon substrate with 300 nm thermal oxide. The surfaces of Re-doped $MoS_2$/$SiO_2$/Si samples were spin coated with 1.5-μm-thick polycarbonate (1 wt % dissolved in chloroform). The single-layered Re-doped $MoS_2$ flakes were transferred from the $SiO_2$ surface to the TEM microgrid (quantifoil) using 2-propanol and cleaned using chloroform for 12 h before the TEM observation. Then, the specimens were cleaned by baking in air at 200 °C for 10 min, after which they were placed in the TEM chamber. The JEOL double tilt holder was precleaned using ion-plasma cleaner (JEOL, operated at 360 V for 10 min) after ethanol treatment. The vacuum level in the TEM chamber was $\sim 1.7 \times 10^{-5}$ Pa.

The experimental setup for the PzR measurements has been described elsewhere.[17,18)] Our systems were prepared by gluing the thin single crystal specimen onto a 0.15-cm-thick lead–zirconate–titanate (PZT) piezoelectric transducer driven by a 200 $V_{rms}$ sinusoidal wave at 200 Hz. The alternating expansion and contraction of the transducer subjects the sample to an alternating strain with a typical rms $\Delta l/l$ of $\sim 10^{-5}$. A 150 W tungsten–halogen lamp filtered using a McPherson 0.35 m monochromator provided the monochromatic light. The reflected light was detected by an EG&G HUV-2000B silicon photodiode. The DC output of the silicon photodiode was maintained constant by the servo mechanism of a variable neutral density filter. A dual-phase lock-in amplifier was used to measure the detected signal. Modulated spectra were normalized to the reflectance to obtain $\Delta R/R$. An RMC 22 closed-cycle cryogenic refrigerator equipped with a model 4075 digital thermometer controller was used to control the measurement temperature between 25 and 300 K with a temperature stability of 0.5 K or better.

For the EER experiment, maximum-size crystals of 1% Re-doped $MoS_2$ were selected. The EER measurements were taken on a fully computerized setup for modulation spectroscopy described elsewhere.[17,19,20)] Detailed investigations of the polarization dependence of the prominent features, A and B excitons in the energy range of 1.75–2.25 eV, were undertaken. For the Re-doped $MoS_2$, the spectra were recorded for the perpendicular ($E \perp c$) and parallel ($E \parallel c$) polarizations together with an unpolarized spectrum for the $k \perp c$ (edge plane) configuration, whereas only the unpolarized spectrum was recorded for the $k \parallel c$ (van der Waals plane) configuration. For the undoped $MoS_2$, only the $k \parallel c$ and unpolarized spectrum was taken. The detector response to the DC component of the reflected light is kept constant by either an electronic servo mechanism or a neutral density filter so that the AC reflectance corresponds to $\Delta R/R$, the differential reflectance. Scans of $\Delta R/R$ versus wavelength were obtained using a 0.35 m McPherson grating monochromator together with an Oriel 150 W xenon arc lamp as a monochromatic light source. Phase-sensitive detection was carried out to measure the differential reflectance. The electrolyte was a 1 N $H_2SO_4$ aqueous solution, and the counter-electrode was a 5 $cm^2$ platinum plate. A 200 Hz 100 mV peak-to-peak square wave with $V_{DC} = 0$ V versus a platinum electrode was used to modulate the electric field in the space charge region of the $MoS_2$ electrode.

## 3. Results and discussion

Figure 1 reveals the XRD patterns of doped and undoped $MoS_2$ single crystals. The relative intensity and resolution of observed peaks change for the Re-doped sample. For Re-doped crystals, the observed peaks correspond to the rhombohedral structure (3R) crystal with the cell dimension of $a = 3.164$ Å and $c = 18.371$ Å, whereas for the undoped crystal, the patterns correspond to the hexagonal structure (2H). The lines were identified with a 3R in which, by referring to the 2H, the $a$ parameter of the unit cell is similar to that of the 3R ($a = 3.160$ Å) but the $c$ parameter was about 1.5 times larger than that of that 2H ($c = 12.295$ Å). We observed that the $a$ parameter remains unchanged for the undoped and Re-doped samples, whereas the $c$ parameter shows an appreciable increase, which is in agreement with the increase in the $d$-spacing.

In Figs. 2 and 3, the STEM images of Re-doped $MoS_2$ crystals are presented. It is clearly seen that Re atoms tend to occupy or substitute Mo atoms in the host $MoS_2$ lattice. The Re dopants are well dispersed in $MoS_2$ layers and show no formation of clusters in the host material.[21)] The observed doping concentration of ~1% Re is in agreement with the synthesis condition. About 7% of the Re dopants were found as adatoms. Those Re adatom dopants on $MoS_2$ can become mobile by receiving kinetic energy ($E_k$) from the focused incident electron beam. The energy transferred from the 60 kV electron beam to Re atoms is $E_k = 0.75$ eV.[22–24)] In this case, substitution to the Mo site has the lowest formation energy by a large margin. Among the adatom sites, the position on the top of Mo is favored. This is in good agreement with the observations that nearly all Re atoms are located at Mo sites, and rarely on the adatom sites on top of Mo and S. The way the Re atoms moved has been discussed in more detail in our previous work.[24)]

The PzR spectra near the direct band edge over the range of 1.7–2.3 eV for the undoped and Re-doped $MoS_2$ single crystals are respectively shown in Figs. 4(a) and 4(b). The spectra are characterized by observing two prominent excitonic transitions, A and B. In the case of undoped $MoS_2$, a higher-series A exciton, denoted as $A_2$, is also detected. The dashed lines in Fig. 4 are the experimental PzR spectra and the solid curves are the least-square fits to a derivative Lorentzian functional form appropriate for the interband transitions expressed as[17,19)]

$$\frac{\Delta R}{R} = \mathrm{Re}\left[\sum_{i=1}^{m} A_i^{ex} e^{j\varphi_i^{ex}} (E - E_i^{ex} + j\Gamma_i^{ex})^{-2}\right], \qquad (1)$$

where $A_i^{ex}$ and $\varphi_i^{ex}$ are the amplitude and phase of the line shape, and $E_i^{ex}$ and $\Gamma_i^{ex}$ are the energy and broadening parameters of the interband excitonic transitions, respectively. For the first derivative functional form, the exponential term 2.0 is appropriate for the bound states, such as excitons or impurity transitions.[19)] The fits yield the parameters $A_i$, $E_i$, and $\Gamma_i$. The obtained values of $E_i$ are indicated as arrows and denoted as $A_1$, $A_2$, and B. The nomenclature was commonly used previously by Wilson and Yoffe,[1)] Beal et al.,[25)] and Fortin and Raga.[3)] The fitted values of $E_i$ are listed in Table I together with some of the values from previous works.[3,25–28)] The energies of prominent A and B excitons of 3R are observed to be lower than those of the 2H undoped $MoS_2$.

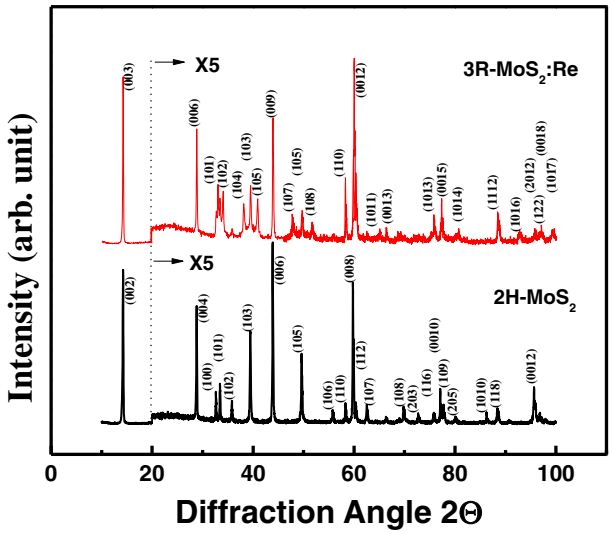


**Fig. 1.** (Color online) XRD patterns of the undoped and Re-doped $MoS_2$ single crystals.

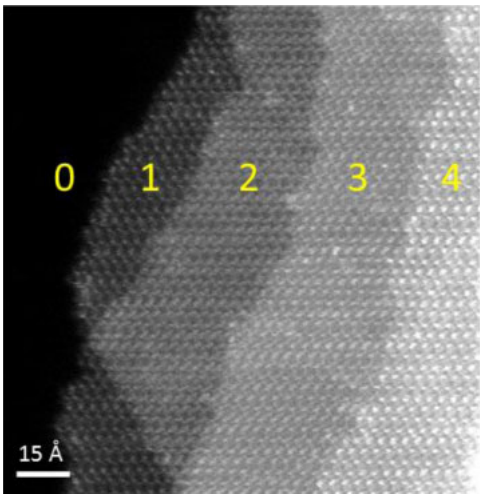


**Fig. 2.** (Color online) Low magnification annular dark-field STEM image of Re-doped few-layer stacked $MoS_2$ flakes, where the atomic element arrangements and the number of $MoS_2$ layers can be clearly distinguished by the *Z*-contrast. The numbers 0, 1, 2, 3, and 4 correspond to the number of layers.

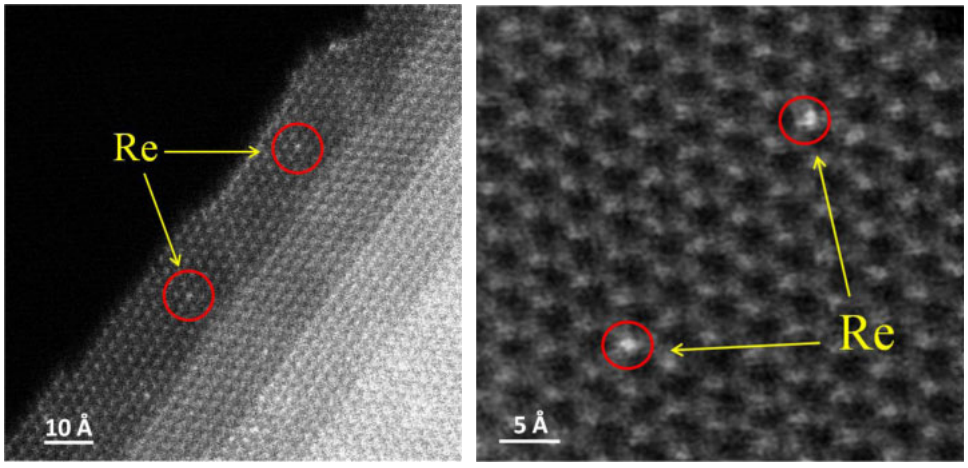


**Fig. 3.** (Color online) ADF-STEM image of Re atoms tending to occupy Mo atoms.

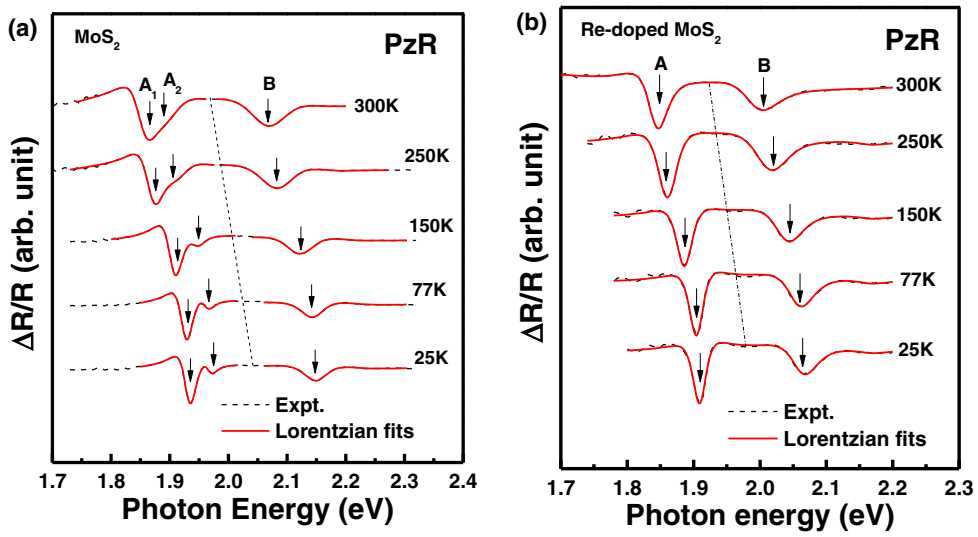


**Fig. 4.** (Color online) Piezoreflectance spectra of (a) undoped and (b) Re-doped $MoS_2$ at several temperatures between 25 and 300 K. The dashed curves are the experimental results, and the solid curves are the least-squares fits of Eq. (1).

**Table I.** Energies of excitons A and B for the undoped and Re-doped $MoS_2$. The corresponding values in previous reports are included.

| Material | $E_{A_1}$ (eV) | $E_{A_2}$ (eV) | $E_B$ (eV) | Temperature (K) |
|---|---|---|---|---|
| Undoped $MoS_2$[a)] | $1.932 \pm 0.005$ | $1.970 \pm 0.005$ | $2.148 \pm 0.008$ | 25 |
| | $1.927 \pm 0.005$ | $1.966 \pm 0.005$ | $2.144 \pm 0.008$ | 77 |
| | $1.853 \pm 0.008$ | $1.903 \pm 0.008$ | $2.070 \pm 0.008$ | 300 |
| Re-doped $MoS_2$[a)] | $1.910 \pm 0.005$ | | $2.068 \pm 0.008$ | 25 |
| | $1.905 \pm 0.005$ | | $2.062 \pm 0.008$ | 77 |
| | $1.846 \pm 0.008$ | | $2.004 \pm 0.008$ | 300 |
| Re-doped $WS_2$[b)] | $2.039 \pm 0.002$ | | $2.454 \pm 0.003$ | 15 |
| | $1.958 \pm 0.005$ | | $2.340 \pm 0.008$ | 300 |
| Undoped $MoS_2$[c)] | $1.929 \pm 0.005$ | | $2.136 \pm 0.008$ | 25 |
| | $1.845 \pm 0.008$ | | $2.053 \pm 0.010$ | 300 |
| $MoS_2$[d)] | 1.88 | | 2.06 | 300 |
| $MoS_2$[e)] | 1.9255 | | 2.137 | 4.2 |
| $MoS_2$[f)] | 1.92 | | 2.124 | 4.2 |
| 2H-$MoS_2$[g)] | 1.910 | | 2.112 | 5 |
| 3R-$MoS_2$[g)] | 1.908 | | 2.057 | 5 |

a) Present work. b) Ref. 28 (PzR). c) Ref. 27 (PzR).
d) Ref. 26 (reflectance). e) Ref. 3 (WMR). f) Ref. 3 (photoconductivity).
g) Ref. 25 (transmission).

The energy separations between A and B excitons ($\Delta_{BA} = E_B - E_A$) are $152 \pm 5$ meV for Re-doped $MoS_2$ and $212 \pm 8$ meV for undoped $MoS_2$. The Re incorporation can reduce the energy separation between A and B excitons. The linewidth of the exciton B is much broader than that of exciton A. The A exciton originates from the valence-band top whereas the B exciton comes from the valence-band splitting. In general, the Rydberg series of the A and B excitons of undoped $MoS_2$ can be described by three-dimensional Mott–Wannier excitons,[25,26,29)] as $E_n = E_\infty - Rn^{-2}$, where $n = 1, 2, 3, \ldots$, and $E_\infty$ and $R$ are the critical and binding energies, respectively. For Re-doped $MoS_2$, only $n = 1$ Rydberg series for both excitonic transitions are observed. It has been shown that excitons for the 3R $MoS_2$ are more appropriately described by the two-dimensional Mott–Wannier excitons.[25,26,29)] The absence of higher-order series is an inherent nature of the two-dimensional Mott–Wannier excitons.[26)] From more recent theoretical and experimental studies,[30,31)] the A and B excitons are attributed to the smallest direct transitions at the $K$ point of the Brillouin zone split by interlayer interaction and spin–orbit splitting. The A exciton belongs to $K_4$ to $K_5$ optical transition whereas the B exciton corresponds to $K_1$ to $K_5$ optical transition. The $K$ states have been shown to be predominantly determined by the metal $d$ states with a small contribution from the non-metal $p$ states.[30,31)] The energies and linewidths of A and B excitons can be determined accurately by using the fits of Eq. (1). When the temperature increased, both excitonic transitions showed energy reduction which is a general semiconductor behavior. The linewidths also become broadened in the process. The temperature-dependent variations of the energies of A and B excitons for the undoped and Re-doped $MoS_2$ are shown in Fig. 5. The dashed curves in Fig. 5(a) are the least-squares fits to the Varshni-type equation:[32)]

$$E_i(T) = E_i(0) - \frac{\alpha_i T^2}{\beta_i + T}, \tag{2}$$

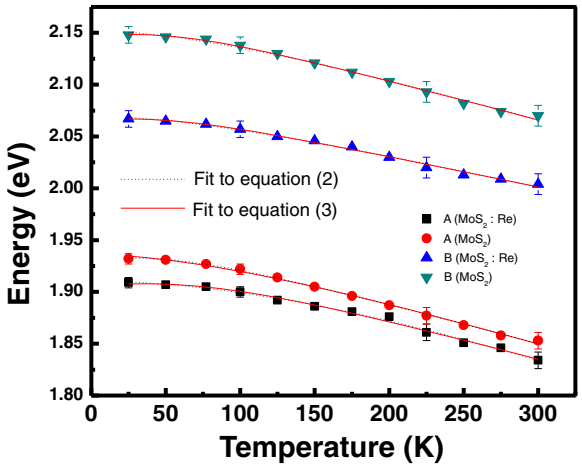


**Fig. 5.** (Color online) Temperature-dependent variations of the energies of the A–B excitonic pair for undoped and Re-doped $MoS_2$. Representative error bars are shown. The dashed and solid curves are least-squares fits to Eqs. (2) and (3), respectively.

where $i =$ A or B, $E_i(0)$ is the transition energy at 0 K, and $\alpha_i$ and $\beta_i$ are the Varshni coefficients. The constant $\alpha_i$ is related to the electron (exciton)–phonon interaction and $\beta_i$ is closely related to the Debye temperature. For the undoped sample, the fitted values for exciton A are $E(0) = 1.935 \pm 0.005$ eV, $\alpha = 0.47 \pm 0.05$ meV K$^{-1}$, and $\beta = 148 \pm 45$ K; and for exciton B, they are $E(0) = 2.151 \pm 0.005$ eV, $\alpha = 0.46 \pm 0.05$ meV K$^{-1}$ and $\beta = 188 \pm 45$ K, whereas for the Re-doped $MoS_2$, the fitted values for exciton A are $E(0) = 1.917 \pm 0.005$ eV, $\alpha = 0.43 \pm 0.05$ meV K$^{-1}$, and $\beta = 170 \pm 45$ K; and for exciton B they are $E(0) = 2.071 \pm 0.005$ eV, $\alpha = 0.43 \pm 0.05$ meV K$^{-1}$, and $\beta = 185 \pm 45$ K.

The temperature dependence of excitonic transition energies $E_A(T)$ and $E_B(T)$ of the undoped and Re-doped $MoS_2$ can also be analyzed (solid curves in Fig. 5) by using another expression containing the Bose–Einstein occupation factor for phonons[33,34)]

$$E_i(T) = E_{iB} - a_{iB}\left[1 + \frac{2}{\exp(\Theta_{iB}/T) - 1}\right], \tag{3}$$

where $i =$ A or B, $a_{iB}$ represents the strength of the electron (exciton)–phonon interaction, and $\Theta_{iB}$ corresponds to the average phonon temperature. For the undoped sample, the fitted values for exciton A are $E_{AB} = 1.932 \pm 0.01$ eV, $a_{AB} = 40 \pm 15$ meV, and $\Theta_{AB} = 180 \pm 65$ K; and for exciton B, they are $E_{BB} = 2.148 \pm 0.01$ eV, $a_{BB} = 41 \pm 15$ meV, and $\Theta_{BB} = 190 \pm 65$ K, whereas for the Re-doped samples, the fitted values for exciton A are $E_{AB} = 1.905 \pm 0.01$ eV, $a_{AB} = 42 \pm 15$ meV, and $\Theta_{AB} = 220 \pm 65$ K; and for exciton B $E_{BB} = 2.07 \pm 0.01$ eV, $a_{BB} = 40 \pm 15$ meV, and $\Theta_{BB} = 205 \pm 65$ K. The obtained values are typical of the layered-type transition metal dichalcogenides.[27,35–37)] The line-width broadening parameter of the A and B excitons can be analyzed by[33,34)]

$$\Gamma_i(T) = \Gamma_{i0} + \frac{\Gamma_{iLO}}{\exp(\Theta_{iLO}/T) - 1}, \tag{4}$$

where $i =$ A or B. The first term represents the broadening induced by temperature-independent mechanisms, such as impurity, dislocation, electron interaction, and Auger proc-

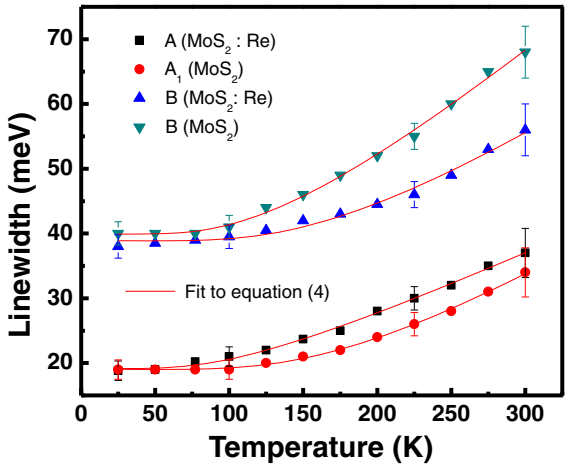


**Fig. 6.** (Color online) Temperature-dependent variations of the broadening parameters of A and B excitonic transitions for undoped and Re-doped $MoS_2$. Representative error bars are shown. The solid curves are the least-squares fits to Eq. (4).

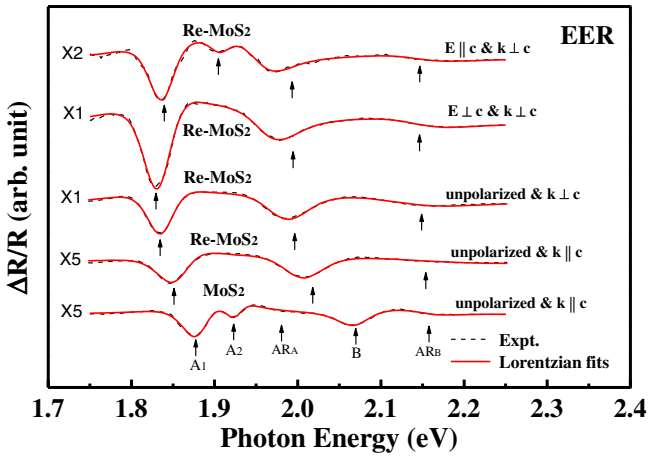


**Fig. 7.** (Color online) Polarization-dependent EER spectra of undoped and Re-doped $MoS_2$ over the range of 1.75 to 2.25 eV. The dashed curves are the experimental results, and the solid curves are the least-squares fits of Eq. (1).

esses, whereas the second term is caused by the Fröhlich interaction. The quantity $\Gamma_{i\mathrm{LO}}$ represents the strength of the electron (exciton)–LO phonon coupling, whereas $\Theta_{i\mathrm{LO}}$ is the LO phonon temperature. The solid curves in Fig. 6 represent least-squares fits to Eq. (4), which determine the values of $\Gamma_{i0}$, $\Gamma_{i\mathrm{LO}}$, and $\Theta_{i\mathrm{LO}}$ for the excitonic transitions. For the undoped $MoS_2$, the fitted values for exciton A are $\Gamma_0 = 18.3 \pm 1.0$ meV, $\Gamma_{\mathrm{LO}} = 77 \pm 20$ meV K$^{-1}$, and $\Theta_{\mathrm{LO}} = 562 \pm 50$ K; and for exciton B they are $\Gamma_0 = 37.6 \pm 2.0$ meV, $\Gamma_{\mathrm{LO}} = 76 \pm 30$ meV K$^{-1}$, and $\Theta_{\mathrm{LO}} = 562 \pm 50$ K, whereas for the Re-doped $MoS_2$, the fitted values for exciton A are $\Gamma_0 = 16.2 \pm 1.0$ meV, $\Gamma_{\mathrm{LO}} = 83 \pm 20$ meV K$^{-1}$, and $\Theta_{\mathrm{LO}} = 515 \pm 50$ K; and for exciton B they are $\Gamma_0 = 38.5 \pm 2.0$ meV, $\Gamma_{\mathrm{LO}} = 88 \pm 30$ meV K$^{-1}$, and $\Theta_{\mathrm{LO}} = 522 \pm 50$ K. These values are typical and similar to all of the layered structure transition metal dichalcogenides.[27,35–37]

Figure 7 shows the polarized and unpolarized EER spectra of undoped and Re-doped $MoS_2$ measured from the van der Waals plane or edge plane in the energy range of 1.75 to 2.25 eV. The EER spectrum of the undoped $MoS_2$ is displayed on the bottom of Fig. 7. Two bands, $E_{\mathrm{A1}} = 1.881$ eV and $E_{\mathrm{A2}} = 1.925$ eV, were detected for exciton A. The direct band gap $E_{\mathrm{g}} = 1.94$ eV and the exciton binding energy $R = 58.7$ meV can be estimated from the A exciton series.[25,26] These values are similar to those in Ref. 25. The features of $\mathrm{AR_A} = 1.986$ eV and $\mathrm{AR_B} = 2.15$ eV are identified to be those of the antiresonance structures.[25] For exciton B, the EER transition feature is much broadened and the energy is approximately 2.07 eV.

The top four curves in Fig. 7 are the EER spectra of the 1% Re-doped $MoS_2$ sample obtained on the edge plane [(1) $E \parallel c$ and $k \perp c$, (2) $E \perp c$ and $k \perp c$, and (3) unpolarized and $k \perp c$, from top] and on the basal plane [i.e., (4) unpolarized and $k \parallel c$ spectrum]. The higher bands (i.e., $A_2$, $\mathrm{AR_A}$, and $\mathrm{AR_B}$ observed in undoped $MoS_2$) in all the spectra of the Re-doped $MoS_2$ are absent. The energies of excitons A and B showed a decrease when the Re element was incorporated into the $MoS_2$. In particular, the reduction of ~65 meV for exciton B with the $k \parallel c$ configuration in Re-doped and undoped $MoS_2$ is identical to the separation of the feature labeled B* from exciton B of the WMR measurement in Ref. 3 where the same $k \parallel c$ configuration is employed. The presence of B* is attributed to the coexistence of 3R and 2H phases[3,15] in the synthetic crystals. In the $E \parallel c$ and $k \perp c$ spectrum, we have additionally detected one distinct structure of unknown origin located between excitons A and B at 1.906 eV. It is possibly closely related to the antiresonance feature such as $\mathrm{AR_A}$ that has been detected in the undoped $MoS_2$. In addition, the undoped and Re-doped $MoS_2$ in Fig. 7 also show that excitons A and B are respectively lowered by 27 and 65 meV for the Re-doped $MoS_2$. This is due to the presence of the rhenium impurity altering the original crystal symmetry of $MoS_2$. During the crystal growth of Re–$MoS_2$, rhenium ions can substitute Mo atoms in the $MoS_2$ lattice.[15] Consequently (by the interlayer interactions), the excitonic transitions with A–B energy separation of the spin orbit doublet can reduce from ~210 meV for undoped $MoS_2$ (i.e., 2H) to approximately 158 meV for the Re-doped $MoS_2$ (i.e., 3R). As shown in Fig. 7, the unpolarized spectra of $k \parallel c$ and $k \perp c$ configurations for Re-doped $MoS_2$ show that the measured energy difference between excitons A and B is identical (~158 meV) but the energy shift is about 21 meV. The ~21 meV energy shift is attributed to the crystal anisotropy.[38,39] The appearance of the measured crystal anisotropy for the Re-doped $MoS_2$ [i.e., measurements on the basal ($k \parallel c$) and edge ($k \perp c$) planes] is due to the fact that the incorporation of Re ions not only transforms the stacking structure from 2H to 3R but also pushes the layered sample to become thicker to form a large area of the edge (side) plane available for EER measurement. This evidence also supports the dopant effect of the Re ions in $MoS_2$ as previously described in STEM. Besides, the top two spectra in Fig. 7 from the edge plane (i.e., $k \perp c$) of $E \parallel c$ and $E \perp c$ polarizations showed $A_1 = 1.838$ and 1.833 eV, respectively. The broadened B exciton shows insensitivity (no energy shift) to the polarizations. A measured shift of 5 meV for $A_1$ can be consistently obtained by careful repetition of the measurements by $E \parallel c$ and $E \perp c$ operations on the edge plane. The unpolarized spectrum measured from the edge plane (i.e., unpolarized and $k \perp c$) can be regarded as a

random superposition of the two spectra, whose transition energy is determined to be $A_1 = 1.836$ eV in Fig. 7. The intralayer bonding of $MoS_2$ is partially ionic and partially covalent with the latter being dominant in the crystal.[40,41] The presence of Re atoms in the $MoS_2$ lattice enhances the ionicity of the metal–chalcogen bonding and also increases the lattice polarizability[40] in the Re-doped $MoS_2$. From the top-two EER spectra in Fig. 7, the $E \perp c$ spectrum demonstrates a more pronounced lattice field than that of the $E \parallel c$ spectrum to render a shift of 5 meV in exciton A. From all of the optical results of the EER measurements, the Re dopant surely substitutes the Mo atom in the Re–$MoS_2$ lattice. By the Re incorporation, the stacking structure of $MoS_2$ has thus been changed (2H → 3R), and the crystal polarizability and lattice iconicity have therefore been reconstructed.

## 4. Conclusions

We have demonstrated the synthesis of single crystals of undoped and Re-doped $MoS_2$ by the CVT method using $Br_2$ as a transport agent. XRD revealed the 3R structure of the Re-doped compound and 2H of the undoped one. Re atoms tend to occupy or substitute Mo atoms in the host $MoS_2$ lattice. Optical spectra were recorded to clarify the spectral features near the direct band-edge excitonic transitions and showed a splitting of approximately 150 meV between the A and B excitons for the 3R compound. The corresponding splitting is measured to be 200 meV for the 2H compound. The temperature dependence of the broadening function has also been interpreted in terms of a Bose–Einstein equation that contains the electron (exciton)–LO phonon coupling $\Gamma_{LO}$. The Re ions stabilize the formation of 3R-$MoS_2$. Re doping can strongly reduce the splitting between A and B excitons and cause their redshift in relation to the undoped $MoS_2$. The electronic states of the $MoS_2$ crystals are modified and affect the symmetry selection rules of the excitonic transitions.

## Acknowledgment

The authors would like to acknowledge the financial support by the National Science Council of Taiwan under Grant No. NSC 100-2112-M-011-001-MY3.

1) J. A. Wilson and A. D. Yoffe, Adv. Phys. **18**, 193 (1969).
2) L. F. Mattheiss, Phys. Rev. B **8**, 3719 (1973).
3) E. Fortin and F. Raga, Phys. Rev. B **11**, 905 (1975).
4) W. Kautek, H. Gerisch, and H. Tributsch, J. Electrochem. Soc. **127**, 2471 (1980).
5) K. K. Kam and B. A. Parkinson, J. Phys. Chem. **86**, 463 (1982).
6) S. J. Li, J. C. Bernède, J. Pouzet, and M. Jamali, J. Phys.: Condens. Matter **8**, 2291 (1996).
7) P. Grange and B. Delmon, J. Less-Common Met. **36**, 353 (1974).
8) P. G. Moses, B. Hinnemann, H. Topsøe, and J. K. Nørskov, J. Catal. **248**, 188 (2007).
9) C. T. Tye and K. J. Smith, Catal. Today **116**, 461 (2006).
10) J. M. Martin, C. Donnet, J. Le Mogne, and T. Epicier, Phys. Rev. B **48**, 10583 (1993).
11) S. D. Walck, J. S. Zabinski, N. T. McDevitt, and J. E. Bultman, Thin Solid Films **305**, 130 (1997).
12) L. Rapoport, V. Leshchinsky, I. Lapsker, Yu. Volovik, O. Nepomnyashchy, M. Lvovsky, R. Popovitz-Biro, Y. Feldman, and R. Tenne, Wear **255**, 785 (2003).
13) R. Murray and B. L. Evans, J. Appl. Crystallogr. **12**, 312 (1979).
14) A. H. Clark, Neues Jahrb. Mineral. Monatsh. **3**, 33 (1970).
15) A. N. Zelikman, G. V. Indenbaum, M. V. Teslitskaya, and V. P. Shalankova, Sov. Phys. Crystallogr. **14**, 687 (1970).
16) K. K. Tiong, P. C. Liao, C. H. Ho, and Y. S. Huang, J. Cryst. Growth **205**, 543 (1999).
17) F. H. Pollak and H. Shen, Mater. Sci. Eng. R **10**, 275 (1993).
18) H. Mathieu, J. Allegre, and B. Gil, Phys. Rev. B **43**, 2218 (1991).
19) D. E. Aspnes, in *Optical Properties of Semiconductors: Handbook on Semiconductors*, ed. M. Balkanski (North-Holland, Amsterdam, 1980) p. 109.
20) Y. S. Huang and F. F. Cheng, Phys. Rev. B **38**, 7997 (1988).
21) R. Zan, U. Bangert, Q. Ramasse, and K. S. Novoselov, J. Phys. Chem. Lett. **3**, 953 (2012).
22) H. P. Komsa, J. Kotakoski, S. Kurasch, O. Lehtinen, U. Kaiser, and A. V. Krasheninnikov, Phys. Rev. Lett. **109**, 035503 (2012).
23) W. A. McKinley and H. Feshbach, Phys. Rev. **74**, 1759 (1948).
24) Y. C. Lin, D. O. Dumcenco, H. P. Komsa, Y. Niimi, A. V. Krasheninnikov, Y. S. Huang, and K. Suenaga, Adv. Mater. **26**, 2857 (2014).
25) A. R. Beal, J. C. Knights, and W. Y. Liang, J. Phys. C **5**, 3540 (1972).
26) A. R. Beal and W. Y. Liang, J. Phys. C **9**, 2459 (1976).
27) C. H. Ho, C. S. Wu, Y. S. Huang, P. C. Liao, and K. K. Tiong, J. Phys.: Condens. Matter **10**, 9317 (1998).
28) P. C. Yen, H. P. Hsu, Y. T. Liu, Y. S. Huang, and K. K. Tiong, J. Phys.: Condens. Matter **16**, 6995 (2004).
29) S. L. Chuang, in *Physics of Optoelectronic Devices*, ed. J. W. Goodman (Wiley, New York, 1995) p. 102.
30) R. Coehoorn, C. Haas, J. Dijtkstra, C. J. F. Flipse, R. A. de Groot, and A. Wold, Phys. Rev. B **35**, 6195 (1987).
31) R. Coehoorn, C. Haas, and R. A. de Groot, Phys. Rev. B **35**, 6203 (1987).
32) Y. P. Varshni, Physica **34**, 149 (1967).
33) P. Lautenschlager, M. Garriga, S. Logothetidis, and M. Cardona, Phys. Rev. B **35**, 9174 (1987).
34) P. Lautenschlager, M. Garriga, L. Vina, and M. Cardona, Phys. Rev. B **36**, 4821 (1987).
35) C. C. Huang, C. C. Kao, D. Y. Lin, C. M. Lin, F. L. Wu, R. H. Horng, and Y. S. Huang, Jpn. J. Appl. Phys. **52**, 04CH11 (2013).
36) Y. C. Jian, D. Y. Lin, J. S. Wu, and Y. S. Huang, Jpn. J. Appl. Phys. **52**, 04CH06 (2013).
37) T. P. Huang, D. Y. Lin, Y. C. Kao, J. D. Wu, and Y. S. Huang, Jpn. J. Appl. Phys. **50**, 04DH17 (2011).
38) A. M. Chaparro, P. Salvador, B. Coll, and M. Gonzalez, Surf. Sci. **293**, 160 (1993).
39) P. Y. Yu and M. Cardona, *Fundamentals of Semiconductors* (Springer, New York, 2001) 3rd ed., p. 288.
40) G. Weiser, Surf. Sci. **37**, 175 (1973).
41) A. R. Beal and H. P. Hughes, J. Phys. C **12**, 881 (1979).

 

Optik 126 (2015) 666–670

Contents lists available at ScienceDirect

Optik

journal homepage: www.elsevier.de/ijleo

# Growth and optical characterization of $MoS_2$ single crystals with different dopants

Mula Sigiro[a,b,*], Nasruddin MN[c]

[a] Department of Electronic and Computer Engineering, National Taiwan University of Science and Technology, Taipei 106, Taiwan
[b] Department of Physics Education, Faculty of Teacher Training and Education, University of HKBP Nommensen, Medan 20234, Indonesia
[c] Department of Physics, Faculty of Mathematics and Natural Sciences, University of Sumatera Utara, Medan 20155, Indonesia

ARTICLE INFO

*Article history:*
Received 17 December 2013
Accepted 20 July 2014

*Keywords:*
Single crystals
Optical spectroscopy
Molybdenum disulfide
Doping effects

ABSTRACT

Single crystals $MoS_2$:X with different dopants X (X = Re, Nb, Fe, Co, Ni) were grown by the chemical vapor transport method using $Br_2$ as transport agent. By analyzing the X-ray diffraction patterns, the structure of the single crystals shows rhombohedral symmetry for Re and Nb-doped and hexagonal symmetry for Fe, Co, and Ni-doped. Piezoreflectance (PzR) measurements along ***c***-axis at 300 and 25 K were carried out to confirm the origin of the broad peak as observed in electrolyte electroreflectance (EER) measurements and check the optical quality of the samples. The energies and broadening parameters of the A and B excitons of the $MoS_2$:X single crystals have been determined accurately.



## 1. Introduction

Molybdenum disulfide ($MoS_2$), a two dimensional layered-structure materials which belong to the group VIA [1,2], have attracted much interest in recent years for their unique physical properties in thermal, optical and electronic devices. Recent demonstrations of $MoS_2$ devices such as field-effect transistors [3,4], logic circuits [5], phototransistors [6], chemical sensors and photonic detectors [7–9] are already promising. Early studies on the Hall and photoresponse measurements indicate that cobalt can be present only on the surface of $MoS_2$ and has not diffused appreciably into the bulk [12,13]. In catalyst, Co or Ni added to Mo increases the reactivity of catalysts, and because only a small fraction of Co or Ni relative to Mo is needed, they are considered promoters rather than catalysts in their own right [14] while in Fe-doped $MoS_2$, the charge carrier change from holes to electrons [15].

There are two known polytypes of $MoS_2$ [1,2,10]; two-layer hexagonal and three-layer rhombohedral termed 2H and 3R, respectively. Both have regular layered structures with six-fold trigonal prismatic coordination of the Mo atoms by the sulfur atoms within the layers; $2HMoS_2$ has two layers per unit cell stacked in the hexagonal symmetry and belongs to the space group $D^4_{6h}$, while 3R-$MoS_2$ has three layers in the *c*-direction but has rhombohedral symmetry and belongs to the space group $C^5_{3v}$. Previous studies [11] suggest that natural rhombohedral $MoS_2$ is consistently rich in certain minor elements (e.g. Re, Nb, Ti, Zr, Fe), and that incorporation of such impurity elements has predetermined the adoption of the lower structural symmetry of $MoS_2$, i.e. 3R-$MoS_2$. The influence of dopant in transforming 2H-$MoS_2$ to 3R-$MoS_2$ had also been reported recently [16]. However, only few works concerning the effects of dopants in affecting the optical properties of $MoS_2$ have been reported [17].

In this study, we reported optical investigation of $MoS_2$:X single crystals with different dopants X (X = Re, Nb, Fe, Co, Ni) grown by the chemical vapor transport method using $Br_2$ as transport agent. The crystal structure was analyzed by X-ray diffraction (XRD) patterns. Room-temperature electrolyte electroreflectance (EER) measurements were carried out. Piezoreflectance (PzR) were also performed at 300 and 25 K. EER [18] and PzR [19,20] measurements have been used very extensively for semiconductor characterization. The derivative nature of EER and PzR spectrum suppresses uninteresting background effects and greatly enhances the precision in the determination of interband excitonic transition energies. The sharper line shapes as compared to the conventional optical techniques have enabled us to achieve a greater resolution and hence to detect weaker features. The EER and PzR spectra are fitted with a form of the Aspnes equation of the fist derivative Lorentzian lineshape [18,20]. From a detailed lineshape fit we are able to determine accurately the energies and broadening parameters of the excitonic transitions. The parameters which describe the behavior of excitonic transitions indicate that A–B, caused by interlayer interaction and spin-orbit splitting, correspond to excitonic

* Corresponding author. Tel.: +886 2 27376385; fax: +886 2 27376424.
*E-mail address:* mulasigiro@gmail.com (M. Sigiro).

http://dx.doi.org/10.1016/j.ijleo.2014.07.140
0030-4026/

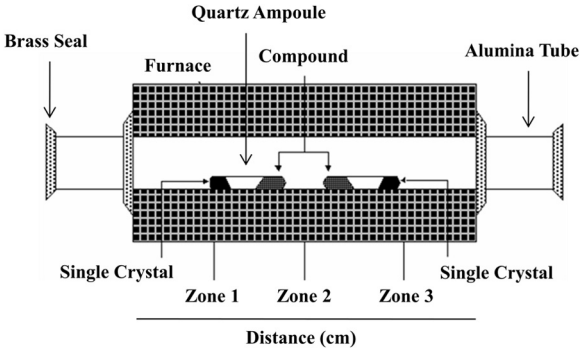


**Fig. 1.** Set up profile for the growth of $MoS_2$:X single crystals.

transitions with different origin. The origin of A, B excitons and the effects of dopant are discussed.

## 2. Crystals growth

The crystal growth of set up profile is shown in Fig. 1. $MoS_2$:X with different dopants X (X = Re, Nb, Fe, Co, Ni) single crystals have been grown by the chemical vapor transport method with $Br_2$ as a transport agent. The total charge used in each growth experiment was about 10 g. The stoichiometrically determined weight of the doping material was added in the hope that it would be transported at a rate similar to that of Mo. The quartz ampoule (40 mm in diameter) containing $Br_2$ ($\sim$5 mg cm$^{-3}$) and uniformly mixed elements (99.99% pure Mo, Re, Nb, Fe, Co, Ni and S) was sealed at $10^{-6}$ Torr. The ampoule was then placed in a Linberg model 54529 three-zone tube furnace and the charge prereacted for 24 h at 800 °C with the growth zone at 950 °C, preventing the transport of the product. The temperature of the furnace was increased slowly to avoid any possibility of explosion due to the exothermic reaction between the elements. The furnace was then equilibrated to give a constant temperature across the reaction tube, and programmed over 24 h to produce the temperature gradient at which single-crystal growth took place. Optimal result was obtained with a temperature gradient of approximately 960 → 930 °C. After 24 h, the furnace was allowed to cool down slowly (40 °C/h) to about 200 °C. The ampoule was then removed and wet tissues applied rapidly to the end away from the crystals to condense the $Br_2$ vapor. When the ampoule reached room temperature, it was opened and the crystals removed. The crystals were then rinsed with acetone and deionized water. Single crystalline platelets up to $10 \times 10$ mm$^2$ surface area and 2 mm in thickness were obtained. The as-grown $MoS_2$:X single crystal is shown in Fig. 2. We do not expect the two solid solutions to be miscible. It was found that a 5% nominal doping of $MoS_2$ prevented the growth of single crystals.

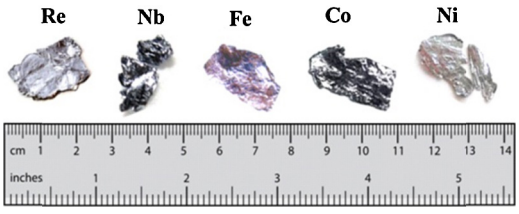


**Fig. 2.** Photograph of the as-grown $MoS_2$:X with different dopants X (X = Re, Nb, Fe, Co, and Ni) single crystal with the surface normal to ***c***-axis.

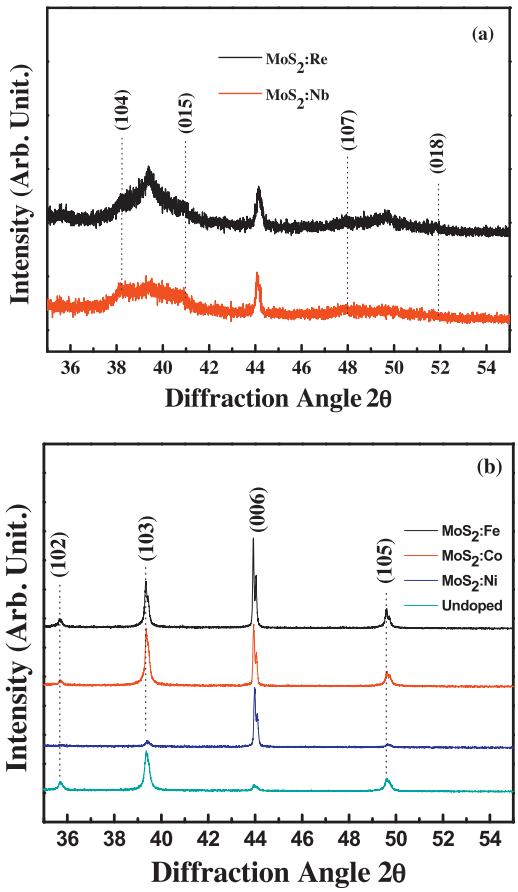


**Fig. 3.** X-ray diffraction patterns of the $MoS_2$:X with different dopants X (X = Re, Neb, Fe, Co, and Ni) single crystal.

## 3. Characterization

### 3.1. X-ray diffraction

XRD patterns of single crystals were obtained by using a Rigaku RTP300RC X-ray with Ni-filtered Cu $K_\alpha$ radiation ($\lambda$ = 1.5418 Å) and a silicon standard was used to calibrate the diffractometer. For the studies, several small crystals from batches of as-grown $MoS_2$:X with different dopants X (X = Re, Nb, Fe, Co, Ni) were finely ground with a mixture of glass powder and the X-ray powder patterns were taken and recorded by means of a slow-moving radiation detector. Lattice parameters were calculated with the aid of computer using a least-squares refinement program.

From the evaluation of the X-ray powder diffraction patterns in Fig. 3, we may conclude that Re and Nb-doped $MoS_2$ samples are of 3R polytype and Fe, Co, and Ni-doped $MoS_2$ samples are 2H-polytype. The X-ray pattern of of Re and Nb-doped $MoS_2$ crystals differed from that of the crystals of Fe, Co, and Ni-doped $MoS_2$ in that the relative intensities of the lines were different and additional lines were present. The change in relative line intensities could not be explained but the additional lines were determined to be due to the presence of the rhombohedral polytype having cell dimension ***a*** = 3.164 Å and ***c*** = 18.371 Å, these numbers are quite similar with JCPDS no. 77-0744 for comparison. The lines were identified with a rhombohedral structure in which, by referring to the hexagonal lattice, the ***a*** parameter of the unit cell was similar to that of the hexagonal polytype (***a*** = 3.160 Å) but the ***c*** parameter was about 1.5 times larger than that of the hexagonal polytype (***c*** = 12.295 Å), these number agreed well with the JCPDS no. 37-1492 for comparison. We notice that the ***a***-parameter

remains unchanged for the Fe, Co, and Ni-doped $MoS_2$, while the ***c***-parameter shows appreciable increase in consistent agreement with the increase in the ***d***-spacing.

### 3.2. EER measurements

EER measurements were carried out at room temperature. The modulated electrical field can easily be applied to the electrolyte-semiconductor interface by a function generator. The sample preparation is achieved by attaching the sample on a copper plate with silver conducting paint. The copper plate and the round edge of the sample must be insulated from the electrolyte by spreading with the Microstop epoxy cement. This insulation conforms that all modulated field was applied to the space charge region of electrolyte-semiconductor interface only. An aqueous solution of 0.5 M $H_2SO_4$ electrolyte was filled into a Teflon tank and a 5 $mm^2$ platinum plate was used for the counter-electrode. The electric field is transversely applied to the exposed semiconductor surface by an ac voltage across the immersed sample and Pt electrodes. The surface states and the nature of impurity determine the surface potential and consequently resulted in a band bending near and at the electrolyte-semiconductor interface. The built-in electric field varied either accumulation or depletion mode depending on the variation of the externally applied voltages. A photomultiplier tube is used for optical detection and the detector response to the DC component of the reflected light is kept constant by an electric servo mechanism so that the ac reflectance is a direct measurement of $\Delta R/R$, the differential reflectivity. Scans of $\Delta R/R$ versus wavelength were obtained using a 0.25 m Photon Technology International (PTI) grating monochromator together with a 150 W tungsten–halogen lamp as a monochromatic light source. Displayed in Fig. 4(a) and (b) are the EER spectra over the range 1.65–2.2 eV at room temperature and characterized by two prominent excitonic transitions, A and B excitons. In order to determine the positions of the transition accurately, the functional form used in the fitting procedure corresponds to a first derivative Lorentzian line shape function on the form [18]

$$\frac{\Delta R}{R} = Re\sum_{j=1}^{n} A_j e^{i\emptyset_j}\left(E - E_j + i\Gamma_j\right)^{-n_i} \quad (1)$$

where the subject $j$ refers to the type of interband transition, $A_j$ and $\emptyset_j$ are the amplitude and phase of the line shape $E_j$ and $\Gamma_j$ are the energy and broadening parameter of the transition and the value of $n_j$ depends on the origin of the transition. The fitted values of $E_j$ and $\Gamma_j$ are displayed in Table 1. The prominent A and B excitons are observed to be red-shifted. The excitonic transition energies were determined precisely and the splitting were estimated to be around 150 meV for Re and Nb-doped $MoS_2$ and 200 meV for Fe, Co, and Ni-doped $MoS_2$. According to Coehoorn et al. [21], this experimentally confirmed that Re and Nb-doped $MoS_2$ structure are 3R-polytypes which has three layers in the ***c***-direction but has rhombohedral symmetry and belong to the space group $C_{3v}^5$, while Fe, Co, and Ni-doped $MoS_2$ structure are 2H-polytypes which has two layers per unit cell stacked in the hexagonal symmetry and belong to the space group $C_{6h}^4$.

### 3.3. PzR measurements

The PzR measurements were achieved by gluing the thin single crystal specimens on a 0.15 cm thick lead–zirconate–titanate (PZT) piezoelectric transducer driven by a 200 $V_{rms}$ sinusoidal wave at 200 Hz. The alternating expansion and contraction of the transducer subjects the sample to an alternating strain with a typical rms $\Delta l/l$ value of $\sim 10^{-5}$. A 150 W tungsten–halogen lamp filtered by a model 270 McPherson 0.35 m monochromator provided the monochromatic light. The reflected light was detected by EG&G type HUV-2000B silicon photodiode. The DC output of the silicon photodiode was maintained constant by a servo mechanism of a variable neutral density filter. A dual-phase lock-in amplifier was used to measure the detected signal. Modulated spectra were normalized to the reflectance to obtain $\Delta R/R$. A RMC model 22 close-cycle cryogenic refrigerator equipped with a model 4075 digital thermometer controller was used to control the measurement temperature between 25 and 300 K with a temperature stability of 0.5 K or better.

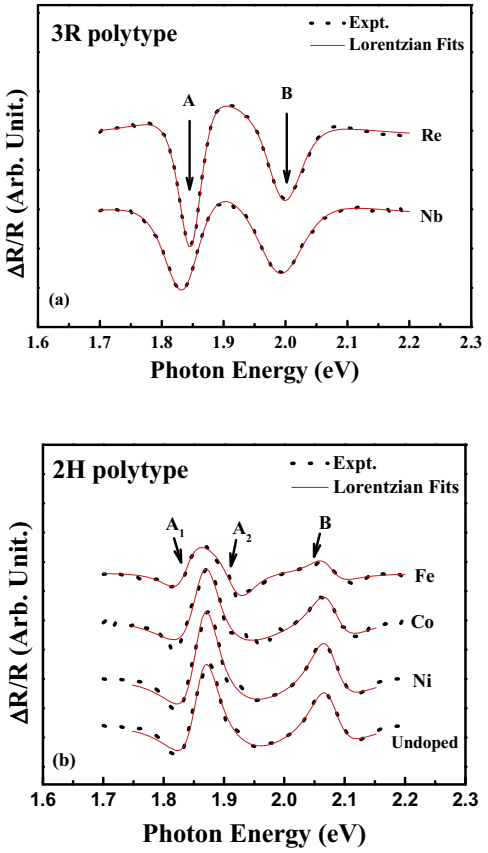


**Fig. 4.** Electrolyte electroreflectance (EER) spectra of $MoS_2$:X with different dopants X (a) X = Re, Nb and (b) X = Fe, Co, Ni at room temperature. The dashed curves are the experimental results and the solid curves are the least-squares fits of Eq. (1).

Displayed in Figs. 5 and 6 are the PzR spectra for the van der Waals plane over the range 1.6–2.2 eV at 300 and 25 K for Re and Nb-doped (top) and Fe, Co, and Ni-doped and undoped (bottom) $MoS_2$ single crystals. The spectra are characterized by two prominent excitonic transitions, A and B excitons [22,23]. If we focus our attention on exciton A feature which lies at the lower energy side, we notice that for the spectra at 300 K, a weak structure denoted as $A_2$ which belongs to the higher series of exciton. A is visible for Fe, Co, and Ni-doped, while not for Re and Nb-doped. In order to ascertain the accurate position of all observable features, we refer to the PzR spectra at 25 K, where the same features are blue shifted and clearly resolved. To determine the positions of the transitions accurately, we have fitted the experimental line shape to the function of the form Eq. (1).

The least-squares fits using Eq. (1) with $n = 2.0$ can be achieved and the fits are shown as solid curves in Figs. 5 and 6. Arrows at Figs. 5(b) and 6(b) show the peak positions of the interband excitonic features, $A_1$, $A_2$ and B, while $A_1$ disappear for Figs. 5(a) and 6(a), respectively. The energies and broadening parameters obtained for these spectra are summarized in Table 1. Comparing the PzR and

**Table 1**
Fitted peak positions and broadening parameters of the excitonic features from EER and PzR measurements.

| Dopants | Temperature (K) | $E^{ex}_{A_1}$ (eV) | $E^{ex}_{A_2}$ (eV) | $E^{ex}_{B}$ (eV) | $\Gamma^{ex}_{A_1}$ (meV) | $\Gamma^{ex}_{A_2}$ (meV) | $\Gamma^{ex}_{B}$ (meV) |
|---|---|---|---|---|---|---|---|
| Re | 300 (EER) | 1.839 ± 0.005 | | 1.993 ± 0.005 | 42 ± 5 | | 65 ± 5 |
| | 25 (PzR) | 1.911 ± 0.005 | | 2.069 ± 0.005 | 20 ± 5 | | 38 ± 5 |
| | 300 | 1.838 ± 0.005 | | 1.994 ± 0.005 | 38 ± 5 | | 55 ± 5 |
| Nb | 300 (EER) | 1.834 ± 0.005 | | 1.982 ± 0.005 | 41 ± 5 | | 73 ± 5 |
| | 25 (PzR) | 1.928 ± 0.005 | | 2.167 ± 0.005 | 13 ± 5 | | 33 ± 5 |
| | 300 | 1.833 ± 0.005 | | 1.981 ± 0.005 | 30 ± 5 | | 62 ± 5 |
| Fe | 300 (EER) | 1.851 ± 0.005 | 1.946 ± 0.005 | 2.051 ± 0.005 | 51 ± 5 | 41 ± 5 | 67 ± 5 |
| | 25 (PzR) | 1.937 ± 0.005 | 1.975 ± 0.005 | 2.152 ± 0.005 | 17 ± 5 | 13 ± 5 | 40 ± 5 |
| | 300 | 1.852 ± 0.005 | 1.948 ± 0.005 | 2.050 ± 0.005 | 40 ± 5 | 33 ± 5 | 56 ± 5 |
| Co | 300 (EER) | 1.852 ± 0.005 | 1.953 ± 0.005 | 2.053 ± 0.005 | 48 ± 5 | 43 ± 5 | 68 ± 5 |
| | 25 (PzR) | 1.941 ± 0.005 | 1.978 ± 0.005 | 2.156 ± 0.005 | 22 ± 5 | 15 ± 5 | 39 ± 5 |
| | 300 | 1.851 ± 0.005 | 1.952 ± 0.005 | 2.051 ± 0.005 | 39 ± 5 | 34 ± 5 | 58 ± 5 |
| Ni | 300 (EER) | 1.852 ± 0.005 | 1.950 ± 0.005 | 2.053 ± 0.005 | 49 ± 5 | 45 ± 5 | 67 ± 5 |
| | 25 (PzR) | 1.938 ± 0.005 | 1.975 ± 0.005 | 2.151 ± 0.005 | 17 ± 5 | 12 ± 5 | 34 ± 5 |
| | 300 | 1.852 ± 0.005 | 1.949 ± 0.005 | 2.052 ± 0.005 | 38 ± 5 | 33 ± 5 | 58 ± 5 |
| Undoped | 300 (EER) | 1.853 ± 0.005 | 1.904 ± 0.005 | 2.071 ± 0.005 | 49 ± 5 | 45 ± 5 | 67 ± 5 |
| | 25 (PzR) | 1.932 ± 0.005 | 1.970 ± 0.005 | 2.148 ± 0.005 | 19 ± 5 | 15 ± 5 | 40 ± 5 |
| | 300 | 1.853 ± 0.005 | 1.903 ± 0.005 | 2.070 ± 0.005 | 34 ± 5 | 48 ± 5 | 68 ± 5 |

EER measurements, we see that the broad peak for Fe, Co and Ni-doped observed previously can be taken to be the average of the room-temperature values for $A_1$ and $A_2$ in the PzR measurements, while for Re and Nb-doped only $A_1$ detected. If we focus our attention on the experimental data of Fe, Co and Ni-doped $MoS_2$, we can conclude that the quality is almost the same as that of the pure crystal (undoped) [22,24]. This experimental observation is consistent with the electrical transport and EER measurements.

XRD, EER and PzR results confirmed that doping is an effective approach and strongly bound for modulating the band structures of $MoS_2$ materials may be understood as follows. The $MoS_2$ single crystals may be stacked in different ways (polytypism) by materials of doping. Thus, $MoS_2$, either natural or synthetic, may be 2H-polytype or 3R or a mixture of both. The unit cell of 2H-$MoS_2$ and 3R-$MoS_2$ contain two and three alternating S–Mo–S layers, respectively. The 2H-polytype is more stable than 3R-polytype.

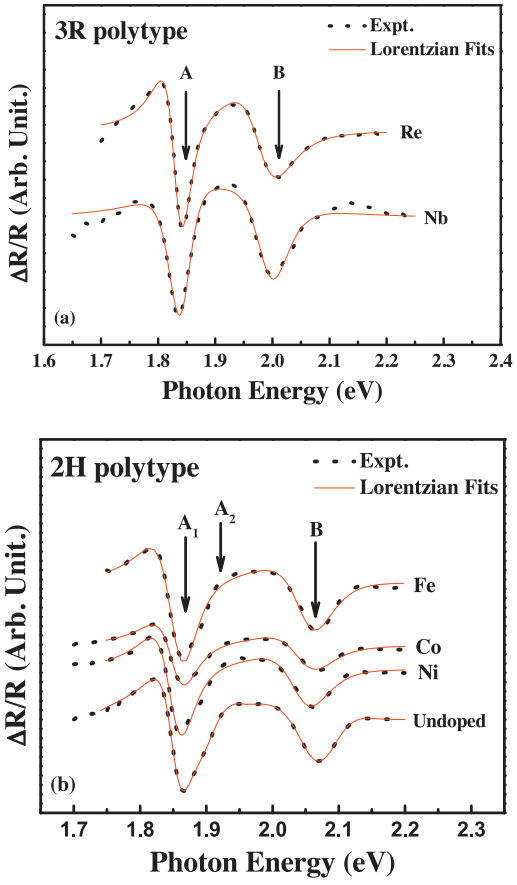


**Fig. 5.** Piezoreflectance (PzR) spectra of $MoS_2$:X with different dopants X (a) X = Re, Nb and (b) X = Fe, Co, Ni at room temperature.

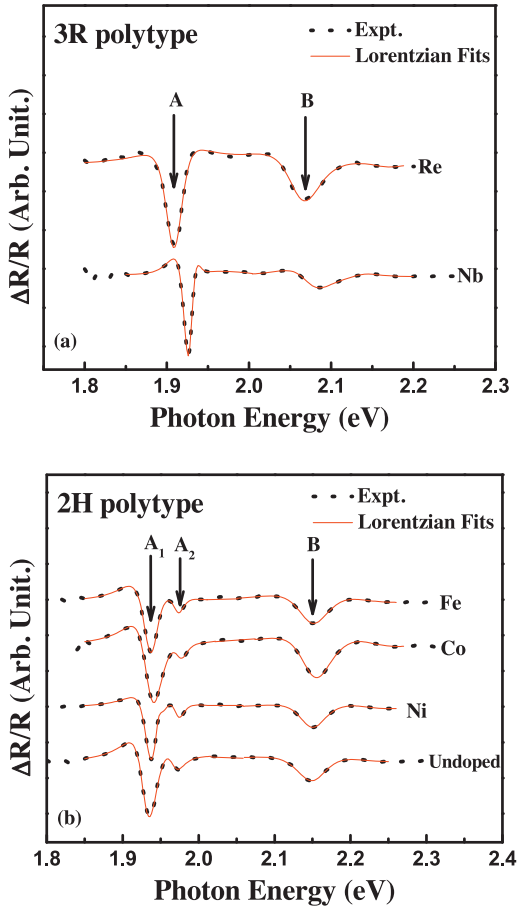


**Fig. 6.** Piezoreflectance (PzR) spectra of $MoS_2$:X with different dopants X (a) X = Re, Nb and (b) X = Fe, Co, Ni at 25 K.

The 3R-polytype transform into the 2H-polytype upon heating. Published experimental data show that (l) both polytypes can be synthesized [25], (2) 3R-polytype converts to 2H, when heated for long periods at temperatures in excess of 500 °C [26], (3) the time necessary for complete conversion in creases drastically as temperature falls [27], (4) 3R-polytype converts to 2H, faster and more completely in the presence of sulfur gas [28], and (5) 3R-polytype converts to 2H, only by recrystallization [28]. Experimental synthesis of $MoS_2$ by reaction of molybdenum metal with sulfur vapor or liquid generally results in a mixture of the 3R and 2H polytypes [29]. In one experiment two $MoS_2$ layers were formed: a 2H layer next to the molybdenum metal and a mixed 3R + 2H layer next to the sulfur [30]. These results are inconsistent with the theory that 3R forms in comparatively sulfur-poor environments. Rather, as Zelikman et al. point out [30], there are differences in the growth mechanisms of $MoS_2$ formed at the metal and sulfur interfaces. The exciton spectra of $MoS_2$ also indicate that the 2H-polytype is energetically stable relative to 3R [1]. This work has supposed that 3R-type in low sulfur fugacity environments and impurity content and is sulfur deficient relative to 2H-polytype because of impurity or dopant. Finally, the addition of an impurity or dopant in synthetic $MoS_2$ affects the 3R-polytype to 2H, conversion reaction.

## 4. Conclusions

In conclusions, we have demonstrated the synthesis of single crystals of $MoS_2$:X with different dopants X (X = Re, Nb, Fe, Co, Ni) were grown by the chemical vapor transport method using $Br_2$ as transport agent. The effect of doping on the optical properties is studied. Our measurements indicate that Re and Nb-doped are stabilize the formation of 3R-$MoS_2$, while Fe, Co and Ni-doped are stabilize the formation of 2H-$MoS_2$. The splitting of excitonic transition energies for A and B were estimated to be around 150 meV for 3R-$MoS_2$ formation and 200 meV for 2H-$MoS_2$ formation.

## Acknowledgement

The authors wish to express thanks to Prof. Ying-Sheng Huang and Prof. Ching-Hwa Ho for numerous helpful comments, assisting and discussion.

## References

[1] J.A. Wilson, A.D. Yoffe, The transition metal dichalcogenides discussion and interpretation of the observed optical, electrical and structural properties, Adv. Phys. 18 (1969) 193–335.
[2] A.R. Beal, J.C. Knights, W.Y. Liang, Transmission spectra of some transition metal dichalcogenides. II. Group VIA: trigonal prismatic coordination, J. Phys. C: Solid State Phys. 5 (1972) 3540–3551.
[3] A. Ayari, E. Cobas, O. Ogundadegbe, M.S. Fuhrer, Realization and electrical characterization of ultrathin crystals of layered transition-metal dichalcogenides, J. Appl. Phys. 101 (2007) 014507.
[4] B. Radisavljevic, A. Radenovic, J. Brivio, V. Giacometti, A. Kis, Single-layer $MoS_2$ transistors, Nat. Nanotechnol. 6 (2011) 147–150.
[5] B. Radisavljevic, M.B. Whitwick, A. Kis, Integrated circuits and logic operations based on single-layer $MoS_2$, ACS Nano 5 (2011) 9934–9938.
[6] Z. Yin, H. Li, H. Li, L. Jiang, Y. Shi, Y. Sun, G. Lu, Q. Zhang, X. Chen, H. Zhang, Single-layer $MoS_2$ phototransistors, ACS Nano 6 (2012) 74–80.
[7] F.K. Perkins, A.L. Friedman, E. Cobas, P.M. Campbell, G.G. Jernigan, B.T. Jonker, Chemical vapor sensing with monolayer $MoS_2$, Nano Lett. 13 (2013) 668–673.
[8] H. Li, Z.Y. Yin, Q.Y. He, H. Li, X. Huang, G. Lu, D.W.H. Fam, A.I.Y. Tok, Q. Zhang, H. Zhang, Fabrication of single and multilayer $MoS_2$ film-based field-effect transistors for sensing NO at room temperature, Small 8 (2012) 63–67.
[9] D.S. Tsai, K.K. Liu, D.H. Lien, M.L. Tsai, C.F. Kang, C.A. Lin, L.J. Li, J.H. He, Few-layer $MoS_2$ with high broadband photogain and fast optical switching for use in harsh environments, ACS Nano 7 (2013) 3905–3911.
[10] R. Murray, B.L. Evans, Applications of a solid-state detector on a modern single-crystal X-ray diffractometer, J. Appl. Crystallogr. 12 (1979) 263–266.
[11] R.J. Traill, A rhombohedral polytype of molybdenite, Can. Mineral. 7 (1963) 524–526.
[12] D.M. D'Ambra, J.V. Marzik, R. Kershaw, J. Baglio, K. Dwighta, A. Wold, Preparation and electronic properties of $MoS_2$ and $WS_2$ single crystals grown in the presence of cobalt, J. Solid State Chem. 57 (1985) 351–356.
[13] D.M. D'Ambra, R. Kershaw, J. Baglio, K. Dwight, A. Wold, The photoelectrochemical properties of $MoS_2$ single crystals grown in the presence of cobalt, J. Solid State Chem. 64 (1986) 108–112.
[14] J.V. Lauritsen, J. Kibsgaard, G.H. Olesen, P.G. Moses, B. Hinnemann, S. Helveg, J.K. Nørskov, B.S. Clausen, H. Topsøe, E. Lægsgaard, F. Besenbacher, Location and coordination of promoter atoms in Co- and Ni-promoted $MoS_2$-based hydrotreating catalysts, J. Catal. 249 (2007) 220–233.
[15] C. Tiwari, R. Sharma, Y. Sharma, Ab-initio study of Fe doped molybedenum dichalcogenides, AIP Conf. Proc. 1512 (2013) 852–853.
[16] K.K. Tiong, P.C. Liao, C.H. Ho, Y.S. Huang, Growth and characterization of rhenium-doped $MoS_2$ single crystals, J. Cryst. Growth 205 (1999) 543–547.
[17] W.Y. Liang, Optical anisotropy in layer compounds, J. Phys. C: Solid State Phys. 6 (1973) 551–565.
[18] D.E. Aspnes, Optical Properties of Semiconductors, in: M. Balkanski (Ed.), Handbook on Semiconductors 2, North-Holland, Amsterdam, 1980, p. 109.
[19] H. Mathieu, J. Allegre, B. Gil, Piezomodulation spectroscopy: a powerful investigation tool of heterostructures, Phys. Rev. B: Condens. Matter 43 (1991) 2218–2227.
[20] F.H. Pollak, H. Shen, Modulation spectroscopy of semiconductors: bulk/thin film, microstructures, surfaces/interfaces and devices, Mater. Sci. Eng. R 10 (7–8) (1993) 275–374.
[21] R. Coehoorn, C. Haas, R.A. de Groot, Electronic structure of $MoSe_2$, $MoS_2$, and $WSe_2$, II. The nature of the optical band gaps, Phys. Rev. B: Condens. Matter 35 (12) (1987) 6203–6206.
[22] C. Ballif, M. Regula, F. Levy, Optical properties of tungsten disulfide single crystals doped with gold, Sol. Energy Mater. Sol. Cells 57 (1999) 189–207.
[23] G.L. Frey, R. Tenne, M.J. Matthews, M.S. Dresselhaus, G. Dresselhaus, Optical properties of $MS_2$ (M=Mo,W) inorganic fullerene-like and nanotube material, J. Mater. Res. 13 (1998) 9–14.
[24] M. Remskar, Z. Skraba, P. Stadelmann, F. Levy, Structural stabilization of new compounds: $MoS_2$ and $WS_2$ micro- and nanotubes alloyed with gold and silver, Adv. Mater. 12 (2000) 814–818.
[25] R.E. Bell, R.E. Herfert, Preparation and characterization of a new crystalline form of molybdenum disulfide, J. Am. Chem. Soc. 79 (1957) 3351–3354.
[26] J.C. Wildervanck, F. Jellinek, Preparation and crystallinity of molybdenum and tungsten sulfides, Z. Anorg. Allg. Chem. 328 (1964) 309–318.
[27] A.H. Clark, Compositional differences between hexagonal and rhombohedral molybdenite, Neues Jahrb. Mineral. Monatsh. (1970) 33–38.
[28] A.N. Zelikman, G.V. Indenbaum, M.V. Testlistkaya, V.P. Salankova, Structural transformation in synthetic $MoS_2$, Transl. Sov. Phys-Crystallogr. 14 (1969) 687–691.
[29] E.A. Dukhovskoi, Y.V. Makarov, N.I. Sarpov, A.A. Sitin, Crystal structure of $MoS_2$ coatings on molybdenum, Transl. Inorg. Mater. 12 (1976) 1118–1120.
[30] A.N. Zelikman, B.P. Lobashev, Y.V. Macarov, G.I. Sevost'yanova, Kinetics and mechanism of the growth of molybdenum disulfide coatings on molybdenum, Transl. Inorg. Mater. 12 (1976) 1367–1370.

# Study of Re, Au, and Fe dopant effect on the structure and optical properties of molybdenum disulfide single crystals



2
Author(s)

Sigiro Mula ; Ho Ching-Hwa

View All Authors



**Abstract:**
We report on extensive structural and optical studies of a variety of pure and Re-, Au-, Fe-doped molybdenum disulfide ($MoS_2$) single crystals which grown by chemical vapor transport (CVT) method. In order to compare structural properties of crystals with different doping we conducted X-ray diffraction (XRD) and transmission electron microscopy (TEM) measurements. For optical characterization we used Raman spectroscopy, piezoreflectance (PzR), electrolyte electroreflectance (EER) and photoconductivity (PC).

**Published in:** Compound Semiconductor Week (CSW) [Includes 28th International Conference on Indium Phosphide & Related Materials (IPRM) & 43rd International Symposium on Compound Semiconductors (ISCS), 2016

**Date of Conference:** 26-30 June 2016

**INSPEC Accession Number:** 16196210

**Date Added to IEEE *Xplore*:** 04 August 2016

**DOI:** 10.1109/ICIPRM.2016.7528820

**ISBN Information:**

**Publisher:** IEEE

## Contents



We report on extensive structural and optical studies of a variety of pure and Re-, Au-, Fe-doped molybdenum disulfide ($MoS_2$) single crystals which grown by chemical vapor transport (CVT) method. In order to compare structural properties of crystals with different doping we conducted X-ray diffraction (XRD) and transmission electron microscopy (TEM) measurements. For optical characterization we used Raman spectroscopy, piezoreflectance (PzR), electrolyte electroreflectance (EER) and photoconductivity (PC).

**Read document**

**Keywords**

**IEEE Keywords**

**IEEE Keywords**
Optical diffraction, Crystals, Electron optics, Compounds, Gold, Iron, Periodic structures

Citations

Keywords

Back to Top

**INSPEC: Controlled Indexing**
X-ray diffraction, crystal growth from vapour, crystal structure, electroreflectance, gold, iron, molybdenum compounds, photoconductivity, piezoreflectance, Raman spectra, rhenium, semiconductor doping, semiconductor growth, semiconductor materials, transmission electron microscopy

**INSPEC: Non-Controlled Indexing**
$MoS_2$:Fe, dopant effect, optical properties, molybdenum disulfide single crystals, chemical vapor transport, CVT, structural properties, X-ray diffraction, XRD, transmission electron microscopy, TEM, Raman spectroscopy, piezoreflectance, electrolyte electroreflectance, photoconductivity, $MoS_2$:Re, $MoS_2$:Au

## Authors

Sigiro Mula
Department of Physics Education, Faculty of Teacher Training and Education, University of HKBP Nommensen, Indonesia

Ho Ching-Hwa
Graduate Institute of Applied Science and Technology, National Taiwan University of Science and Technology, Taiwan

## Related Articles

Optical properties of InGaN double heterostructures and quantum wells grown by metalorganic chemical vapor deposition
R.D. Dupuis; P.A. Grudowski; C.J. Eiting; J. Park; B.S. Shelton; D.J.H. Lambert; I. Shmagin; R.M. Kolbas

Regrowth of semi-insulating iron doped InP around reactive ion etched laser mesas in [110] and [-110] directions by hydride vapour phase epitaxy
O. Kjebon; S. Lourdudoss; J. Wallin

Properties of iron-doped multicrystalline silicon grown by the float-zone technique
T.F. Ciszek; T.H. Wang; R.K. Ahrenkiel; R. Matson

Properties of iron disilicide doped with Ru, Rh and Pd
M.I. Fedorov; M.A. Khazan; A.E. Kaliazin; V.K. Zaitsev; N.F. Kartenko; A.E. Engelychev

Fe distribution around hydride VPE InP:Fe regrown laser stripes
R. Gobel; H. Janning; H. Burkhard

High quality InP substrates grown by the VCZ method
Y. Yabuhara; K. Oida; Y. Hosokawa; R. Nakai; K. Aoyagi; Y. Iguchi; T. Iwasaki

Influence of Fe dopant on the optical and nonlinear optical properties of ZnO thin films obtained by spray ultrasonic
S. Abed; M.S. Aida; N. Bouhssira; K. Bouchouit

$Cu^{2+}$ and $Zn^{2+}$ Adsorption to Synthetic Iron Oxides and Natural Iron Ore Powder
Yu Li; Jianlin Liu; Xiaoli Wang; Ting Wang; Xianyuan Du

4-inch InP crystals grown by phosphorous vapor controlled LEC method
A. Noda; K. Suzuki; A. Arakawa; H. Kurita; R. Hirano

Growth of dislocation free grade Fe doped InP crystals
A. Noda; M. Nakamura; A. Arakawa; R. Hirano

# Study of Re, Au, and Fe Dopant Effect on the Structure and Optical Properties of Molybdenum Disulfide Single Crystals

Mula Sigiro[1,2*], and Ching-Hwa Ho[3]
[1]Department of Physics Education, Faculty of Teacher Training and Education, University of HKBP Nommensen, Medan 20234, Indonesia.
[2]Department of Electronic and Computer Engineering, National Taiwan University of Science and Technology, Taipei 106, Taiwan.
[3]Graduate Institute of Applied Science and Technology, National Taiwan University of Science and Technology, Taipei 106, Taiwan.
*Corressponding author: mulasigiro@gmail.com

***Abstract*— We report on extensive structural and optical studies of a variety of pure and Re-, Au-, Fe-doped molybdenum disulfide ($MoS_2$) single crystals which grown by chemical vapor transport (CVT) method. In order to compare structural properties of crystals with different doping we conducted X-ray diffraction (XRD) and transmission electron microscopy (TEM) measurements. For optical characterization we used Raman spectroscopy, piezoreflectance (PzR), electrolyte electroreflectance (EER) and photoconductivity (PC).**

***Keywords—transition-metal dichalcogenides, piezoreflectance, photoconductivity, excitons***

## I. INTRODUCTION

Dopant in solid generally governs the physical and chemical properties of any kind of materials and is of great technological importance. In the case of bulk system, a prominent example is seen in semiconductor industry where doping is used to adjust carrier densities and to tailor the electronic characteristics of the devices [1]. Moreover, the effect of doping is very significant in two dimensional systems. Recently, transition-metal dichalcogenide compounds (TMDs), particularly molybdenum disulfide ($MoS_2$), have been extensively investigated because of the possible practical application as catalysts, lubricants, lithium batteries, and phototransistors as well as in nanoelectronics and excellent candidates for the study of fundamental physics in two-dimensional materials [2]. The knowledge of how dopant atoms influence and interact with the host TMD lattices are highly important both in fundamental science and future device technology. This paper deals with the influence of dopant elements (Re, Au, Fe) mainly on the structural and optical properties of $MoS_2$ single crystals grown by chemical vapor transport method using $Br_2$ as a transport agent. These results provide useful guidance for the fabrication of semiconductor and electronic devices using $MoS_2$ structures.

## II. EXPERIMENTAL METHODS, RESULTS AND DISCUSSIONS

### *Experimental methods*

The $MoS_2$ single crystals were grown by the chemical vapor transport (CVT) method, using $Br_2$ and $I_2$ as a transporting agent. The elements including Mo(99.99%), S(99.99%) and dopants(99.99%) were used for the crystal growth and the next steps of methods are similar to that of $ReS_2$ we grown before [3]. In order to characterize our samples we used different experimental methods like X-ray diffraction (XRD), transmission electron microscopy (TEM), piezoreflectance (PzR), electrolyte electroreflectance (EER), and photoconductivity (PC). They are described in detail in our previous work [3-6].

### *Results and discussions*

Fig. 1 reveals the XRD pattern of doped and undoped $MoS_2$ single crystals. The relative intensity and resolution of observed peaks change for different doping. For Re and Au doped crystals observed peaks correspond to 3R phase (cell dimension $\boldsymbol{a}$ = 3.164 Å and $\boldsymbol{c}$ = 18.371 Å) , whereas for Fe-doped and pure crystals the patterns correspond to 2H phase. In 2H lattice, ***a-*** parameter of the unit cell is similar to that of the 3R ($\boldsymbol{a}$ = 3.160 Å), while $\boldsymbol{c}$ parameter is about 1.5 times larger ($\boldsymbol{c}$ = 12.295 Å). We noticed that $\boldsymbol{a}$-parameter remains unchanged for the Fe-doped and undoped samples, whereas the $\boldsymbol{c}$-parameter shows appreciable increase in consistent agreement with the increase in the $\boldsymbol{d}$-spacing.

In Fig. 2 the TEM images for differently doped $MoS_2$ crystals are presented. It is clearly seen that Re atoms tend to occupy or substitute Mo atoms in host $MoS_2$ lattice. However, Au atoms move around on the $MoS_2$ surface and they can jump to different position. On other hand, Fe atoms are segregated into groups and dispersed not uniformly on the surface. Fig. 3 shows the peaks of two (unpolarized) and three (polarized) dominant first order Raman-active modes on the edge plane. Also, we measured for basal plane which confirmed that only two modes even used polarizer. From Raman spectra analysis we could not able to distinguish 2H and 3R. The PzR spectra have recorded in the range 25 to 300 K to determine the energies, broadening parameters, and temperature dependence of the line-width of the A dan B excitons accurately via a detailed line shape fit, Varshni and Bose-Einstein equations of the which these formulations are similar to that

of $Mo_{1-x}W_xS_2$ we did before [6]. The fitted values of PzR and EER for exciton and broadening parameter given in Table 1 and the splitting of A and B excitons of 3R calculated around 150 meV, while around 200 meV for 2H. EER measurements confirmed that the amplitudes of excitons A and B are proportional to modulation voltage. Fig. 4 revealed that these materials are an indirect semiconductor.

**Acknowledgements**

The authors would like to acknowledge the financial supports by the National Science Council of Taiwan under Grant Nos. NSC 101-2811-M-011-002 and NSC 100-2112-M-011-001-MY3. Acknowledge for TEM images supported by Prof. Kazu Suenaga and AIST-Japan.

**References**

[1] P. M. Voyles, D. A. Muller, J. L. Grazul, P. H. Citrin and H. J. L. Gossmann, Nature **416** (2002) 826.

[2] Z. Huang, X. Peng, H. Yang, C. He, L. Xue, G. Hao, C. Zhang, W. Liu, X. Qia and J. Zhong, RSC Adv. **3** (2013) 12939.

[3] C. C. Huang, C. C. Kao, D. Y. Lin, C. M. Lin, F. L. Wu, R. H. Horng and Y. S. Huang, Jpn. J. Appl. Phys. **52** (2013) 04CH11.

[4] D. O. Dumcenco, H. Kobayashi, Z. Liu, Y.S. Huang and K. Sueenaga, Nat. Commun. **4** (2013) 1351.

[5] D. O. Dumcenco, Y. C. Su, Y. P. Wang, K..Y. Chen, Y. S. Huang, C. H. Ho and K. K. Tiong, Chin. J. Phys. **49** (2011) 270.

[6] C. H. Ho, C. S. Wu, Y. S. Huang, P. C. Liao, and K.K. Tiong, J. Phys. Condens. Matter **10 (41)** (1998) 9317.

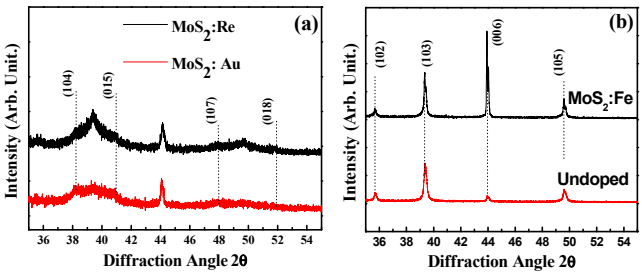


Fig.1 XRD spectra of the $MoS_2$ with different dopants

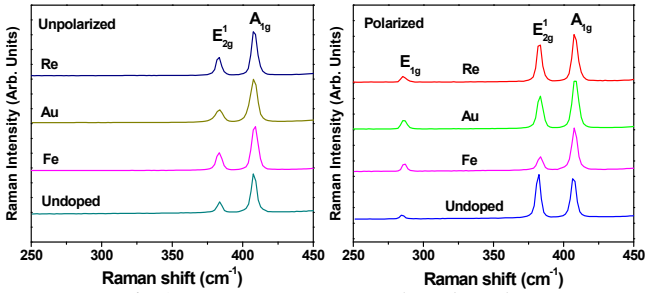


Fig.3 . Raman spectra on the edge plane

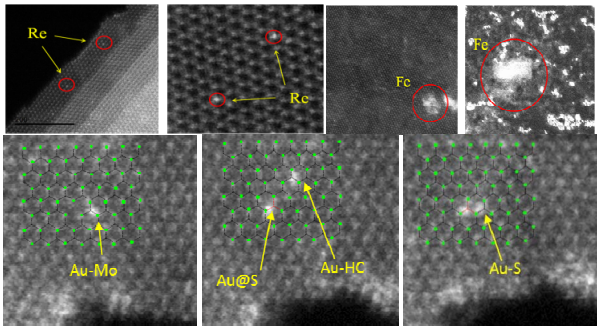


Fig.2 TEM image of the $MoS_2$ with different dopants

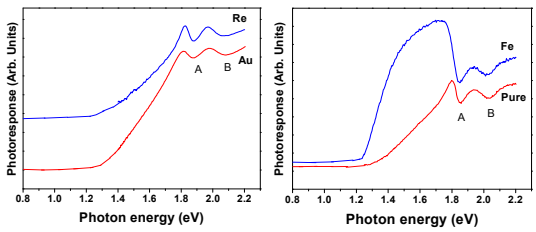


Fig.4 PC spectra of the $MoS_2$ with different dopants

Table I Fitted peak positions and broadening parameters of the excitonic features from EER and PzR measurements

| Dopants | Temperature (K) | $E^{ex}_{A_1}(eV)$ | $E^{ex}_{A_2}(eV)$ | $E^{ex}_{B}(eV)$ | $\Gamma^{ex}_{A_1}(eV)$ | $\Gamma^{ex}_{A_2}(meV)$ | $\Gamma^{ex}_{B}(meV)$ |
|---|---|---|---|---|---|---|---|
| Re | 300 (EER) | 1.839 ± 0.005 | | 1.993 ± 0.005 | 42±5 | | 65±5 |
| | 25 (PzR) | 1.911 ± 0.005 | | 2.069 ± 0.005 | 20±5 | | 38±5 |
| | 300 | 1.838 ± 0.005 | | 1.994 ± 0.005 | 38±5 | | 55±5 |
| Au | 300 (EER) | 1.833 ± 0.005 | | 1.981 ± 0.005 | 30±5 | | 62±5 |
| | 25 (PzR) | 1.931 ± 0.005 | | 2.091 ± 0.005 | 22±5 | | 41±5 |
| | 300 | 1.854 ± 0.005 | | 2.014 ± 0.005 | 18±5 | | 58±5 |
| Fe | 300 (EER) | 1.851 ± 0.005 | 1.946 ± 0.005 | 2.051 ± 0.005 | 51±5 | 41±5 | 67±5 |
| | 25 (PzR) | 1.937 ± 0.005 | 1.975 ± 0.005 | 2.152 ± 0.005 | 17±5 | 13±5 | 40±5 |
| | 300 | 1.852 ± 0.005 | 1.948 ± 0.005 | 2.050 ± 0.005 | 40±5 | 33±5 | 56±5 |
| Undoped | 300 (EER) | 1.853 ± 0.005 | 1.904 ± 0.005 | 2.071 ± 0.005 | 49±5 | 45±5 | 67±5 |
| | 25 (PzR) | 1.932 ± 0.005 | 1.970 ± 0.005 | 2.148 ± 0.005 | 19±5 | 15±5 | 40±5 |
| | 300 | 1.853 ± 0.005 | 1.903 ± 0.005 | 2.070 ± 0.005 | 34±5 | 48±5 | 68±5 |

Optik 127 (2016) 1599–1602

Contents lists available at ScienceDirect

Optik

journal homepage: www.elsevier.de/ijleo

# Growth and optical studies of tungsten disulphide single crystals doped with gold

M.N. Nasruddin[a], Mula Sigiro[b,*]

[a] Department of Physics, Faculty of Mathematics and Natural Sciences, University of Sumatera Utara, Medan 20155, Indonesia
[b] Department of Physics Education, Faculty of Teacher Training and Education, University of HKBP Nommensen, Medan 20234, Indonesia

ARTICLE INFO

*Article history:*
Received 20 April 2015
Accepted 10 November 2015

*Keywords:*
Layered crystals
Surface photovoltage spectroscopy
Piezoreflectance

ABSTRACT

Tungsten disulphide single crystals doped with gold ($WS_2$:Au) have been grown by the chemical vapor transport method using iodine as a transporting agent. The structure of the materials was characterized by scanning electron microscope (SEM), X-ray diffraction (XRD), and Raman measurements. The doping effects of the materials are characterized by surface photovoltage (SPV) and piezoreflectance (PzR) measurements. The SPV spectrum reveals an impurity level located below the A exciton. The direct band-edge excitonic transition energies for $WS_2$:Au show redshifts and the broadening parameters of the excitonic transition features increase due to impurity scattering.



## 1. Introduction

Tungsten disulphide ($WS_2$) belongs to group VIA transition metal dichalcogenides $MX_2$ that exhibit many interesting physical properties with a pronounced two dimensional character [1]. The peculiar properties of these materials result from their layered structure, consisting of almost covalently bonded X-M-X sheets linked by weak van der Waals forces. $WS_2$, an indirect-gap semiconductor, has the subject of great interest, because its band gap is well matched to the solar spectrum. Taking into account prevention of photocorrosion, $WS_2$ can act as an efficient photoconductive layer in photovoltaic devices and photoelectrochemical solar cells [2]. Up-to date, only a few works concerning the doping effect on the properties of $WS_2$ was reported [3,4].

In this work, we report a detailed characterization, including scanning electron microscope (SEM), X-ray diffraction (XRD), Raman, surface photovoltage (SPV) and piezoreflectance (PzR) measurements of Au-doped $WS_2$ single crystals. The effects of dopant (Au) on the optical properties of $WS_2$ were analyzed and discussed.

## 2. Experiment

Single crystals of the system Au-doped $WS_2$ were grown using the chemical vapor transport (CVT) method with $Br_2$ as a transport agent. The total charge used in each growth experiment was about 10 g. The stoichiometrically determined weight of doping material was added in the hope that it will be transported at a rate similar to that of Mo. Before the crystal growth, the powdered compounds were prepared from the elements by reaction at 1000 °C for 10 days in an evacuated quartz ampoule. Prior to the crystal growth, a quartz ampoule (22 mm OD, 17 mm ID, 20 cm length) containing $Br_2$ (~5 mg/cm$^3$) and the elements (W, 99.99% pure; Au, 99.99%; S, 99.999%) was evacuated to $10^{-6}$ Torr and sealed. It was shaken well for uniform mixing of the powder. The ampoule was placed in a three-zone furnace and the charge prereacted for 24 h at 800 °C with the growth zone at 950 °C, preventing the transport of the product. The temperature of the furnace was increased slowly. The slow heating was necessary to avoid any possibility of explosion due to the exothermic reaction between the elements. The furnace was then equilibrated to give a constant temperature across the reaction tube, and was programmed over 24 h to produce the temperature gradient at which single crystal growth took place. Optimal results were obtained with temperature gradient of approximately 960 °C → 930 °C. After 240 h, the furnace was allowed to cool down slowly (40 °C/h) to about 200 °C. The ampoule was then removed and wet tissues applied rapidly to the end away from the crystals to condense the $Br_2$ vapor. When the ampoule reached room temperature, it was opened and the crystals removed. The crystals were then rinsed with acetone and deionized water. Single crystalline platelets up to 10 mm × 10 mm surface area and 2 mm in thickness were obtained.

The morphology of the $WS_2$:Au was recorded using a JEOL-JSM6500F field-emission scanning electron microscope (FESEM).

* Corresponding author at: Center of Semiconductor Physics Studies (CSPS), University of HKBP Nommensen, Medan, Indonesia. Tel.: +62 61 4522831; fax: +62 61 4571426.
*E-mail address:* mulasigiro@gmail.com (M. Sigiro).

http://dx.doi.org/10.1016/j.ijleo.2015.11.056
0030-4026/

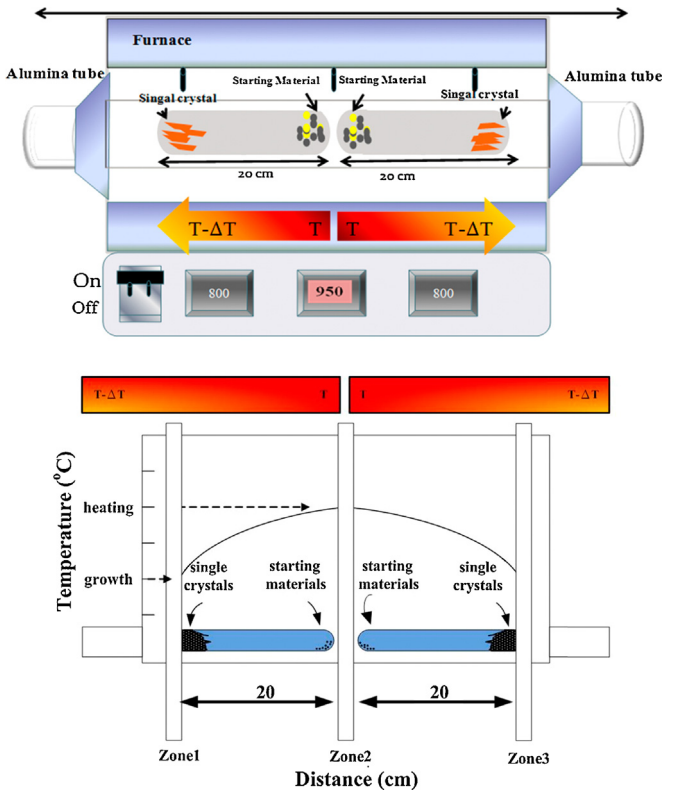


**Fig. 1.** The schematic diagram of the CVT setup and temperature profile for the growth of Au-doped $WS_2$ single crystals.

For X-ray studies, several small crystals from each grown batch of $WS_2$:Au were finely ground into powders. The powder X-ray patterns were taken and recorded by means of a slow moving radiation detector. The copper $K_\alpha$ radiation ($\lambda = 1.542$ Å) was employed in the X-ray diffraction measurements and a silicon standard used for experimental calibration.

The SPV measurements, which used normalized incident light intensity, were performed at normal incidence using a fixed grid and probe light chopped at 200 Hz [5]. The method of PzR has been described in the literature [6]. The measurements were achieved by gluing the thin single-crystal specimens on a 0.15 cm thick lead zirconate titanate piezoelectric transducer driven by a 200 $V_{rms}$ sinusoidal wave at 200 Hz. An RMC model 22 closed-circle cryogenic refrigerator equipped with a model 4075 digital thermometer controller was used for low-temperature measurements. The measurements were made between 15 and 300 K with a temperature stability of 0.5 K or better (Fig. 1).

## 3. Results and discussion

The photo of the pristine $WS_2$:Au single crystals with centimeter sizes grown by CVT is shown in Fig. 2(a). The FESEM image of the $WS_2$:Au single crystals after preliminary mechanical exfoliation is depicted in Fig. 2(b) and most of the flakes have a random shape. The structure of $WS_2$:Au single crystals was further examined by the XRD measurement. Fig. 3 illustrates the XRD patterns. Four major diffraction peaks centered at 29.0°, 44.0°, 59.9°, and 77.2° were detected, which belong to a single orientation group of ⟨0 0 1⟩ (*c*-axial) (JCPDS #381367) for the mixed of rhombohedral and hexagonal structure of $WS_2$. Fig. 4 depicts the Raman scattering measurements for the $WS_2$:Au single crystals, the intensity of Raman lines in unpolarized and polarized ($Z(XX)\bar{Z}$ and $Z(XY)\bar{Z}$) configurations differ appreciably showing the first order Raman active modes. Two major Raman modes, respectively, at around 353 and

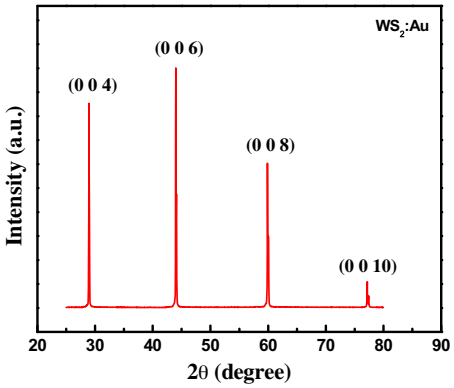


**Fig. 3.** The XRD pattern of $WS_2$:Au single crystals.

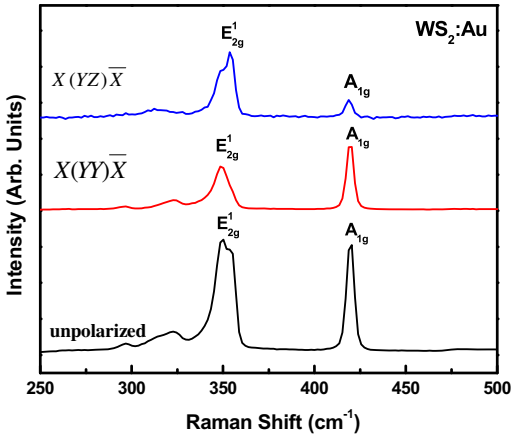


**Fig. 4.** The Raman spectra of $WS_2$:Au single crystals.

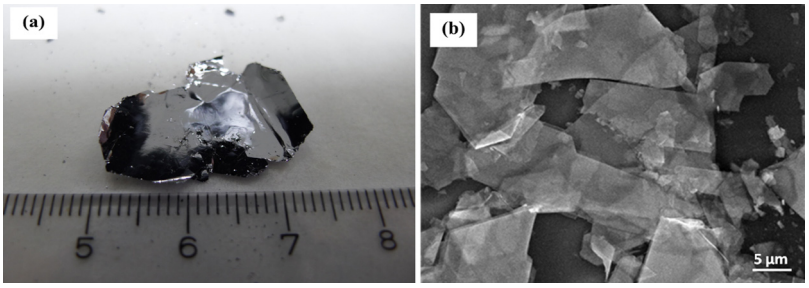


**Fig. 2.** (a) Photograph and (b) SEM image of $WS_2$:Au single crystals grown by CVT.

**Table 1**
Transition energies of the excitons A, B, d and C at 15 and 300 K. The corresponding values in previous works are included.

| Sample | Temperature (K) | $E_A$ (eV) | $E_B$ (eV) | $E_d$ (eV) | $E_C$ (eV) |
|---|---|---|---|---|---|
| 2H-$WS_2$:Au[a] | 15 | 2.048 ± 0.002 | 2.460 ± 0.003 | 2.715 ± 0.005 | 2.799 ± 0.005 |
| | 300 | 1.959 ± 0.005 | 2.347 ± 0.008 | 2.664 ± 0.010 | 2.743 ± 0.010 |
| 2H-$WS_2$[a] | 15 | 2.068 ± 0.002 | 2.494 ± 0.003 | 2.729 ± 0.005 | 2.821 ± 0.005 |
| | 300 | 1.986 ± 0.005 | 2.384 ± 0.008 | 2.680 ± 0.010 | 2.770 ± 0.010 |
| 2H-$MoS_2$[b] | 300 | 1.853 ± 0.008 | 2.070 ± 0.008 | | |
| 3R-$MoS_2$:Au[c] | 300 | 1.854 ± 0.005 | 2.082 ± 0.005 | | |
| 3R-$MoS_2$:Nb[d] | 300 | 1.834 ± 0.005 | 1.982 ± 0.005 | | |

[a] Present work.
[b] Previous work [15].
[c] Previous work [16].
[d] Previous work [17].

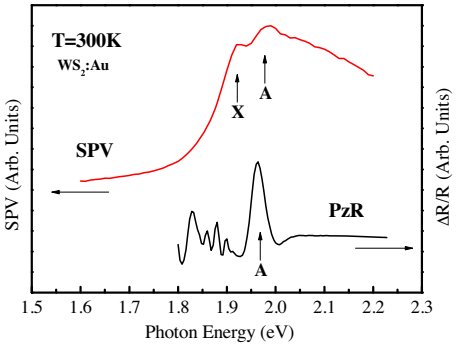


**Fig. 5.** Room-temperature SPV and PzR spectra of $WS_2$:Au single crystals.

418 were detected, which are consistent with the $E^1_{2g}$ and $E_{1g}$ modes in the previous reports for the $WS_2$ single crystal [7–12]. By normalizing the intensity of $E^1_{2g}$ and $E_{1g}$ modes, no significant difference can be observed from the peak broadening and position of $E^1_{2g}$ and $E_{1g}$ modes for the unpolarized and polarized ($Z(XX)\bar{Z}$ and $Z(XY)\bar{Z}$) configurations.

Fig. 5 shows a room-temperature SPV and PzR spectra of $WS_2$:Au. The excitonic feature A has been detected in both SPV and PzR spectra. An additional feature located ~50 meV below exciton A, denoted as X, is observed in the SPV spectrum. The possible origin of this feature can be explained as follows. It is known that the surface photovoltage signal is proportional to the absorption coefficient $\alpha$. The appearance of an additional feature in SPV spectrum is related to an impurity absorption peak due to the doped of Au, since such feature only observed in the doped sample.

Displayed in Fig. 6 are the PzR spectra over the range 1.8–3.0 eV at 15 K and room temperature for the Au-doped and undoped $WS_2$ single crystals. The spectra are characterized by four excitonic transitions marked by A, B, d and C according to previous results [13]. In case of undoped $WS_2$, the higher series of the A exciton and an adjacent resonance feature above the A series denoted as $A_2$ and $A_R$, are also detected. In order to determine the positions of the transitions accurately, we used a first-derivative Lorentzian line shape function of the form [14]

$$\frac{\Delta R}{R} = Re\left[\sum_{i=1}^{n} A_i^{ex} e^{j\varphi_i^{ex}} (E - E_i^{ex} + j\Gamma_i^{ex})^{-2}\right], \quad (1)$$

where $A_i^{ex}$ and $\varphi_i^{ex}$ are the amplitude and phase of the line shape, $E_i^{ex}$ and $\Gamma_i^{ex}$ are the energy and broadening parameters of the interband excitonic transitions, respectively. The fits yield the parameters $A_i^{ex}$, $E_i^{ex}$ and $\Gamma_i^{ex}$. The obtained values of $E_i^{ex}$ indicated as arrows and denoted as $A_1$, $A_2$, $A_R$, B, d and C. The fitted values $E_i^{ex}$ are displayed in Table 1. For undoped $WS_2$, the exciton A Rydberg series can be described by three-dimensional Mott–Wannier excitons. As listed

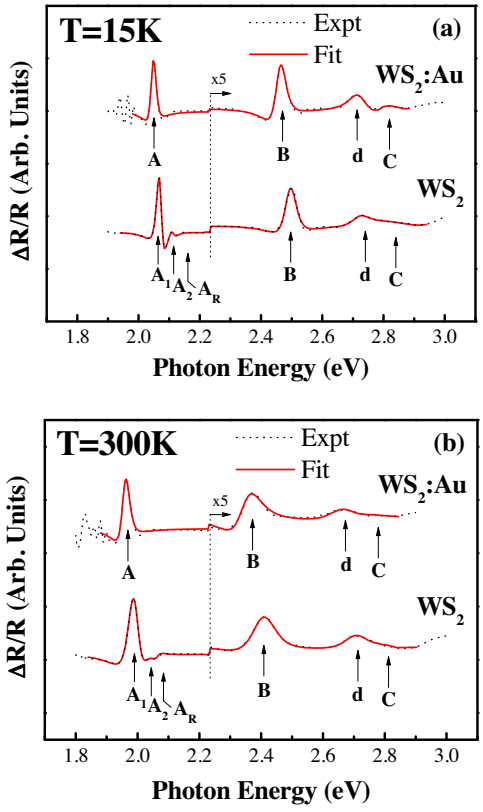


**Fig. 6.** PzR spectra for Au-doped and undoped $WS_2$ at (a) 15 K and (b) room temperature. The dashed curves are the experimental curves and the solid curves are least squares fits to Eq. (1). Arrows under the curves show the energy location for the excitonic features.

in Table 1, the transition energies for the excitons show redshifts due to the presence of a small amount of Au.

## 4. Summary

Single crystals of Au-doped $WS_2$ have been grown by the chemical vapor transport method using bromine as a transport agent. XRD spectra revealed that single crystals of $WS_2$:Au have mixture rhombohedral and hexagonal structure. Two major Raman modes, respectively, at around 353 and 418 were detected, which are consistent with the $E^1_{2g}$ and $E_{1g}$ modes, respectively. The presence of Au impurity has been determined to play a major role in influencing the electrical and optical properties of the doped sample. In SPV spectrum an additional feature located ~50 meV below exciton A has been observed and tentatively assigned to the impurity absorption caused by Au dopant. The redshift of peak positions and

increase of the broadening parameters of the band-edge excitonic features are mainly due to the presence of a small amount of Au.

## Acknowledgements

The authors would like to acknowledge Professor Ying-Sheng Huang and Professor Ching-Hwa Ho for advising and providing materials and experimental equipment at Semiconductor Characterization Laboratory, National Taiwan University of Science and Technology (NTUST).

## References

[1] A. Klein, S. Tiefenbacher, V. Eyert, C. Pettenkofer, W. Jaegermann, Electronic band structure of single-crystal and single-layer $WS_2$: influence of interlayer van der Waals interactions, Phys. Rev. B 64 (2001) 205416.
[2] J.A. Baglio, G.S. Calabrese, D.J. Harrison, E. Kamieniecki, A.J. Ricco, M.S. Wrighton, G.D. Zoski, Electrochemical characterization of p-type semiconducting tungsten disulfide photocathodes: efficient photoreduction processes at semiconductor/liquid electrolyte interfaces, J. Am. Chem. Soc. 105 (1983) 2246–2256.
[3] Y.Q. Zhu, W.K. Hsu, S. Firth, M. Terrones, R.J.H. Clark, H.W. Kroto, D.R. Walton, Nb-doped $WS_2$ nanotubes, Chem. Phys. Lett. 342 (2001) 15–21.
[4] S. Wang, G. Li, G. Du, L. Li, X. Jiang, C. Feng, Z. Guo, S. Kim, Synthesis and characterization of cobalt-doped $WS_2$ nanorods for lithium battery applications, Nanoscale Res. Lett. 5 (2010) 1301–1306.
[5] L. Kronik, Y. Shapira, Surface photovoltage phenomena: theory, experiment, and applications, Surf. Sci. Rep. 37 (1999) 1–5.
[6] F.H. Pollak, H. Shen, Modulation spectroscopy of semiconductors: bulk/thin film, microstructures, surfaces/interfaces and devices, Mater. Sci. Eng. R10 (1993) 275–374.
[7] T.J. Wieting, J.L. Verble, Infrared and Raman studies of long-wavelength optical phonons in hexagonal $MoS_2$, Phys. Rev. B 3 (1971) 4286.
[8] J.M. Chen, C.S. Wang, Second order Raman spectrum of $MoS_2$, Solid State Commun. 14 (1974) 857–860.
[9] T. Sekine, T. Nakashizu, K. Toyoda, K. Uchinokura, E. Matsuura, Raman scattering in layered compound 2H-$WS_2$, Solid State Commun. 35 (1980) 371–373.
[10] C. Sourisseau, M. Fouassier, Resonance Raman, inelastic neutron scattering and lattice dynamics studies of 2H-$WS_2$, Mater. Sci. Eng. B3 (1989) 119–123.
[11] E. Dobardzic, B. Dakic, M. Damnjanovic, I. Miloševic, Raman and infrared-active modes in $MS_2$ nanotubes (M =Mo,W), Phys. Rev. B 74 (2006) 033403.
[12] M. Viršek, A. Jesih, I. Milošević, M. Damnjanović, M. Remškar, Raman scattering of the $MoS_2$ and $WS_2$ single nanotubes, Surf. Sci. 601 (2007) 2868–2872.
[13] A.R. Beal, J.C. Knights, W.Y. Liang, Transmission spectra of some transition metal dichalcogenides. II. Group VIA: trigonal prismatic coordination, J. Phys. C: Solid State Phys. 5 (1972) 3540.
[14] D.E. Aspnes, Optical properties of semiconductors, in: M. Balkanski (Ed.), Handbook on Semiconductors, vol. 2, North-Holland, Amsterdam, 1980, p. 109.
[15] M. Sigiro, Y.S. Huang, C.H. Ho, Y.C. Lin, K. Suenaga, Influence of rhenium on the structural and optical properties of molybdenum disulfide, Jpn. J. Appl. Phys. 54 (2015) 04DH05.
[16] M. Sigiro, Y.S. Huang, C.H. Ching-Hwa, Optical characterization of undoped and Au-doped $MoS_2$ single crystals, Appl. Mech. Mater. 627 (2014) 50–53.
[17] M. Sigiro, M.N. Nasruddin, Growth and optical characterization of $MoS_2$ single crystals with different dopants, Optik 126 (2015) 666–670.

IOP Conference Series: Materials Science and Engineering



# Study of the near band-edge excitonic transition energies of the mixed layered compounds of $Mo_{1-x}W_x Se_2$ single crystals

# Study of the near band-edge excitonic transition energies of the mixed layered compounds of $Mo_{1-x}W_x Se_2$ single crystals

**Mula Sigiro**
Department of Physics Education, Faculty of Teacher Training and Education, Universitas HKBP Nommensen, Medan 20234, Indonesia

mulasigiro@gmail.com

**Abstract**
The temperature dependence of the spectral features in the vicinity of the direct band edge of $Mo_{1-x}W_xSe_2$ single crystals was measured in the temperature range of 25–300 K using piezoreflectance (PzR). The near band-edge excitonic transition energies of the mixed layered compounds of $Mo_{1-x}W_xSe_2$ single crystals determined accurately from a detailed line-shape fit of the PzR spectra. From a detailed line-shape fit of the PzR spectra, the temperature dependence of the energies of the band-edge excitons are determined accurately.

## 1. Introduction

Layered-structure transition metal dichalcogenides have the formula $MX_2$, where M = Mo, W and X=S, Se that exhibit many physical properties with a pronounced two-dimensional character.[1-3] The peculiar properties of these materials result from their layered structure, consisting of mostly covalently bonded X–M–X sheets linked by weak Van der Waals (VdW) forces. The layered transition metal dichalcogenides $MX_2$ semiconductors have been extensively investigated due to the potential application of the materials as solid lubricants, catalysts and photovoltaic solar cell materials.[4-7] Agarwal *et al*. have successfully described the growth and some of the key properties of $Mo_{1-x}W_xSe_2$, $Mo_{0.5}W_{0.5}Se_2$ and $WS_xSe_{2-x}$ single crystals.[8-11] Similar mixed-layered crystals of compounds such as $Mo_xW_{1-x}Se_2$, $Mo_{0.5}W_{0.5}Se_2$ and $Mo_{0.02}W_{0.98}Se_2$ by using various methods have been published.[12-14] Our previously work, $Mo_{1-x}W_xS_2$ single crystals have been experimentally realized to vary their bandgap values and temperature dependence of energies and broadening parameters of the band-edge excitons.[15,16]

In this paper we report a detailed study of the temperature dependence of the piezoreflectance (PzR) measurements in the spectral range near the direct band gap of $Mo_{1-x}W_xSe_2$ single crystals in the temperature range 25–300 K. The PzR spectra are fitted with a form of the Aspnes equation of the first-derivative Lorentzian line shape.[17] From a detailed lineshape fit we are able to determine accurately the energies and broadening parameters of the excitonic transitions.

## 2. Experiment

Single crystals of $Mo_{1-x}W_xSe_2$ solid solutions were grown by chemical-vapour transport method. The chemical transport was achieved with $Br_2$ as transport agent in the amount of about 10 mg/cm$^3$. Prior to the crystal growth the powdered compounds of the series were prepared from the elements (Mo: 99.99%; W: 99.99%; and Se:99.99%) by reaction at 1000 $^0$C for 10 days in evacuated quartz ampoules. To improve the stoichiometry, sulphur 2 mol% in excess was added with respect to the stoichiometry mixture of the constituent elements. The mixture was slowly heated to 1000 $^0$C. This slow heating is necessary to avoid any explosions due to the strongly exothermic reaction between the elements. The growth temperature was

about 1050 °C in a temperature gradient of about 3 °C/cm and the growth time was about 20 days. The crystals had the shape of thin layer plates with a thickness of 20–100 $\mu$m and a surface area of 5–200 mm$^2$. X-ray analysis confirmed that the samples were single-phase materials of two hexagonal structure over the entire range of the W composition *x*. The lattice constants determined for the crystals were practically identical to those of the stoichiometric polycrystalline starting materials.

The PzR measurements were achieved by gluing the thin single crystal specimens on a 0.15 cm thick lead-zirconate-titanate (PZT) piezoelectric transducer driven by a 200 $V_{rms}$ sinusoidal wave at 200 Hz. The alternating expansion and contraction of the transducer subject the sample to an alternating strain with a typical rms $\Delta l/l$ value of ~ $10^{-5}$. A 150 W tungsten-halogen lamp filtered by a 0.25 m monochromator provided the monochromatic light. The reflected light was detected by a silicon detector. The DC output of the silicon photodiode was maintained constant by a servo mechanism of a variable neutral density filter. A dual-phase lock-in amplifier was used to measure the detected signal. Modulated spectra were normalized to the reflectance to obtain $\Delta R/R$. A close-cycle cryogenic refrigerator equipped with a digital thermometer controller was used to control the measurement temperature between 25 and 300 K with a temperature stability of 0.5 K or better.

## 3. Results and discussion

Displayed by the dashed curves in Figs. 1(a) and 1(b) are the PzR spectra in the vicinity of direct band edge for several mixed crystals of $Mo_{1-x}W_xSe_2$ at 25 and 300 K. The nature of the line shape indicates the presence of two oscillators on the high-energy side of the spectra. The oscillations on the lower-energy side are caused by the interference effects. The experimental curves have been fitted to a functional form appropriate for excitonic transitions that can be expressed as a Lorentzian line-shape function of the form.[17]

$$\frac{\Delta R}{R} = \mathrm{Re}\left[\sum_{i=1}^{n} A_i^{ex} e^{j\varphi_i^{ex}} \left(E - E_i^{ex} + j\Gamma_i^{ex}\right)^{-2}\right] \quad , \qquad (1)$$

where $A_i^{ex}$ and $\varphi_i^{ex}$ are the amplitude and phase of the line shape, $E_i^{ex}$ and $\Gamma_i^{ex}$ are the energy and broadening parameters of the interband excitonic transitions, respectively. Shown by the solid curves in Fig. 1 are the least-squares fits using Eq. (1). The fits yield the parameters $A_i^{ex}$, $E_i^{ex}$ and $\Gamma_i^{ex}$. The obtained values of $E_i^{ex}$ are indicated by arrows and denoted as $A_1$, $A_2$ and B in the figures. However, at 300 K (see Fig. 1(b)), only $A_1$ and B features are clearly visible over most of the *x* values except that of $x = 0$, $x = 0.2$, $x = 0.3$ and $x = 0.4$ where a weak shoulder on the higher-energy side of $A_1$ excitonic transitions is visible. The weak shoulder corresponds to the $A_2$ peak. The energies and their splitting of the A, B excitons of $Mo_{1-x}W_xSe_2$ are listed in Table II. For comparison purposes, we have also listed numbers for $MoS_2$,[18,19] $MoSe_2$,[19] $MoTe_2$,[19] $WS_2$,[20,21] $WSe_2$[21] and our previous work of $Mo_{1-x}W_xS_2$.[22]

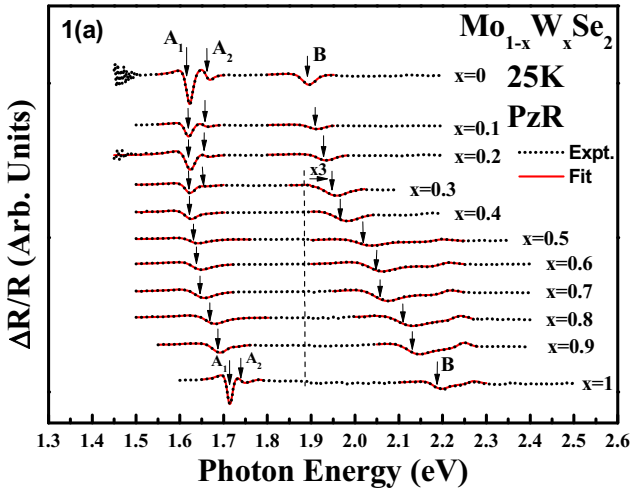


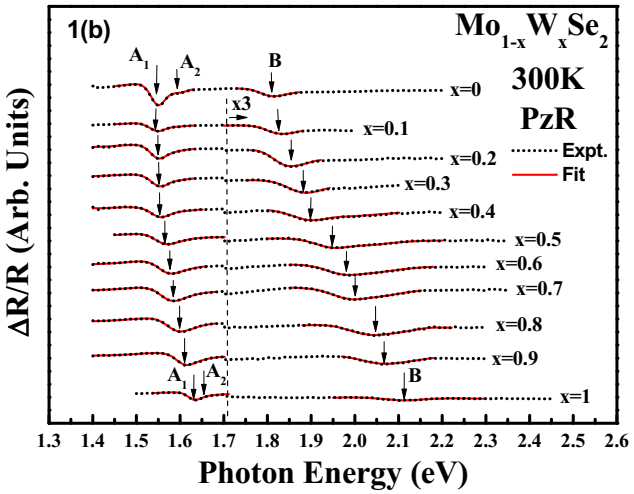


**Figure. 1** The experimental PzR spectra (dashed curves) of $Mo_{1-x}W_xSe_2$ at (a) 25 K and (b) 300 K. The solid curves are least-squares fits to Eq. (1) which yields the excitonic transition energies indicated by the arrows.

**Table.1** Energy of A, B excitons and their splittings in $Mo_{1-x}W_xSe_2$, $Mo_{1-x}W_xS_2$, $MoSe_2$, $MoTe_2$ and $WSe_2$.

| Materials | $E_A$ (eV) | $E_B$ (eV) | $E_{A-B}$ (eV) | Temperature (K) |
|---|---|---|---|---|
| $MoSe_2$[a] | 1.622 ± 0.005 | 1.892 ± 0.008 | 0.270 ± 0.013 | 25 |
| | 1.546 ± 0.008 | 1.799 ± 0.01 | 0.253 ± 0.018 | 300 |
| $MoSe_2$[b] | 1.57 | 1.82 | 0.25 | 300 |
| $Mo_{0.9}W_{0.1}Se_2$[a] | 1.619 ± 0.005 | 1.909 ± 0.008 | 0.290 ± 0.013 | 25 |
| | 1.544 ± 0.008 | 1.816 ± 0.01 | 0.272 ± 0.018 | 300 |

| | | | | |
|---|---|---|---|---|
| $Mo_{0.8}W_{0.2}Se_2$[a] | 1.620 ± 0.005 | 1.929 ± 0.008 | 0.309 ± 0.013 | 25 |
| | 1.550 ± 0.008 | 1.834 ± 0.01 | 0.284 ± 0.018 | 300 |
| $Mo_{0.7}W_{0.3}Se_2$[a] | 1.621 ± 0.005 | 1.947 ± 0.008 | 0.326 ± 0.013 | 25 |
| | 1.552 ± 0.008 | 1.871 ± 0.01 | 0.319 ± 0.018 | 300 |
| $Mo_{0.6}W_{0.4}Se_2$[a] | 1.622 ± 0.005 | 1.966 ± 0.008 | 0.344 ± 0.013 | 25 |
| | 1.553 ± 0.008 | 1.903 ± 0.01 | 0.350 ± 0.018 | 300 |
| $Mo_{0.5}W_{0.5}Se_2$[a] | 1.631 ± 0.005 | 2.018 ± 0.008 | 0.387 ± 0.013 | 25 |
| | 1.555 ± 0.008 | 1.942 ± 0.01 | 0.387 ± 0.018 | 300 |
| $Mo_{0.4}W_{0.6}Se_2$[a] | 1.638 ± 0.005 | 2.044 ± 0.008 | 0.406 ± 0.013 | 25 |
| | 1.561 ± 0.008 | 1.960 ± 0.01 | 0.399 ± 0.018 | 300 |
| $Mo_{0.3}W_{0.7}Se_2$[a] | 1.645 ± 0.005 | 2.057 ± 0.008 | 0.421 ± 0.013 | 25 |
| | 1.569 ± 0.008 | 1.980 ± 0.01 | 0.411 ± 0.018 | 300 |
| $Mo_{0.2}W_{0.8}Se_2$[a] | 1.668 ± 0.005 | 2.110 ± 0.008 | 0.442 ± 0.013 | 25 |
| | 1.583 ± 0.008 | 2.001 ± 0.01 | 0.418 ± 0.018 | 300 |
| $Mo_{0.1}W_{0.9}Se_2$[a] | 1.687 ± 0.005 | 2.130 ± 0.008 | 0.443 ± 0.013 | 25 |
| | 1.600 ± 0.008 | 2.043 ± 0.01 | 0.443 ± 0.018 | 300 |
| $WSe_2$[a] | 1.714 ± 0.005 | 2.187 ± 0.008 | 0.473 ± 0.013 | 25 |
| | 1.629 ± 0.008 | 2.113 ± 0.01 | 0.484 ± 0.018 | 300 |
| 2H-$WSe_2$[c] | 1.71 | 2.30 | 0.59 | 77 |
| $Mo_{0.7}W_{0.3}S_2$[d] | 1.932 ± 0.005 | 2.223 ± 0.008 | 0.291 ± 0.013 | 25 |
| | 1.858 ± 0.008 | 2.168 ± 0.01 | 0.290 ± 0.018 | 300 |
| $Mo_{0.5}W_{0.5}S_2$[d] | 1.943 ± 0.005 | 2.252 ± 0.008 | 0.309 ± 0.013 | 25 |
| | 1.860 ± 0.008 | 2.170 ± 0.01 | 0.310 ± 0.018 | 300 |
| $Mo_{0.3}W_{0.7}S_2$[d] | 1.976 ± 0.005 | 2.333 ± 0.008 | 0.357 ± 0.013 | 25 |
| | 1.902 ± 0.008 | 2.253 ± 0.01 | 0.351 ± 0.018 | 300 |
| $MoS_2$[d] | 1.929 ± 0.005 | 2.136 ± 0.008 | 0.207 ± 0.013 | 25 |
| | 1.845 ± 0.008 | 2.053 ± 0.01 | 0.208 ± 0.018 | 300 |
| $WS_2$[d] | 2.064 ± 0.005 | 2.489 ± 0.008 | 0.425 ± 0.013 | 25 |
| | 1.981 ± 0.008 | 2.401 ± 0.01 | 0.420 ± 0.018 | 300 |
| $WS_2$[e] | 2.06 | 2.47 | 0.41 | 77 |
| | 2.0 | 2.386 | 0.386 | 300 |
| 3R-$WS_2$[f] | 2.06 | 2.50 | 0.44 | 77 |
| $MoTe_2$[g] | 1.71 | 2.30 | 0.59 | 77 |
| $MoS_2$[h] | 1.9255 | 2.137 | 0.2115 | 4.2 |
| $MoS_2$[i] | 1.92 | 2.124 | 0.204 | 4.2 |

[a]this work [d]Reference 22. [g]Reference 19.
[b]Reference 19. [e]Reference 21. [h]Reference 18.
[c]Reference 20. [f]Reference 20. [i]Reference 18.

The A and B exciton peaks near the optical absorption edge are characteristic features of the optical spectra of all layered molybdenum and tungsten dichalcogenides.[22] The nature of the direct gaps has been investigated by studying these exciton pairs. Following Wilson and Yoffe[22] many authors have attributed the A–B exciton pair to transitions at the Γ point, split by spin–orbit splitting, as suggested by the dependence of the splittings on the masses of the constituent elements.

## 4. Conclusions

In conclusions we have measured the temperature dependence of the energies and broadening parameters of the direct band-edge excitonic transitions of $Mo_{1-x}W_xSe_2$ using PzR in the temperature range between 25 and 300 K. The transition energies of A, B excitons and their separation at various temperatures change smoothly with W composition *x*, indicating that the nature of the direct band edges of $Mo_{1-x}W_xSe_2$ are similar, even for $Mo_{1-x}W_xS_2$ . The splitting of excitons A and B for $Mo_{1-x}W_xSe_2$ is larger than $Mo_{1-x}W_xS_2$ at various temperatures.

## Acknowledgements

The author would like to acknowledge Professor Ying-Sheng Huang and Professor Ching-Hwa Ho for advising and providing materials and experimental equipment at Semiconductor Characterization Laboratory, National Taiwan University of Science and Technology (NTUST).

## References

[1] A. R. Beal and J. C. Knights, J. Phys. C: Solid State Phys. **5**, 3540 (1972).
[2] W. Y. Liang, J. Phys. C: Solid State Phys. **6**, 551 (1973).
[3] W. J. Schutte, J. L. De Boer, and F. Jellinek, J. Solid State Chem. **70**, 207 (1987).
[4] P. D. Fleischauer, Thin Solid Films **154**, 309 (1987).
[5] J. M. Martin, C. Donnet, J. Le Mogne, and T. Epicier, Phys. Rev. B **48**, 10583 (1993).
[6] K. K. Kam and B. A. Parkinson, J. Phys. Chem. **86**, 463 (1982).
[7] A. Jager-Waldau, M. Lux-Steiner, R. Jager-Waldau, R. Burkhardt, and E. Bucher, Thin Solid Films **189**, 339 (1990).
[8] M. K. Agarwal and P. A. Wani, Mater. Res. Bull. **14**, 82513 (1979).
[9] M. K. Agarwal, P. A. Wani, and P. D. Patel, J. Cryst. Growth **49**, 693 (1980).
[10] M. K. Agarwal and L. T. Talell, Solid State Commun. **76**, 549 (1986).
[11] M. K. Agarwal, M. N. Vashi, and A. R. Jani, J. Cryst. Growth **71**, 414 (1985).
[12] W.K. Hofmann, H.J. Lewerern, and C. Pettenkofer, Solar Energy Mater. **17**, 165 (1988).
[13] A. A. Patil, P. P. Hankare, A. B. Gaikawad, and K. M. Garadkar, J. Mater. Sci.: Mater. Electron. **23**, 909 (2012).
[14] G. Kline, K. K. Kam, R. Ziegler, and B. A. Parkinson, Solar Energy Mater. **6**, 337 (1982).
[15] Y. Chen, C. Xi, D. O. Dumcenco, Z. Liu, K. Suenaga, D. Wang, Z. Shuai, Y. S. Huang, and L. Xie, ACS Nano **7**, 4610 (2013).
[16] M. Tanaka, H. Fukutani, and G. Kuwabara, Solid State Commun. **26**, 911 (1978).
[17] D. E. Aspnes, in Handbook on Semiconductors, edited by M. Balkanski (North-Holland, Amsterdam), 1980, p. 109
[18] E. Fortin and F. Raga, Phys. Rev. B **11**, 905 (1975).
[19] A. R. Beal, W.Y. Liang, and H.P. Hughes, J. Phys. C: Solid State Phys. **9**, 2449 (1976).
[20] A. R. Beal and H. P. Hughes, J. Phys. C: Solid State Phys. **12**, 881 (1979).
[21] S. J. Li, J. C. Bernede, J. Pouzet, and M. Jamali, J. Phys.: Condens. Matter **8**, 2291 (1996).
[22] J. A. Wilson and A. D. Yoffe, Adv. Phys. **18**, 193 (1969).

# Raman Scattering Characterization of $Mo_xW_{1-x}S_2$ Layered Mixed Crystals

M. Sigiro*

Department of Physics Education, Faculty of Education and Teacher Training, Universitas HKBP Nomensen, Medan 20234, Indonesia

*(Received August 31, 2016; in final form January 5, 2017)*

A series of $Mo_xW_{1-x}S_2$ ($0 \leq x \leq 1$) layered mixed crystals was grown by the chemical vapor transport method. A systematic study of these crystals was then conducted using the Raman scattering measurements. The peaks of the two dominant first-order Raman-active modes, $A_{1g}$ and $E^1_{2g}$, and of several second-order bands are observed from 150 $cm^{-1}$ to 500 $cm^{-1}$. The peaks corresponding to $A_{1g}$ mode show one-mode type behavior, whereas the peaks of $E^1_{2g}$ mode demonstrate two-mode type behavior for the entire series. These results can be explained by the atomic displacements of each mode. For $A_{1g}$ mode, only S atoms vibrate, thereby resulting in a one-mode type behavior for the mixed crystals. For $E^1_{2g}$ mode, metal and S atoms vibrate. The mass difference in the vibrating Mo and W cations causes the two-mode type behavior of $E^1_{2g}$ mode. In addition, the largest asymmetry and broadening of $A_{1g}$ mode for $Mo_{0.5}W_{0.5}S_2$ is attributed to random alloy scattering.

DOI: 10.12693/APhysPolA.131.259

PACS/topics: Raman-active mode, layered mixed crystal, atomic displacement, chemical-vapor transport method

## 1. Introduction

Layered semiconductors $TX_2$ are receiving significant interest because of their structural properties. $MoS_2$ is an important member of layered-type transition metal dichalcogenides, which have a VI-group layer-type structure [1] $MX_2$ (or $WX_2$), where M = Mo or W, and X = S or Se. The "layered" structure of $MoS_2$ is formed by a graphene-like hexagonal arrangement of Mo and S atoms stacked together to achieve S–Mo–S sandwiches, which are coordinated in a triangular prismatic fashion. The S–Mo–S sandwiches are bonded together by weak Van der Waals forces [2]. Layered semiconductors are potential candidates in various important technologies, such as solid lubricants [3–5], photovoltaic and polymer solar cells [6–10], and hydrosulphurization catalysts [11]. The possibility of obtaining $MoS_2$ by exfoliation of multilayered $MoS_2$ into single-layered $MoS_2$nanosheets, followed by a Li-intercalation and exfoliation method [12, 13] allowed the solution-based production and thin-film fabrication of $MoS_2$ sheets, which are applicable in high-performance electronics. In addition, a high in-plane carrier mobility of $\approx 200$ $cm^2$ $V^{-1}$ $s^{-1}$ to 500 $cm^2$ $V^{-1}$ $s^{-1}$ and superior mechanical properties of the $MoS_2$ nanosheets have made them promising materials for various applications in electronic devices [14–17]. Given these versatile properties, many researchers have investigated the utilization of $MoS_2$ as a semiconducting channel material for high-performance unipolar or ambipolar field-effect transistors [14, 18–21]. Over the last two decades, several papers concerning the preparation and characterization of $Mo_xW_{1-x}S_2$ compounds using various methods have been published [22–26]. The X-r has layered-type structure with hexagonal symmetry [22, 23]. The thermal decomposition of thiometallate solid solutions $(NH_4)_2Mo_{1-x}W_xS_4$ in an inert or hydrogen atmosphere yields $Mo_xW_{1-x}S_2$ nanotubes and related structures [24–26]. Using piezoreflectance measurements in the vicinity of the direct band edge, the transition energies were found to vary smoothly with the W composition $x$, thereby indicating that the natures of the direct band edges are similar for the $Mo_xW_{1-x}S_2$ compounds [23].

In this report, we present a systematic Raman scattering study of a series of $Mo_xW_{1-x}S_2$ layered mixed crystals grown using chemical-vapor transport method. The peaks of the two dominant first-order Raman-active modes, $A_{1g}$ and $E^1_{2g}$, and several second-order (SOR) bands were observed. Polarization-dependent measurements in the backscattering configuration were performed to determine the positions of $A_{1g}$ and $E^1_{2g}$ modes at different W composition $x$. The peaks that correspond to $A_{1g}$ mode show one-mode type behavior, whereas the peaks of $E^1_{2g}$ mode demonstrate two-mode type behavior for the entire series. The composition-dependent behaviors of $A_{1g}$ and $E^1_{2g}$ modes are discussed.

## 2. Experimental

Solid solutions of $Mo_xW_{1-x}S_2$ single crystals were grown using chemical-vapor transport method with $Br_2$ as a transport agent. The total charge used in each growth experiment was approximately 10 g. The W and Mo materials were added in such manner that the W composition $x$ changes with respect to increases of the Mo from 0 to 1 with a composition step size $\Delta x = 0.1$. Prior to crystal growing, the powdered compounds of the series were prepared from the elements (Mo: 99.99%,

*e-mail: mulasigiro@gmail.com

W: 99.95%, and S: 99.999%) by reaction at 1000 °C for 10 days in evacuated quartz ampoules, which was sealed at $10^{-6}$ Torr. The ampoule, which contained $Br_2$ ($\approx 5$ mg cm$^{-3}$), was then placed in a three-zone furnace, and the charge was pre-reacted for 24 h at 800 °C with the growth zone at 950 °C, thereby preventing the transport of the product. The temperature of the furnace was increased slowly to avoid any possible explosion caused by exothermic reaction between the elements. The furnace was then equilibrated to achieve a constant temperature across the reaction tube, and then programmed over 24 h to produce the temperature gradient at which single-crystal growth occurred. Optimal results were obtained at a temperature gradient of approximately 960 °C to 930 °C. Single crystalline platelets up to $10 \times 10$ mm$^2$ surface area and 2 mm in thickness were obtained. We do not expect the two solid solutions to be miscible.

The Raman measurements were performed at room temperature using the backscattering configuration on a Renishaw micro-Raman system with 1800 grooves/mm grating (Fig. 1). An optical microscope with a 50× objective was used to focus the laser beam on the sample placed on an $X-Y$ motorized sample stage. A linearly polarized $Ar^+$ laser beam (514.5 nm excitation line) with a power of $\approx$ 1.5 mW was focused into a spot size of $\approx 5$ $\mu$m in diameter. Prior to measurement, the system was calibrated using the 520 cm$^{-1}$ Raman peak of a polycrystalline Si. The time of acquisition of a particular spectral window was optimized for individual sample measurements. Fifty accumulations were performed to obtain a spectrum.

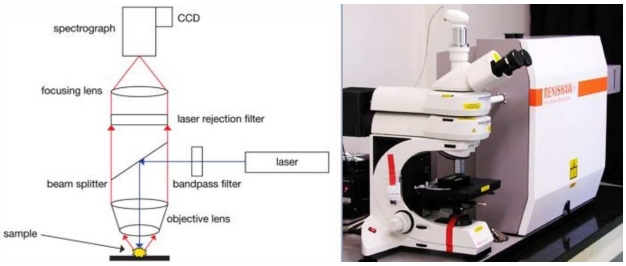


Fig. 1. Schematic diagram of the setup for Raman spectroscopy system.

## 3. Results and discussion

Polarization-dependent measurements in the backscattering configuration were performed to determine the position of $A_{1g}$ and $E^1_{2g}$ modes accurately, as well as the SOR band located in the vicinity of $E^1_{2g}$ of the W-containing samples. The Porto notation method [27] was used for the designation of the crystal and polarization directions. The [1 0 0], [0 1 0], and [0 0 1] crystallographic axes are denoted by the letters $X$, $Y$, and $Z$, respectively. The notation $Z(XX)\bar{Z}$ means that the direction of incident radiation is along the $Z$, the first and second terms in the bracket denotes the polarization of the incident and scattered light, respectively, and $\bar{Z}$ represents the direction of scattered light. For $Z(XX)\bar{Z}$ configuration, the analyzer, which was placed just in front of the charge-coupled device (CCD) camera, was set to have polarization axis that is parallel to the polarization of the incident linearly polarized laser beam. A fine adjustment in the orientation of the [1 0 0] crystallographic axis of the sample to the $\boldsymbol{E}$ vector of the incident linearly polarized laser beam was performed by maximizing the intensity of the $A_{1g}$ mode. The $Z(XX)\bar{Z}$ configuration was obtained simply by placing the half-wavelength plate directly between the analyzer and the CCD camera.

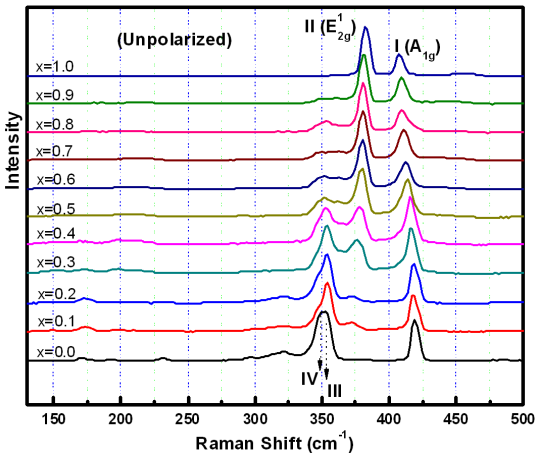


Fig. 2. Unpolarized Raman spectra between 150 and 500 cm$^{-1}$ of $Mo_xW_{1-x}S_2$ layered mixed crystals. The dotted lines guided by eyes show position dependence of the peaks with Mo compositions $x$.

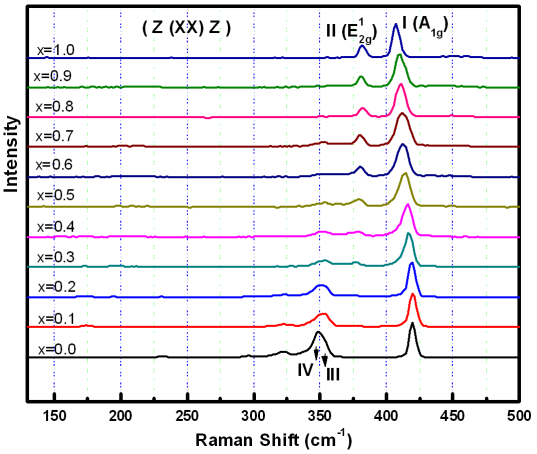


Fig. 3. Polarized Raman spectra between 150 and 500 cm$^{-1}$ of $Mo_xW_{1-x}S_2$ layered mixed crystals. The dotted lines guided by eyes show position dependence of the peaks with Mo compositions $x$.

The results of polarization-dependent Raman spectra between 150 and 500 cm$^{-1}$ of several $Mo_xW_{1-x}S_2$ mixed crystals are shown in Figs. 2 and 3. The intensity of the Raman lines in $Z(XX)\bar{Z}$ and $Z(XY)\bar{Z}$ configurations differ significantly, showing the strong polarization dependence of the first-order Raman-active modes. In

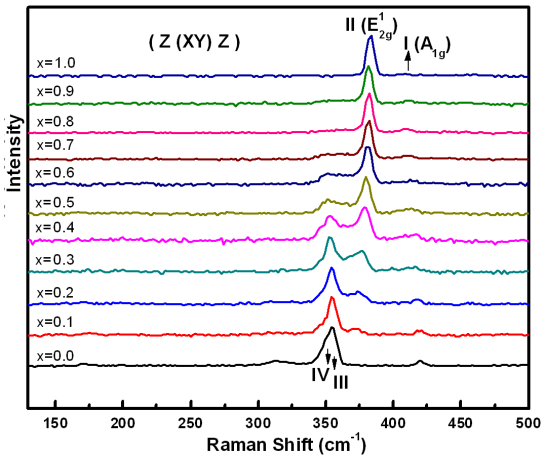


Fig. 4. Raman spectra (between 150 and 500 $cm^{-1}$) of $Mo_xW_{1-x}S_2$ layered mixed crystals for polarized added half wave plate. The dotted lines guided by eyes show position dependence of the peaks with Mo compositions $x$.

this wave number range, for 2H-$MoS_2$ single crystal, the peak denoted by I, which corresponds to $A_{1g}$ mode, is detected for $Z(XX)\bar{Z}$configuration and quenched almost completely for that of $Z(XY)\bar{Z}$ configuration. The lower lying peak denoted by II is associated with $E^1_{2g}$ mode and observed both for $Z(XX)\bar{Z}$ and $Z(XY)\bar{Z}$ polarization configurations. Furthermore, the measured intensities of peak II for both $Z(XX)\bar{Z}$ and $Z(XY)\bar{Z}$ polarization show very similar values. The obtained results, together with the strong polarization dependence, are consistent with the selection rules of $A_{1g}$ and $E^1_{2g}$ modes as given by the Raman scattering tensors [28]. For the 2H-$WS_2$ sample, a similar polarization behavior for higher wave-number peak I is observed and assigned as the $A_{1g}$ mode. The lower lying structure is determined to be composed of two peaks at 356 $cm^{-1}$ (designated as III) and 352 $cm^{-1}$ (designated as IV) in the $Z(XX)\bar{Z}$ configuration. A clear resolution of this structure can be seen in the unpolarized Raman spectrum of 2H-$WS_2$ (Fig. 2), as well as in the $Z(XY)\bar{Z}$ configuration in the polarized spectra (Fig. 3). The relative intensities for peaks III and IV in the $Z(XY)\bar{Z}$ configuration are larger than that of the $Z(XX)\bar{Z}$ configuration. This observation agrees with that reported by Sekine et al. [29]. Hence, the peak at 356 $cm^{-1}$ is assigned as the $E^1_{2g}$ mode, whereas the peak at 352 $cm^{-1}$ is attributed to a SOR band. For the mixed $Mo_xW_{1-x}S_2$ samples, the assignment of peaks I and II can be facilitated by comparing their locations and polarization dependence with that of the binary end crystals. The relation of the relative intensities of peaks III and IV in the polarized Raman spectra were utilized for the assignment (Figs. 3 and 4).

Figure 4 shows the Raman spectra from 150 $cm^{-1}$ to 500 $cm^{-1}$ of $Mo_xW_{1-x}S_2$. From top to bottom, the value of the W composition $x$ increases from 0 to 1 with a composition step size $\Delta x = 0.1$ according to the stoichiometry of the constituent elements W and Mo. With the increase in W composition, peak I moves to higher wave number. By contrast, as the value of $x$ increases, peak II shifts to lower wave number with reduced peak intensity. In addition, with the increase in W composition, on the lower wave number side of the Raman spectra of $Mo_xW_{1-x}S_2$, two additional peaks (III and IV) appear. Both of these additional peaks demonstrate blue shift and become the dominant peaks at higher $x$ values. An alloy disorder-related peak [30], which is positioned between peaks II and III, is also observed for the mixed ternary $Mo_xW_{1-x}S_2$ samples.

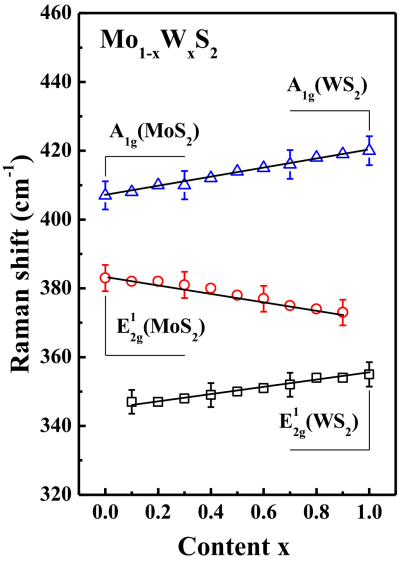


Fig. 5. The dependence of the wave numbers of the Raman-active modes on the composition of $Mo_xW_{1-x}S_2$ layered mixed crystals.

The dependences of the wave numbers of the Raman-active modes on the composition of $Mo_xW_{1-x}S_2$ layered mixed crystals are shown in Fig. 5. For the $A_{1g}$ mode, a one-mode behavior is the most typical, whereas for the $E^1_{2g}$ mode, a two-mode behavior is observed. These experimental results can be explained satisfactorily on the basis of the atomic displacements for each mode. In the $A_{1g}$ mode, only S atoms vibrate, thereby resulting in a one-mode type behavior for the mixed crystals. In the $E^1_{2g}$ mode, metal atoms vibrate, as well as S atoms (Fig. 2). The atomic weight of W atom is 1.92× larger than that of Mo atom, and this mass difference most probably causes two-mode type behavior of $E^1_{2g}$ mode. These composition dependences are often seen in the Raman spectra of solid solutions with no ordered distribution of the constituent atoms [31, 32]; hence, the mixed crystals cannot have an ideal periodic lattice. As the composition of W increases, the disorder effect increases in the layered mixed crystals of $Mo_xW_{1-x}S_2$, and the intensities of the modes related to 2H-$MoS_2$ decreases, whereas the 2H-$WS_2$-associated modes increase. This finite periodicity in the mixed crystals relaxes the $q = 0$ Raman selection

rule, thereby leading to the broadening and asymmetry of the Raman line shape. Symmetric phonon line of the $A_{1g}$ mode for pure 2H-$MoS_2$ and 2H-$WS_2$ become asymmetric for $Mo_xW_{1-x}S_2$ mixed crystals.

Line shape analysis of the Raman spectra under $A_{1g}$ mode for $MoS_2$, $Mo_{0.5}W_{0.5}S_2$, and $WS_2$ layered crystals; the inset in $MoS_2$ represents the W composition dependence of linewidth broadening of $A_{1g}$ mode for the $Mo_xW_{1-x}S_2$ layered mixed crystals. Similar broadening and asymmetry of the phonon lines were previously observed in $TlGa_xIn_{1-x}S_2$ layered mixed crystals [33]. The inset of $Mo_{0.5}W_{0.5}S_2$ shows the composition dependence of the full width at half maximum (FWHM) for $A_{1g}$ mode. The FWHM values of the corresponding modes for $MoS_2$ layered crystals were higher than those for $WS_2$ crystals. In addition, as expected, the FWHM dependence is maximal at $x = 0.5$, which corresponds to the maximum substitution disorder in the mixed crystals.

## 4. Conclusions

The Raman spectra of $Mo_xW_{1-x}S_2$ layered mixed crystals were investigated for a wide range of composition ($0 \leq x \leq 1$). The peaks of the two dominant first-order Raman-active modes, $A_{1g}$ and $E^1_{2g}$, and several SOR bands were observed between 150 $cm^{-1}$ and 500 $cm^{-1}$. The peaks, which correspond to $A_{1g}$ mode, show one-mode type behavior,whereas the peaks of $E^1_{2g}$mode demonstrate two-mode type behavior for the entire series. These results are explained on the basis of the atomic displacements for each mode. For $A_{1g}$ mode, only S atoms vibrate, thereby resulting in a one-mode type behavior for the mixed crystals. By contrast, for the $E^1_{2g}$ mode, metal atoms vibrate, as well as S atoms. The mass difference of the vibrating Mo and W cations causes the two-mode type behavior of the $E^1_{2g}$ mode. The largest FWHM value and asymmetry of $A_{1g}$ mode, which are due to crystal disorder, are found at $x = 0.5$.

## Acknowledgments

The author acknowledge the support of Prof. Ying Sheng Huang and Prof. Ching Hwa-Ho for providing experimental facilities and discussions in Department of Electronic Engineering National Taiwan University of Science and Technology.

## References

[1] J.A. Wilson, A.D. Yoffe, *Adv. Phys.* **18**, 193 (1969).

[2] E.S. Kadantsev, P. Hawrylak, *Solid State Commun.* **152**, 909 (2012).

[3] J.M. Martin, C. Donnet, J.L. Mogne, *Phys. Rev. B* **48**, 10583 (1993).

[4] M. Yanagisawa, *Wear* **168**, 167 (1993).

[5] P.D. Fleuschauer, *Thin Solid Films* **154**, 309 (1987).

[6] H. Tributsch, *Z. Nat.forsch. A* **32**, 972 (1977).

[7] K.K. Kam, B.A. Parkinson, *J. Phys. Chem.* **86**, 463 (1982).

[8] S.J. Li, J.C. Bernede, J. Pouze, M. Jamali, *J. Phys. Condens. Matter* **8**, 2291 (1996).

[9] A. Jager-Waldau, M. Lux-Steiner, R. Jager-Waldau, R. Burkhardt, E. Bucher, *Thin Solid Films* **189**, 339 (1990).

[10] Jin-Mun Yun, Yong-Jin Noh, Jun-Seok Yeo, Yeong-Jin Go, Seok-In Na, Hyung-Gu Jeong, Juhwan Kim, Sehyun Lee, Seok-Soon Kim, Hye Young Koo, Tae-Wook Kim, Dong-Yu Kim, *J. Mater. Chem. C* **1**, 3777 (2013).

[11] P. Grange, B. Delmon, *J. Less-Common Met.* **36**, 353 (1974).

[12] W.M.R. Divigalpitiya, S.R. Morrison, R.F. Frindt, *Thin Solid Films* **186**, 177 (1990).

[13] Z. Zeng, Z. Yin, X. Huang, H. Li, Q. He, G. Lu, F. Boey, H. Zhang, *Angew. Chem. Int. Ed.* **50**, 11093 (2011).

[14] B. Radisavljevic, A. Radenovic, J. Brivio, V. Giacometti, A. Kis, *Nat. Nanotechnol.* **6**, 147 (2011).

[15] A. Ayari, E. Cobas, O. Ogundadegbe, M.S. Fuhrer, *J. Appl. Phys.* **101**, 014507 (2007).

[16] X. Huang, Z. Zeng, H. Zhang, *Chem. Soc. Rev.* **42**, 1934 (2013).

[17] M. Chhowalla, H.S. Shin, G. Eda, L.-J. Li, K.P. Loh, H. Zhang, *Nat. Chem.* **5**, 263 (2013).

[18] H. Li, Z. Yin, Q. He, H. Li, X. Huang, G. Lu, D.W.H. Fam, A.L.Y. Tok, Q. Zhang, H. Zhang, *Small* **8**, 63 (2012).

[19] Z. Yin, H. Li, H. Li, L. Jiang, Y. Shi, Y. Sun, G. Lu, Q. Zhang, X. Chen and H. Zhang, *ACS Nano***6**, 74 (2012).

[20] Y. Zhang, J. Ye, Y. Matsuhashi, Y. Iwasa, *Nano Lett.* **12**, 1136 (2012).

[21] V. Podzorov, M.E. Gershenson, C. Kloc, R. Zeis, E. Bucher, *Appl. Phys. Lett.* **84**, 3301 (2004).

[22] S.K. Srivastava, T.K. Mandal, B.K. Samantaray, *Synth. Met.* 90, 135 (1997).

[23] J.A. van Vechten, T.K. Bergstresser, *Phys. Rev. B* **1**, 3351 (19701).

[24] C. Thomazeau, C. Geantet, M. Lacroix, V. Harlé, S. Benazeth, C. Marhic, M. Danot, *J. Solid State Chem.* **160**, 147 (2001).

[25] C. Thomazeau, C. Geantet, M. Lacroix, M. Danot, V. Harlé, P. Raybaud, *Appl. Catal. A Gen.* **322**, 92 (2007).

[26] M. Nath, K. Mukhopadhyay, C.N.R. Rao, *Chem. Phys. Lett.* **352**, 163 (2002).

[27] T.C. Damen, S.P.S. Porto, B. Tell, *Phys. Rev.* **142**, 570 (1966).

[28] R. Loudon, *Adv. Phys.* **13**, 423 (1964).

[29] T. Sekine, T. Nakashizu, K. Toyoda, K. Uchinokura, E. Matsuura, *Solid State Commun.* **35**, 371 (1980).

[30] S. Ould Saad Hamady, N. Dupuis, J. Décobert, A. Ougazzaden, *J. Cryst. Growth* **310**, 4741 (2008).

[31] M. Ishii, M. Saeki, *Solid State Commun.* **67**, 895 (1988).

[32] I.F. Chang, S.S. Mitra, *Adv. Phys.* **20**, 359 (1971).

[33] N.M. Gasanly, N.S. Yuksek, *Acta Phys. Pol. A* **108**, 997 (2005).

# Effect of gold dopant on structural and optical properties of molybdenum disulfide single crystals

Mula Sigiro

Citation: AIP Conference Proceedings **1855**, 030003 (2017); doi: 10.1063/1.4985473
View online: http://dx.doi.org/10.1063/1.4985473
View Table of Contents: http://aip.scitation.org/toc/apc/1855/1
Published by the American Institute of Physics

# Effect of Gold Dopant on Structural and Optical Properties of Molybdenum Disulfide Single Crystals

Mula Sigiro

*Center of Semiconductor Physics Studies (CSPS) Department of Physics Education*
*Faculty of Teacher Training and Education, Universitas HKBP Nommensen, Medan 20234, Indonesia*
Corresponding author: mulasigiro@gmail.com

**Abstract.** Single crystals of $MoS_2$ doped with gold ($MoS_2$: Au) have been grown by the chemical vapor transport method using iodine as a transporting agent. The transmission electron microscopy (TEM) images showed that doping sites and migration behaviors of Au atoms moved around the $MoS_2$ and jumped with different positions. The doping effects of the materials were characterized by temperature-dependent piezoreflectance (PzR) spectroscopy measurements at temperature of 25 to 300 K. The temperature dependence of the spectral features in the vicinity of direct band-edge excitonic transition of the Au-doped and undoped one was figured out. The energies and broadening parameters of the A and B excitons have been determined accurately via a detailed line shape fit of the PzR spectra. The parameters that describe the temperature variation of the energies and broadening functions of the excitonic transitions are analysed. In addition, the origin of these excitonic transitions is evaluated and discussed. A plausible suggestion will be put forth to explain the role of gold in affecting the variation of the excitonic transitions.

## INTRODUCTION

Molybdenum disulfide ($MoS_2$) is an important member of layered type transition metal dichalcogenides that has a VI- group-layer-type structure [1] $MX_2$ where M = Mo or W and X = S or Se. The ‘‘layered’’ structure of $MoS_2$ is formed by a graphene-like hexagonal arrangement of Mo and S atoms stacked together to give S–Mo–S sandwiches coordinated in a triangular prismatic fashion. The S–Mo–S sandwiches are bonded together by weak Van-der-Waals forces [2]. The material is of interest as a potential candidate in a variety of important technologies such as solid lubricants [3], photovoltaic and polymer solar cells [4, 5], hydrosulphurization catalysts [6]. Recently, the possibility of obtaining $MoS_2$ by exfoliation of multi-layered $MoS_2$ into single-layered $MoS_2$ nanosheets, followed by a Li-intercalation and exfoliation method [7, 8] has allowed the solution-based production and thin-film fabrication of $MoS_2$ sheets that are applicable in high-performance electronics. Due to these versatile properties, many researchers have been intensely investigating the utilization of $MoS_2$ as a semiconducting channel material for high performance unipolar or ambipolar field-effect transistors [9, 10]. Topics investigated commonly deal with the strong anisotropy of physical properties [1] , the role of the *d* orbitals of the transition metal atom in the electronic band scheme [11] and the sharp excitonic structures in the visible region [12, 13]. These structures are generally attributed to the existence of the excitonic transitions A and B characterized by fundamental levels still evident at room temperature. Various assignments for these structures have been proposed both from theoretical band structure calculations [11, 14–16] and experimental measurements [17–19]. Moreover, previous works [20] found several results that X-ray photoelectron spectroscopy showed a slight down shift of the Mo *3d* and S *2p* binding energies, field-emission scanning electron microscopy showed foliate morphology and single crystalline structure, room temperature Hall effect measurement indicated *p*-type semiconducting character for the sample, and the optical transmittance measurements revealed that Au-doped $MoS_2$ is an indirect semiconductor. In this context, the knowledge of how dopant atoms interact with the host TMD lattices is highly important both in fundamental science and future device technology. However, conclusive results concerning origins of these structures have not been obtained. Besides, only few works concerning the effect of the dopants on the temperature dependence study of the excitonic transitions have been reported [21].

*Green Process, Material, and Energy: A Sustainable Solution for Climate Change*
AIP Conf. Proc. 1855, 030003-1–030003-9; doi: 10.1063/1.4985473
Published by AIP Publishing. 978-0-7354-1529-4/$30.00

In this article, we report the transmission electron microscopy (TEM) images of Au-doped and a detailed study of the temperature dependence of the piezoreflectance (PzR) measurements in the spectral range of the A, B excitonic structures of undoped and Au-doped $MoS_2$ single crystals from 25 to 300 K, which were grown by chemical vapour transport method with $I_2$ as the transport agent. Piezoreflectance has been proven to be useful in the characterization of semiconductors [22, 23]. The derivative nature of modulation spectra suppresses uninteresting background effects and greatly enhances the precision in the determination of interband excitonic transition energies. The sharper lineshape as compared to the conventional optical techniques has enabled us to achieve a greater resolution and hence to detect weaker features. The PzR spectra are fitted with a form of the Aspnes equation of the fist derivative Lorenzian lineshape [22, 24]. From a detailed lineshape fit, we are able to determine accurately the energies and broadening parameters of the excitonic transitions. The parameters which describe the temperature behaviour of excitonic transitions indicate that A-B, caused by interlayer interaction and spin-orbit splitting, correspond to excitonic transitions with different origin. The origin of A, B excitons and the effects of dopant are discussed. The temperature variation of the transition energies has been analyzed by the Varshni equation [25] and an expression containing the Bose-Einstein occupation factor for phonons [26, 27]. The temperature dependence of the broadening function also has been studied in term of a Bose-Einstein equation that contains the electron (exciton)-longitudinal optical (LO) phonon coupling constant [26, 27].

## EXPERIMENTAL METHODS

Gold-doped $MoS_2$ single crystals have been grown by the chemical vapour transport method with $Br_2$ as the transport agent. The total charge used in each growth experiment was about 10 g. The stoichiometrically determined weight of the doping material was added in the hope that it would be transported at a rate similar to that of Mo. The quartz ampoule containing $Br_2$ (~5 mg $cm^{-3}$) and uniformly mixed elements (99.99% pure Mo, Au and S) was sealed at $10^{-6}$ Torr. The ampoule was then placed in a three-zone furnace and the charge prereacted for 24 h at 800 $^0$C with the growth zone at 950 $^0$C, preventing the transport of the product. The temperature of the furnace was increased slowly to avoid any possibility of explosion due to the exothermic reaction between the elements. The furnace was then equilibrated to give a constant temperature across the reaction tube, and programmed over 24 hours to produce the temperature gradient at which single-crystal growth took place. Optimal result was obtained with a temperature gradient of approximately 960 $\rightarrow$ 930 $^0$C. Single crystalline platelets of 10 x 10 $mm^2$ surface area and 2 mm in thickness were obtained. We do not expect the two solid solutions to be miscible. It was found that a 5% nominal doping of $MoS_2$ prevented the growth of single crystals.

The high magnification of morphologies of the Au-doped $MoS_2$ was investigated by scanning the transmission electron microscope (STEM). A JEM-2100F equipped with a delta corrector and cold field emission gun was operated at 60 kV in these experiments. Image structures were obtained by density functional theory (DFT) calculation and the corresponding STEM image in fig. 2 of (a) Au adatom on Mo site, (b) Au substitute S atom and Au adatom on hollow center (HC) site, and (c) Au adatom on S site, the annular dark field (ADF) images of each possible positions were occupied by Au atom. The ADF images are processed by Gaussian blur filter to increase the S/N ratio. The simulated atomic structure has been tilted -20° in x-axis and 3° in y-axis.

The PzR measurements were achieved by gluing the thin single crystal specimens on a 0.15 cm thick lead-zirconate-titanate (PZT) piezoelectric transducer driven by a 200 $V_{rms}$ sinusoidal wave at 200 Hz. The alternating expansion and contraction of the transducer subjects the sample to an alternating strain with a typical rms $\Delta l/l$ value of ~ $10^{-5}$. A 150 W tungsten-halogen lamp filtered by a model 270 McPherson 0.35 m monochromator provided the monochromatic light. The reflected light was detected by EG&G type HUV-2000B silicon photodiode. The DC output of the silicon photodiode was maintained constant by a servo mechanism of a variable neutral density filter. A dual-phase lock-in amplifier was used to measure the detected signal. Modulated spectra were normalized to the reflectance to obtain $\Delta R/R$. An RMC model 22 close-cycle cryogenic refrigerator equipped with a model 4075 digital thermometer controller was used to control the measurement temperature between 25 and 300 K with a temperature stability of 0.5 K or better.

## RESULTS AND DISCUSSIONS

Displayed by the dashed curve in Figs. 1(a) and 1(b) are the PzR spectra near the direct band edge over the range 1.65–2.35 eV for the undoped and 1.7–2.25 eV for the Au-doped $MoS_2$ single crystals. The spectra are

characterized by two prominent excitonic transitions, A and B excitons. In the case of undoped $MoS_2$, a higher series of A exciton, denoted as $A_2$, is also detected. In order to determine the position of the transitions accurately, we performed a theoretical line shape fitting. The energies of both excitonic transitions showed the general trend of up-shifting as the temperature was lowered. The linewidths also became narrower in the process. The functional form used in the fitting procedure corresponded to a first derivative Lorenzian line shape function of the form [22, 24].

$$\frac{\Delta R}{R} = \mathrm{Re}\left[\sum_{i=1}^{n} A_i^{ex} e^{j\varphi_i^{ex}} \left(E - E_i^{ex} + j\Gamma_i^{ex}\right)^{-n_i}\right] \quad (1)$$

where $A_i^{ex}$ and $\varphi_i^{ex}$ are the amplitude and phase of the line shape, $E_i^{ex}$ and $\Gamma_i^{ex}$ are the energy and broadening parameters of the interband excitonic transitions and the value of $n_i$ depends on the origin of the transition. For the first derivative functional form, $n$ = 2.0 was appropriate for the bounded states, such as excitons or impurity transition, while $n$ = 0.5 was applicable for three dimensional critical point interband transitions [24]. The least-squares fits using equation (1) with $n$ = *2* can be achieved and the fits are shown as solid curve in fig. 1. The fits yielded the parameters $A_i$, $E_i$ and $\Gamma_i$. The obtained values of $E_i$ were indicated as arrows and denoted as $A_1$, $A_2$ and B. The nomenclature used here followed closely that of Wilson and Yoffe [1] and Beal *et al* [28]. The value of $E_i$ obtained here showed a general agreement with slight deviation from the corresponding low temperature transmission data of Beal *et al* [28]. We believed the derivative nature of the PzR spectra should offer better accuracy. The fitted values of $E_i$ are displayed in table 1 together with the relevant works of [13, 21, 28–30] for comparison. The prominent A and B excitons were observed to be red-shifted. The energy position of A and B excitons were measured accurately with the PzR experiment. The splittings of excitons A and B ($\Delta_{BA} = E_B - E_A$) were determined to be 0.16 ± 0.013 eV for Au-doped $MoS_2$ and 0.216 ± 0.013 for undoped $MoS_2$. These number agreed well with the corresponding previous works [21, 29], transmission data of Beal *et al.* [28], Reflectance [30], and wave length modulated reflectance (WMR) spectra of Fortin and Raga and Photoconductivity [13]. In the case of the WMR data of Fortin and Raga, their observed signature, $B^*$ is almost certain to be due to the presence of 3R-$MoS_2$ in their 2H-$MoS_2$ sample. For undoped $MoS_2$, the excitons A and B Rydberg series can be described by three-dimensional Mott-Wannier excitons [28, 30, 31] which followed closely the relations, $E_n = E_\infty - Rn^{-2}$, where n = 1, 2, 3 … , $E_\infty$ and R were the exciton-series limit and binding energy, the calculated values for exciton A were $E_\infty$ = 1.981 ± 0.02 eV and R = 0.051 ± 0.005 eV. For Au-doped $MoS_2$, only n = 1 Rydberg series for both excitonic transitions were observed. It has been shown that excitons for the three-layer rhombohedral $MoS_2$ are more appropriately described by the two-dimensional Mott-Wannier excitons [28, 30, 31]. The non-detection of higher series is an inherent nature of the two-dimensional Mott-Wannier excitons [30]. The physical origin of the measured difference in the energy splitting of A and B excitons $\Delta_{BA}$ for the Au-doped and undoped $MoS_2$ may be understood as follows. From the more recent theoretical and experimental studies [15, 16, 32], the A and B excitons were attributed to the smallest direct transitions at the K point of the Brillouin zone split by interlayer interaction and spin-orbit splitting [15, 16]. The exciton belongs to $K_4$ to $K_5$ while the B exciton corresponds to $K_1$ to $K_5$ optical transitions. The K states have been shown by Coehoorn *et al* [15, 16] to be predominantly metal *d* states with a small contribution from the non-metal *p* states. Then according to the fig. 2, during growth of Au-doped $MoS_2$, once the Au atom jumps into the S vacancy as a substitutional dopant, it stays much more stable than the other adatom cases, also Au atoms tend to weakly couple to the $MoS_2$ layers as adatoms, while doping with Au atoms may give rise to interesting magnetic properties. On the contrary, the Au adatoms on $MoS_2$ surface give rise to similar mid-gap states at all the three sites (Au-S, Au-Mo and Au-HC). Au dopants in two other positions (as adatoms on HC (Au-HC) sites and in substitutional position at S sites (Au@S)) can also be found, but they are quite rare. Very interestingly, our results suggest that Au adatoms can possess magnetic moments on $MoS_2$ surfaces, so that the introduction of Au impurities may lead to new functionalities of $MoS_2$ and likely other TMDs. One Au-S atom in the single layer region is continuously moving and has a different position in each frame. Another Au atom is found to suddenly jump into the imaging area. The first Au atom continues to migrate in the two-layer region. Although it is not possible for us to say whether the Au atom can be on the top or bottom surface of two layers, the migration behavior of the Au atom can be interpreted without any ambiguity as it is migrating at the inter-layer positions [33, 34]. Moreover, gold nanoparticles on $MoS_2$ were reported to dramatically enhance the photocurrent [35]. In a stark contrast, substituting Mo with Au is highly unfavorable, and the Au atoms are expected to be located predominantly at the adatom sites. Indeed, no Au substitution was found in the experiments. The resulting splitting should open up

slightly if no other mechanisms were involved. This plausible deduction is inferred from other experimental work on mixed crystals of $MoS_2$ with either $WS_2$, $WSe_2$ or $MoSe_2$ where larger anion or cation masses will result in a widening of $\Delta_{BA}$ . However, the measured shrinkage of $\Delta_{BA}$ showed the opposite trend. Other mechanisms such the well known process of intercalation which usually involves a distortion of a crystal structure and a variation of the electronic states of the synthesized compounds [36] may be responsible. It is very likely that Au ions stabilize the 3R polytype of $MoS_2$. The resulting van der Waals forces of 3R-$MoS_2$ should be weaker than the 2H polytype and this is reflected by the measured reduction in $\Delta_{BA}$ .

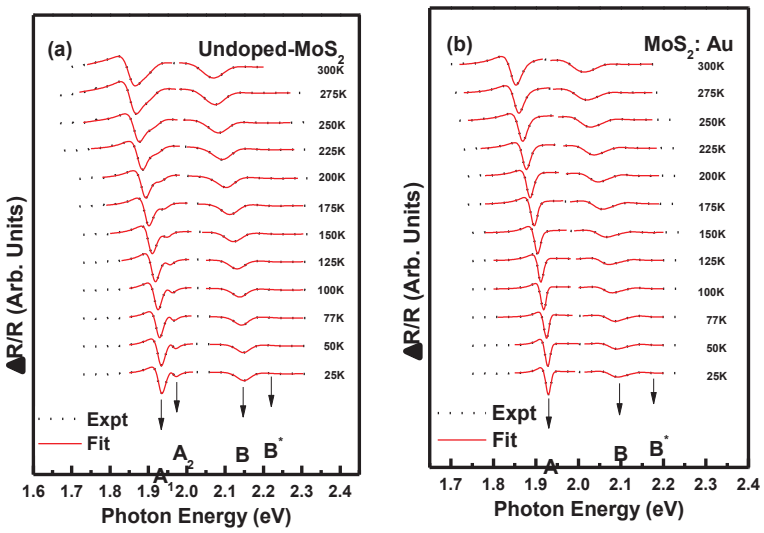


(a) (b)

**FIGURE 1.** Piezoreflectance spectra of (a) undoped and (b) Au-doped $MoS_2$ at several temperatures between 25 and 300K. The dashed curves were the experimental results and the solid curves were least squares fits of Eq. (1).

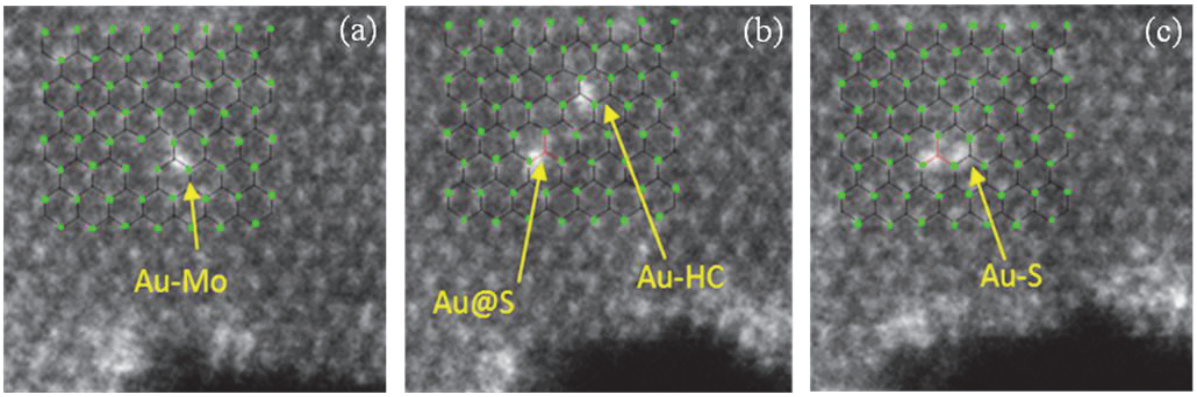


**FIGURE 2.** Image structures obtained by density functional theory (DFT) calculation and the corresponding STEM image of (a)-(c) the ADF images of each possible positions occupied by Au atom.

The temperature variations of the energies of A and B excitons for the doped $MoS_2$ are displayed in fig. 3. The dashed curves in fig. 3 are the least-squares fits to the Varshni empirical relationship [25].

$$E_i(T) = E_i(0) - \frac{\alpha_i T^2}{(\beta_i + T)}, \tag{2}$$

Where $i$ = 1 or 2, $E_i(0)$ is the transition energy at 0 K, and $\alpha_i$ and $\beta_i$ are Varshni coefficients. The constant $\alpha_i$ is related to the electron (exciton)-phonon interaction and $\beta_i$ is closely related to the Debye temperature. For the Au-doped $MoS_2$, the fitted values for exciton A were $E(0)$ = 1.934 ± 0.005 eV, $\alpha$ = 0.39 ± 0.05 meV $K^{-1}$ and $\beta$ = 136 ± 45 K, and for exciton B $E(0)$ = 2.096 ± 0.005 eV, $\alpha$ = 0.43 ± 0.05 meV $K^{-1}$ and $\beta$ = 157 ± 45 K. These numbers are quite similar to other layered structure transition metal dichalcogenide compound [21, 29]. The Debye temperature can be estimated from the Lindemann formula $\Theta_D \approx 120 T_m^{1/2} A^{-5/6} \rho^{1/3}$ [37], where $T_m$ is the melting temperature, A the atomic weight, and $\rho$ is the density of the material. We have computed $\Theta_D$ = 253 K for $MoS_2$ with $T_m$ = 1185 $^0$C [37], A=53.357 g $mol^{-1}$, $\rho$ = 4.8 g $cm^{-3}$ [37]. These number for $\Theta_D$ are in reasonable agreement with the fitted values of $\beta$ as given by equation (2). The temperature dependence of the excitonic transition energies $E_A$(T) and $E_B$(T) of the doped and undoped $MoS_2$ can also be fitted (solid curves in fig. 3) by the expression containing the Bose-Einstein occupation factor for phonon [26, 27].

$$E_i(T) = E_{iB} - a_{iB}\left\{1 + \frac{2}{[\exp(\Theta_{iB}/T) - 1]}\right\}, \tag{3}$$

Where $i$ = 1 or 2, $a_{iB}$ represents the strength of the electron (exciton)-phonon interaction, and $\Theta_{iB}$ corresponds to the average phonon temperature. For the Au-doped samples, the fitted values for exciton A were $E_{AB}$ = 1.931 ± 0.01 eV, $a_{AB}$ = 30 ± 15 meV and $\Theta_{AB}$ = 175 ± 65 K, and for exciton B $E_{BB}$ = 2.092 ± 0.01 eV, $a_{BB}$ = 35 ± 15 meV and $\Theta_{BB}$ = 188 ± 65 K. Again, these values are typical of all layered structure transition metal dichalcogenides [21, 29].

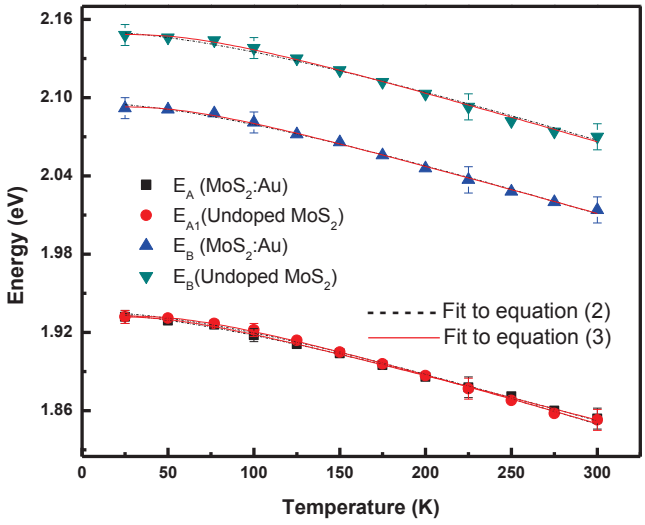


**FIGURE 3.** Temperature variations of the energies of the A-B excitonic pair for undoped and Au-doped $MoS_2$. Representative error bar are shown. The dashed and solid curve are least squares fits to Eq. (2) and (3), respectively.

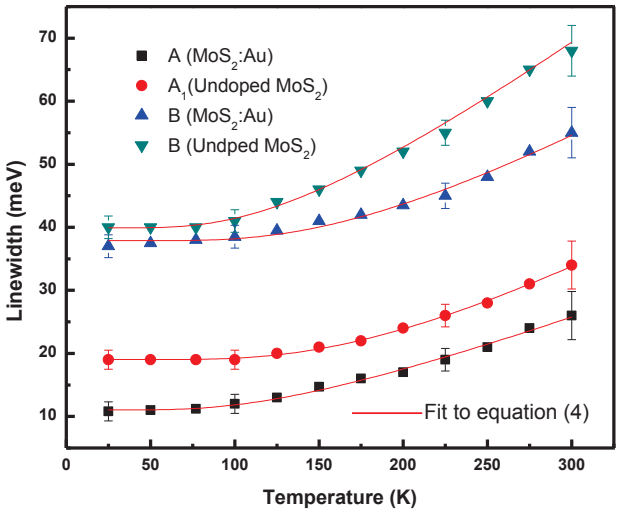


**FIGURE 4.** Temperature variations of the broadening parameters of A and B excitonic transitions for undoped and A-doped $MoS_2$. Representative error bar are shown. The solid cures are least squares fits to Eq (4).

The experimental values of the linewidth $\Gamma_i(T)$ of A and B excitons at several temperatures between 25 and 300 K as obtained from the line shape fit with equation (1) are displayed in fig. 4. Linewidth broadening nearly independent of temperature below 100 K characterizes both excitonic transitions. The temperature independent broadening characteristics of the excitonic transitions for the layered structure transition metal dichalcogenides at temperature below 100 K has been observed previously [13, 21, 29]. The relatively high value of this temperature was attributed to the high value of the exciton reduced mass for the $MoS_2$ crystals [13]. The temperature dependence of the line-width can be expressed as [26, 27]:

$$\Gamma_i(T) = \Gamma_{i0} + \frac{\Gamma_{iLO}}{[\exp(\Theta_{iLO}/T) - 1]}, \tag{4}$$

Where $i$ = 1 or 2. The first term represents the broadening invoked from temperature-independent mechanisms, such as impurity, dislocation, electron interaction, and Auger processes, while the second term was caused by the Fröhlich interaction. The quantity $\Gamma_{iLO}$ represents the strength of the electron (exciton)-LO phonon coupling while $\Theta_{iLO}$ is the LO phonon temperature. The solid curves in fig. 4 represent least-squires fits of the experimental data which enable the evaluation of $\Gamma_{i0}$, $\Gamma_{iLO}$ and $\Theta_{iLO}$ for the excitonic transitions of undoped and Au-doped $MoS_2$. The obtained values of these quantities are listed in table 2 together with the numbers for [21, 29, 38–41] for comparison.

The parameter $\alpha_i$ of equation (2) is related to $a_{iB}$ and $\Theta_{iB}$ of equation (3) by taking the high-temperature limit of both expressions. This yields $\alpha_i \approx 2a_{iB}/\Theta_{iB}$. According to the existing theory [26, 27], this leads to a value of $\Theta_{iB}$ that is significantly smaller than $\Theta_{iLO}$. Our results agreed favorably with the theory [26, 27]. From table 2, the values of $\Gamma_{i0}$ for Au-doped $MoS_2$ for An excitons are slightly smaller than that of the undoped sample, but for B excitons are slightly higher. This means that probably once the Au atom jumped into the S vacancy as a substitutional dopant, it stayed much more stable than the other adatom cases. On the contrary, as has been said earlier, the Au dopant atoms showed extremely high mobility during the observation and easily migrated under the electron beam. Our experimental showed that Au ions stabilized the rhombohedral 3R phase of the $MoS_2$ crystal instead of forming the ternary $Mo_{1-x}Au_xS_2$ system. Our experimental observations thus far supported this assertion. However, from the close similarity of the experimental line shapes and of the fitted parameters, the observed

difference may not be significant enough to account for the effect of gold induced impurity scattering. The apparent ambiguous reasoning is not unreasonable considering the relatively small quantity of dopant. The value of $\Gamma_{i0}$ for the $A_1$ and B excitonic transitions of $MoS_2$ were about 20 and 40, respectively. These values were much larger than those of most semiconductors. The results agreed well the previous reports on GaAs (~20 meV) [41], ZnSe (~24 meV) [40], and $MoS_2$ [13] that reported a detailed study on the excitons in molybdenum disulfide: the results showed that a very large natural broadening nearly independent of temperature below 100 K characterized all the excitonic peaks and a high characteristic temperature $\theta_c$ was deduced from the half width of the $A_1$ and B structures as function of the temperature and was attributed to a high value of the exciton reduced mass. The value of $\Theta_{iLO}$ were quite close to the previous report of the longitudinal optical phonon temperature for $MoS_2$ (557K) obtained from Raman measurements [42]. The close match between the fitted values of $\Theta_{iLO}$ and the LO phonon temperatures obtained from Raman scattering indicated that the temperature variation of $\Gamma_i$ was indeed mainly due to the interaction of the electron with optical phonons. These observations confirmed the existing theory [26, 27], however, a more systematic experimentation should be carried out to verify this property.

**TABLE 1.** Energies of the excitons A, B and their splitting in $MoS_2$, $MoS_2$: Au using equation (1). Relevant values for previous works are included for comparison.

| **Material** | **A (eV)** | **B (eV)** | **$E_{A-B}$ (eV)** | **Temperature (K)** |
|---|---|---|---|---|
| **$MoS_2$:Au** [a] | 1.931 ± 0.005 | 2.091 ± 0.008 | 0.16 ± 0.013 | 25 |
| | 1.926 ± 0.005 | 2.088 ± 0.008 | 0.162 ± 0.005 | 77 |
| | 1.854 ± 0.008 | 2.014 ± 0.01 | 0.16 ± 0.018 | 300 |
| **Undoped $MoS_2$** [a] | 1.932 ± 0.005 | 2.148 ± 0.008 | 0.216 ± 0.013 | 25 |
| | 1.927 ± 0.005 | 2.144 ± 0.008 | 0.217 ± 0.013 | 77 |
| | 1.853 ± 0.008 | 2.070 ± 0.01 | 0.217 ± 0.018 | 300 |
| **$MoS_2$:Re** [b] | 1.915 | 2.066 | 0.151 | 15 |
| **Undoped $MoS_2$** [b] | 1.928 | 2.136 | 0.208 | 15 |
| $MoS_2$ [c] | 1.88 | 2.06 | 0.18 | 300 |
| $MoS_2$ [d] | 1.9255 | 2.137 | 0.2115 | 4.2 |
| $MoS_2$ [e] | 1.92 | 2.124 | 0.204 | 4.2 |
| $MoS_2$ [f] | 1.929 ± 0.005 | 2.136 ± 0.008 | 0.207 ± 0.013 | 25 |
| | 1.845 ± 0.008 | 2.053 ± 0.01 | 0.208 ± 0.018 | 300 |
| 2H-$MoS_2$ [g] | 1.910 | 2.112 | 0.202 | 5 |
| 3R-$MoS_2$ [g] | 1.908 | 2.057 | 0.149 | 5 |

[a]Present work.
[b]PzR [21].
[c]Reflectance [30].
[d]WMR [13].
[e]Photoconductivity [13].
[f]PzR [29].
[g]Transmission [28].

**TABLE 2.** The values of the parameters which describe the temperature dependence of the broadening function of the band-edge excitonic transitions of $MoS_2$: Au and undoped $MoS_2$. Relevant value for previous works and direct band-edge transitions of GaAs and ZnSe are included for comparison.

| **Materials** | **Feature** | $\Gamma_0$ **(meV)** | $\Gamma_{LO}$ **(meV)** | $\Theta_{LO}$ **(K)** |
|---|---|---|---|---|
| Undoped $MoS_2$[a] | $A_1$ | 18.3 ± 1.0 | 77 ± 20 | 562 ± 50 |
| | B | 37.6 ± 2.0 | 76 ± 30 | 562 ± 50 |
| $MoS_2$:Au [a] | $A_1$ | 11.2 ± 1.0 | 55 ± 20 | 450 ± 50 |
| | B | 37.8 ± 2.0 | 85 ± 30 | 572 ± 50 |
| $MoS_2$:Re [b] | $A_1$ | 16.4 ± 1.0 | 85 ± 16 | 510 ± 50 |
| | B | 34.0 ± 1.0 | 90 ± 17 | 520 ± 50 |
| Undoped $MoS_2$[c] | $A_1$ | 18.0 ± 1.0 | 75 ± 20 | 560 ± 50 |
| | B | 37.4 ± 2.0 | 75 ± 35 | 560 ± 50 |
| $ReS_2$ : Au[d] | $E_1^{ex}$ | 5.9 ± 0.5 | 75 ± 15 | 315 ± 100 |
| | $E_2^{ex}$ | 6.8 ± 0.5 | 60 ± 15 | 360 ± 100 |
| $WS_2$ : Au[e] | A | 21 ± 1 | 80 ± 20 | 520 ± 50 |
| | B | 41 ± 2 | 120 ± 30 | 520 ±50 |
| GaAs[f] | $E_d^g$ | 2 | 20 ± 1 | 417 |
| ZnSe[g] | $E_d^g$ | 6.5 ± 2.5 | 24 ± 8 | 360 |

[a]This work. [e]Reference [39].
[b]Reference [21]. [f]Reference [41].
[c]Reference [29]. [g]Reference [40].
[d]Reference [38].

## CONCLUSION

Single crystals of gold-doped and undoped $MoS_2$ have been grown by chemical vapor transport method using iodine as the transporting agent. We have studied the temperature dependence of the energies and broadening parameters of the direct band-edge excitonic transitions of these samples using PzR in the temperature range of 25 to 300 K. From the experimental observations and detailed analysis of the broadening parameters and energies of the excitonic features A and B, we can infer that once the Au atom jumps into the S vacancy as a substitutional dopant, it stays much more stable than the other adatom cases. The TEM results of Au-doped $MoS_2$ propose that the introduction of Au impurities may lead to new functionalities of $MoS_2$ and likely other TMDs. Furthermore, we can infer that Au ions stabilize the formation of 3R-$MoS_2$. As a result, the electronic states of the $MoS_2$ crystals are modified with a reduction of energy splitting of A and B excitons. In addition, the parameters that describe the temperature variation of the energies and broadening function of the interband excitonic transitions were evaluated. The values of $\Gamma_{i0}$ for Au-doped $MoS_2$ for B excitons were slightly higher than that of the undoped sample.

## ACKNOWLEDGMENT

The author would like to acknowledge Professor Ying-Sheng Huang and Professor Ching-Hwa Ho for advising and providing materials and experimental equipment at Semiconductor Characterization Laboratory, National Taiwan University of Science and Technology (NTUST). The author also thanks Prof. Kazu Suenaga and AIST-Japan for providing the STEM image.

## REFERENCES


1. J. A. Wilson and A. D. Yoffe, Adv. Phys. **18**, 193 (1969).
2. E. S. Eugene and P. Hawrylak, Solid State Commun. **152,** 909 (2012).
3. J. M. Martin, C. Donnet, and J. L. Mogne, Phys. Rev. B **48,** 10583 (1993).
4. Tributsch H, Z. Naturf. a **32,** 972 (1977).
5. J. M. Yun, Y. J. Noh, J. S. Yeo, *et al*., J. Mater. Chem. C **1**, 3777 (2013).
6. P. Grange and B. Delmon, J. Less-Common Met. **36**, 353 (1974).
7. W. M. R. Divigalpitiya, S. R. Morrison, and R. F. Frindt, Thin Solid Films **186**, 177 (1990).
8. Z. Zeng, Z. Yin, X. Huang, H. Li, *et al*., Angew. Chem., Int. Ed. **50**, 11093 (2011).
9. B. Radisavljevic, A. Radenovic, J. Brivio, *et al*., Nat. Nanotechnol. **6**, 147 (2011).
10. H. Li, Z. Yin, Q. He, et al., Small **8**, 63 (2012).
11. L. F. Mattheis, Phys. Rev. B **8**, 3719, (1973).
12. M. R. Khan and G. J. Goldsmith, Nuovo Cimento **2D**, 665 (1983).
13. E. Fortin and F. Raga, Phys. Rev. B **11**, 905 (1975).
14. R. V. Kasowski, Phys. Rev. Lett. **30**, 1175 (1973).
15. R. Coehoorn, C. Haas, J. Dickstra , *et al*., Phys. Rev. B **35**, 6195 (1987).
16. R. Coehoorn, C. Haas, and R. A. de Groot, Phys. Rev. B **35**, 6203 (1987).
17. H. Meinhold and G. Weiser, Phys. Status Solidi b **73**, 105 (1976).
18. M. Tanaka, H. Fukutani and G. Kuwabara, Solid State Commun. **26**, 911 (1978).
19. M. Tanaka, G. Kuwabara and H. Fukutani, J. Phys. Soc. Japan **45**, (1899).
20. C. H. Liang, S. Y. Hu, *et al*., ECS Trans. **25**, 183 (2009).
21. K. K. Tiong, T. S. Shou, and C. H. Ho, J. Phys.: Condens. Matter **12**, 3441 (2000).
22. F. H. Pollak and H. Shen, Mater. Sci. Eng. R **10**, 275 (1993).
23. H. Mathieu, J. Allegre, and B. Gil, Phys. Rev. B **43**, 2218 (1991).
24. D. E. Aspnes, *Handbook on Semiconductors: Optical Properties of Semiconductors,* ed. by M. Balkanski (Amsterdam: North-Holland, 1980), Vol. 2, p. 109.
25. Y. P. Varnish, Physica **34**, 149 (1967).
26. P. Lantenschlager, M. Garriga, S. Logothetidis, *et al*., Phys. Rev. B **35**, 9178 (1987).
27. P. Lantenschlager, M. Garriga, L. Vina, *et al*., Phys. Rev. B **36**, 4821 (1987).
28. A. R. Beal, J. C. Knights, and W. J. Liang, J. Phys. C: Solid State Phys. **5,** 3540 (1972).
29. C. H. Ho, C. S. Wu, Y S Huang, *et al*., J. Phys.: Condens. Matter **10**, 9317 (1998).
30. A. R. Beal, W. Y. Liang, and H. P. Huges, J. Phys. C: Solid State Phys. **9,** 2449 (1976).
31. S. L. Chuang, *Physics of Optoelectronic Devices (Wiley Series in Pure and Applied Optics)* ed. by J. W. Goodman (Wiley-Interscience, New York, 1995).
32. T. Straub, K. Fauth, T. Finteis, *et al*., Phys. Rev. B **53**, 16152 (1996).
33. M. Remskar, Z. Skraba, P. Stadelmann, *et al*., Adv. Mater. **12**, 814 (2000).
34. M. Remskar, Z. Skraba, R. Sanjines, *et al*., Surf. Rev. Lett. **6**, 1283 (1999).
35. J. Lin, H. Li, H. Zhang, *et al*., Appl. Phys. Lett. **102**, 203109 (2013).
36. T. Gandke, Ley, and M. Cardona, Phys. Rev. let. 38, 872 (1977); T. Gandke, Ley, and M. Cardona, Phys. Rev. let. 38, 1033 (1977).
37. J. Ziman, *Electrons and Phonons: The Theory of Transport Phenomena in Solids* (Oxford University Press, Clarendon, 1960).
38. D. O. Dumcenco, Y. S Huang, C. H. liang, *et al*., J. Appl. Phys. **104**, 63501 (2008).
39. D.O. Dumcenco, H.P. Hsu, Y.S. Huang, *et al*., Materials Chemistry and Physics **111**, 475 (2008).
40. L. Malikova, W. Krystek, F. H Pollak, *et al*., Phys. Rev. **B** 54, 1819 (1996).
41. H. Qiang, F. H. Pollak, C. M. S. Torres, *et al*., Appl. Phys. Lett. **61**, 1411 (1992).
42. S. I. Uchida and S. Tanaka, J. Phys. Soc. Japan **45**, 153 (1978).

# The influences of load mass changing on inverted pendulum stability based on simulation study

IOP Conf. Series: Materials Science and Engineering **237** (2017) 012005 doi:10.1088/1757-899X/237/1/012005

# The influences of load mass changing on inverted pendulum stability based on simulation study

**Timbang Pangaribuan[1,2], Nasruddin M N[1], Eddy Marlianto[1], Mula Sigiro[3]**
[1]Department of Physics, Faculty of Mathematics and Natural Science, University of North Sumatera, Jl. Bioteknologi No.1, Medan 20155, Indonesia.
[2]Department of Electrical Engineering, Faculty of Engineering, Nommensen HKBP University, Jl. Sutomo No. 4A, Medan 20234, Indonesia.
[3]Department of Physics Education, Faculty of Teacher Training and Education, Nommensen HKBP University, Jl. Sutomo No. 4A, Medan 20234, Indonesia.

* timbang.pbn@gmail.com

**Abstract**. An inverted pendulum has nonlinear dynamic, so it is not easy to do in analysis to see its behavior. From many observations which have been made, there are two things that need to be added on the perfection of inverted pendulum. Firstly, when the pendulum has a large mass, and the second when the pendulum is given a load mass much larger than mass of the inverted pendulum. There are some question, first, how big the load mass can be given so that the movement of the inverted pendulum stay stable is. Second, how weight the changes and moves of load mass which can be given. For all the changes, it hopes the inverted pendulum is stay stable. Finally, the final result is still expected to be as stable, it must need conclude what kind of controller is capable of carrying such a mass burden, and how large the mass load limit can be given.

## 1. Introduction

A behaviour of nonlinear plant on an inverted pendulum can allow the system to become unstable, if its load mass changes suddenly occur on inverted pendulum. The load mass can change with constant values, or it will change depend on time, there is also the burden of mass change all at once moving. The load on cart mass can be made by giving additional load mass after the system is stable. For load mass changes and moves, the movement of that load mass can be done by giving disturbance to the mass of the cart, and it changes depend along with time changes.

If the mass of the cart has changed we can observe the changing of occurring on the position of pendulum, how is that possible to affect the stability of the inverted pendulum. The magnitude of the load mass changes can be made gradually to see the stages of the process, so at last we will find the limit of the mass imposition to the inverted pendulum.

There're so many researchers have designed the stability of an inverted pendulum by using different controllers. One of the techniques was standard pole-placement which proposed by Hari Vasudevan [1]. The controller design was done with the approach of linear system, it has realized to a nonlinear inverted pendulum. The other one has designed the stability of an inverted pendulum by using fuzzy controller which proposed by Ahmad M. El-Nagar [2]. Ronzhina M N [3], have designed the stability of an inverted pendulum by using full feedback from state space techniques, and Sorokin V S [4] has designed stability an inverted pendulum by using swing-up controller techniques. In all these cases, the behavior of the system stability has observed with well, but none of them observe the effect of changing load mass on system stability.

In the other case, the behavior of pendulum's response was observed through giving disturbance and changing the load mass, but the effect of movement of load mass still yet to be observed by them. All those cases have proposed by Prasad at all [5] and Arda and Kuscu [6].

Finally, it needs to observe the effect of mass moving on the stability of the pendulum and analyse the limit of mass on inverted pendulum with a large mass. This paper present a discussion to observe by the influence of changing the load mass on inverted pedulum stability based on simulation study, and expected will give a good contribution to the fields of control systems.

## 1.1 System Details

In addition, there are two purposes of the paper presented. First, the inverted pendulum's dynamic has been relegated separately by author, it has been also controlled and gave the result with a stable response. With reference to Figure1, pendulum is assumed has a limit of movement from $-\theta_L$ to $+\theta_L$, and the action of the cart $x$ is free in movement to stabilise the pendulum with apply the control force F. The action of control force generated by the optimal control techniques, and all the works described here based on simulation. In the beginning of the simulation, the cart mass, $m_c$ is **8** kg, the pendulum mass $m_p$ is **2** kg, the pendulum length, $L$ is **1** m. The numerical work was performed by using a special program which developed by the author on using matlab software.

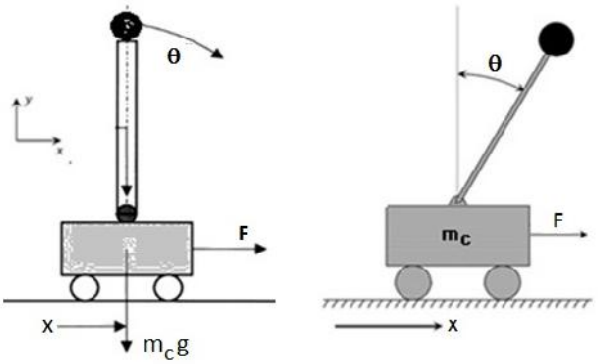


**Figure 1.** General Arrangement of An Inverted Pendulum

Second, based on the topic above, the load mass of the cart can be changed with the constant mass from 8 kg become 18, 28, 38 or 48 kg. The variable load mass can also be varied by using time, as shown the Figure 2 below. Mass of the cart changed and it changed according to a half sinus with magnitude started from 8 to 18, 20, 38 or 38 48 kg.

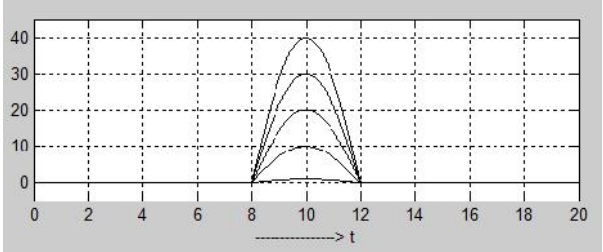


**Figure 2.** Varies of Pendulum's Mass

1.2 Modelling Inverted Pendulum

The dynamics of an inverted pendulum can be derived from its arrangement as shown in Figure 1. It consists of a cart, a pendulum and a driving force unit. The cart uses four wheels can move left or right on the floor freely. The pendulum is placed on the centre of the top surface of the cart. The cart able to rotate to the left or right as like as the cart movement. If all frictions are neglected on the system, the dynamic equation of the inverted pendulum have two equations as expressed below:

$$\ddot{\theta}(t) = \frac{m_p \dot{\theta}^2 \mathrm{c}\quad \theta \mathrm{s}\quad \theta - (m_p + m_c)\frac{g}{L}\,\mathrm{s}\quad \theta - \frac{\mathrm{c}\quad \theta}{L} F}{(-1 + c\quad ^2\theta)\, m_p - m_c} \tag{1}$$

$$\ddot{x}(t) = \frac{L\,\dot{\theta}^2\,\mathrm{s}\quad \theta - (m_p + m_c)\, g\ \mathrm{t}\quad \theta - F}{(-1 + c\quad ^2\theta)\, m_p - m_c} \tag{2}$$

¯ is the the position of pendulum, $\boldsymbol{x}$ is the position of the cart. The initial position of pendulum was ¯ = ¯$_0$ in the unit (rad), the initial position of the cart with $\boldsymbol{x} = \boldsymbol{x}_0 = 0$ in the unit (m). The parameters $\boldsymbol{m_c}$ and $\boldsymbol{m_p}$ are respectively by the mass of the cart and pendulum in the unit (kg), and $\boldsymbol{g}$ = 9,81 (m/s$^2$) is the grafity acceleration.

1.3 Optimal Control Design

From the dynamics of inverted pendulum equation (1) and (2), it needs an approach to generate the linear form with asumtions: for small ¯, the value of sin ¯ = ¯, and the value of cos ¯=Z=N=For those asumtions, the dynamics of inverted pendulum have changed into the equation (3) and (4) below:

$$\ddot{\theta}(t) = \frac{(m_p + m_c)\frac{g}{L}\theta - \frac{1}{L}F}{m_c} \tag{3}$$

$$\ddot{x}(t) = \frac{m_c\, g\, \theta - F}{m_c} \tag{4}$$

$$\begin{bmatrix} \dot{x_1} \\ \dot{x_2} \\ \dot{x_3} \\ \dot{x_4} \end{bmatrix} = \begin{bmatrix} 0 & 1 & 0 & 0 \\ \frac{(m_p + m_c)\, g}{L\, m_c} & 0 & 0 & 0 \\ 0 & 0 & 0 & 1 \\ \frac{m_p\, g}{m_c} & 0 & 0 & 0 \end{bmatrix} \begin{bmatrix} x_1 \\ x_2 \\ x_3 \\ x_4 \end{bmatrix} + \begin{bmatrix} 0 \\ \frac{1}{L\, m_c} \\ 0 \\ \frac{1}{m_c} \end{bmatrix} F \tag{5}$$

Equation (5) has the general form with $\dot{x} = A\,x + B\,u$. By using the Riccati's equation [9] to design the optimal feedback, we can choose the weight $\boldsymbol{Q}$ and $\boldsymbol{R}$ as below:

$$Q = [20\ 0\ 0\ 0\ ;\quad 0\ 1\ 0\ 0\ ;\quad 0\ 0\ 20\ 0\ ;\quad 0\ 0\ 0\ 1]^T \text{ and } R = [1]$$

We found the optimal feedback gain by using the matlab's command,

$$K = [k_1 \quad k_2 \quad k_3 \quad k_4] = \mathrm{lqr}\,(A, B, Q, R) \tag{6}$$

and the result was $K = [32.6220\ \ 6.8964\ \ -1.4142\ \ -2.4721]$.

On insertion of those gain feedback in the form of closed loop system with $\boldsymbol{r}$(t) is the reference intput, the control force is,

$$F(t) = r(t) - K\,x(t) \tag{7}$$

Finally, the equation (8) and (9) are obtained for the closed loop system dynamics:

$$\ddot{\theta}(t) = \frac{m_p \dot{\theta}^2 \mathrm{c}\quad \theta\, \mathrm{s}\quad \theta - (m_p + m_c)\frac{g}{L}\,\mathrm{s}\quad \theta - \frac{\mathrm{c}\quad \theta}{L}\left[k_1\,\theta + k_1\dot{\theta} + k_3\,x + k_4\,\dot{x}\right]}{(-1 + c\quad ^2\theta)\,m_p - m_c} \tag{8}$$

(1)

$$\ddot{x}(t) = \frac{L\,\dot{\theta}^2\,\mathrm{s}\quad \theta - (m_p + m_c)\,g\ \mathrm{t}\quad \theta - \left[k_1\,\theta + k_1\dot{\theta} + k_3\,x + k_4\,\dot{x}\right]}{(-1 + c\quad ^2\theta)\,m_p - m_c} \tag{9}$$

The examination of equations (8) and (9) have been done with $r = 0$ and the initial conditions $x(0) = \left[\frac{\pi}{8}\quad 0\quad 0\quad 0\right]^T$. It shows the state variables of inverted pendulum are coupled.

1.4 The Comparison Between Nonlinear and Linear Dynamics

If we applied the optimal feedback gain from the equation (7) for the linear system as given in equation (3) and (4), we can express both equations as below:

$$\ddot{\theta}(t) = \frac{(m_p + m_c)\frac{g}{L}\theta - \frac{1}{L}\left[k_1\,\theta + k_1\dot{\theta} + k_3\,x + k_4\,\dot{x}\right]}{m_c} \tag{10}$$

$$\ddot{x}(t) = \frac{m_c\,g\,\theta - \left[k_1\,\theta + k_1\dot{\theta} + k_3\,x + k_4\,\dot{x}\right]}{m_c} \tag{11}$$

The responses of the linier system $\theta(t)$ and $x(t)$ from equation (10) and (11) must resemble to the nonlinear system from equation (8) and (9), then the error between the responses nonlinear and linear system must be as small as possible.

## 2. Simulation

In the first step of the simulation, the initial position responses of pendulum and cart showed by the Figure 3. The simulations carried out by using Runge-Kutta integration.

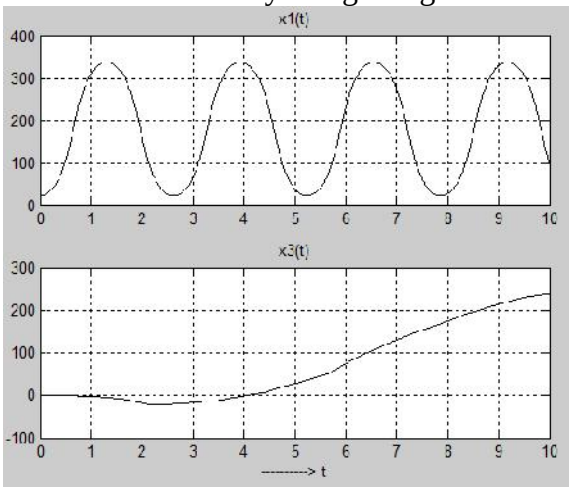


**Figure 3.** Initial Responses of Inverted Pendulum's Positions

$x_1(t)$ is $\theta(t)$ in degree ($^o$), $x_3(t)$ is $x(t)$ in (m). From the results, it can be seen that the pendulum will continue oscillating from 22.5$^o$ to 337.5$^o$. The movement of the cart starts from zero to infinity, so the pendulum and cart position become unstable.

In the second step of the simulation, it shows the optimal respond the linier and nonlinear system according to the Figure 4.

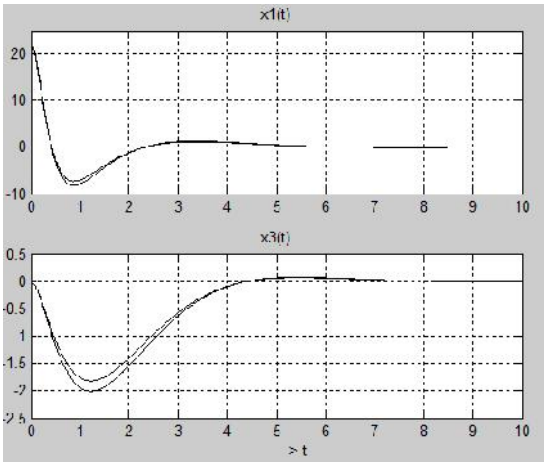


**Figure 4.** Comparison of Responses of Linear and Nonlinear System

From the results, we saw the response of the pendulum and the cart will be continued toward zero. These all responses mean, the system has stable, the both responses toward equilibrium pont. The position error between nonlinear and linear response are calculated by sum of square error, and those equal to 0.4865 % and 0.9815 % for each for the pendulum error and the cart error. Both the error are small enough, and all the responses are eligible.

## 3. The Influence of Load Mass Changes

The change of the load mass from 8 kg to 18, 28, 38 and 48 kg was appiled as given in Figure 5. It seems the response of the pendulum and cart for the different mass was stay stable.

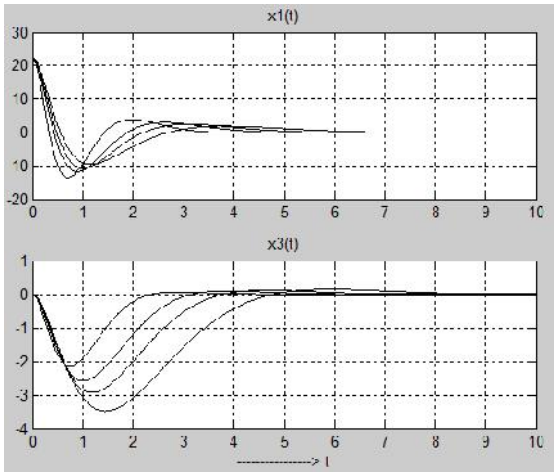


**Figure 5.** The effect of cart's mass change on position response

When the change of a different load mass appiled to the cart of inverted pendulum, the respon of position was found as shown in Figure 6. All responses show that all load mass changes can be overcome by controller, so the the inverted pendulum always stay stable, and the inverted pendulum has already designed to a strong controller.

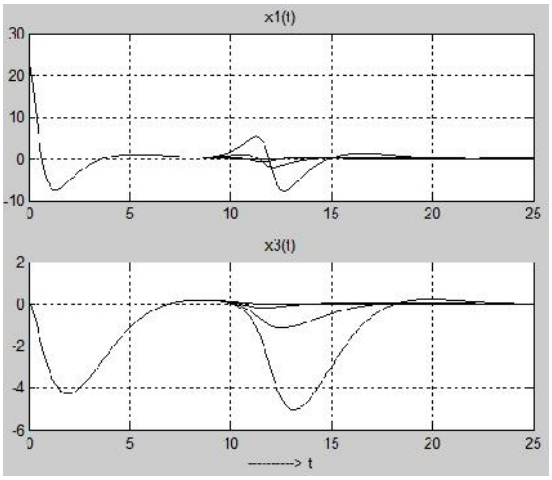


**Figure 6.** The effect of mass load disturbance changes on pendulum's position

## 4. Conclusion

As we have described in the introduction, we need to observe the influences of load mass moving on the stability of pendulum and analyse the limit of mass on inverted pendulum with a large mass, according to the given result on Figure 5 and Figure 6 we can say that we have producted a strong controller with big power and automatic. The limit of load mass which given by the cart has reached 50 kg.

Lastly, the controller has been designed to the strong controller by using the optimal techniques. The weight for optimal conditions to be selected with trial and error several times, so we found the best feedback gain to eliminate all the disturbances.

## References

[1] Hari Vasudevan 2015 Design For Control Of Wheeled Inverted Pendulum Platforms (Journal of Mechanisms and Robotics Volume 7) (ASME)
[2] Ahmad M. El-Nagar 2013Intelligent Control For Nonlinear Inverted Pendulum based On Interval Type-2 Fuzzy PD Controller (Department of Industriial Electronics and Control Engineering) (Menof: Elsevier)
[3] Ronzhina M N 2015 Optimal Conditions With Chattering In The Inverted Two-Link Pendulum Control Problem (Lomonosov Moscow State University) (Moscow: Elsevier)
[4] Sorokin V S 2014 Analysis of Motion Of Inverted Pendulum With Vibrating Suspension Axis At Low-Frequency Excitation (Institute of Problems In Mechanical Engineering) (Moscow: Elsevier)
[5] Lal Bahadur Prasad, Barjeev Tyagi, Hari Om Gupta 2012 Modelling & Simulation for Optimal Control of Nonlinear Inverted Pendulum Dynamical System using PID Controller & LQR (Rorkee: Sixth Asia Modelling Symposium) p138-143
[6] Arda M, Kuscu H 2012 Modelling of the Two Dimensional Inverted Pendulum in Matlab/Simulink (Prague Czech Republic: Proceding of 5th International Mechanical Engineering Forum) p 116-126
[7] Bahram Shahian, Micahel Hassul 1993 Control System Design Using Matlab (London: Prentice-Hall International Inc)
[8] Stanislaw H Zak 2003 System and Controls (New York: Oxford Univeristy Press)
[9] Katsuhiko Ogata 2010 Modern Control Engineering Fifth Edition (Boston: Prentice-Hall)

IOP Conference Series: Materials Science and Engineering



# Piezoreflectance study of Nb-doped $MoS_2$ single crystals

# Piezoreflectance study of Nb-doped $MoS_2$ single crystals

**Kerista Sebayang[1] and MulaSigiro[2,*]**
[1]Department of Physics, Faculty of Mathematics and Natural Sciences, University of Sumatera Utara, Medan 20155, Indonesia.
[2]Department of Physics Education, Faculty of Teacher Training and Education, Universitas HKBP Nommensen, Medan 20234, Indonesia.

* mulasigiro@gmail.com

**Abstract.** We have measured the temperature dependence of the spectral features in the vicinity of direct band-edge excitonic transition of the Nb-doped $MoS_2$ single crystals from 25 to 300 K using piezoreflectance (PzR). The energies and broadening parameters of the A and B excitons of the Nb-doped $MoS_2$ samples have been determined accurately via a detailed line shape fit of the PzR spectra. we can infer that the Nb ions are most likely intercalated between the van der Waals gap and stabilize the rhombohedral 3R phase of the $MoS_2$ crystal.

## 1. Introduction

Molybdenum disulphide $MoS_2$ belongs to the group IVA layer type transition metal dichalcogenides having $C_7$ type crystal structure which is formed of unit layers consisting of transition metal (Mo) atoms sandwiched by chalcogen (S) atoms [1]. The $MoS_2$ compound has been extensively investigated because of the possible practical application as a solid state lubricant and a catalyst for hydrodesulfurization (HDS) and hydrogen evolution reaction (HER) [2-4], photoelectrochemical solar cells [5-6] , and can also be synthesized in large scale by chemical vapor deposition [7-11]. The monolayer $MoS_2$ single crystal exhibits high luminous energy photoconversion efficiencies [12-13], excellent electrical [14-16] and optical performance [17, 18] compared to its bulky counterpart. The successful application of this semiconductor compound originates largely from the sandwich interlayer structure, loosely bound by the weak van der Waals forces, as evidenced by easy cleavage in the c-direction along which the S-Mo-S layers are stacked to form the crystal [1, 19]. There are two known polytypes of $MoS_2$ [1, 19]; two-layer hexagonal and three-layer rhombohedral termed 2H and 3R, respectively. Both have regular layered structures with six-fold trigonal prismatic coordination of the Mo atoms by the sulfur atoms within the layers; 2H-$MoS_2$ has two layers per unit cell stacked in the hexagonal symmetry and belongs to the space group $D_6^4$ while 3R-$MoS_2$ has three layers in the c-direction but has rhombohedral symmetry and belongs to the space group $C_3^5$ . Naturally occurring 3R-$MoS_2$ has been found to be consistently rich in certain minor elements such as Re, Nb etc [20]. The incorporation of the impurity will essentially influence the structure symmetry of $MoS_2$, this is the adoption of the polytype 3R-$MoS_2$. For Nb-doped $MoS_2$, the niobium substitutions improve the photocurrent gain much more slowly than in the case of rhenium [21]. Niobium dopants seems to serve more than just as an impurity donor, it is most likely that niobium transition ions can either substitute for the Mo metal ions interstitially or intercalate between the Vander Waals gap resulting in a distortion of crystal structure [20, 21]. The sandwich Nb ions create stronger bonds than the original van der Waals forces and transform the two-layer hexagonal $MoS_2$ (2H-$MoS_2$) into three-layer rhombohedral $MoS_2$ (3R-$MoS_2$). The transformation of 2H-$MoS_2$ into 3R-$MoS_2$ by doping with niobium is perhaps not too surprising as it has been found that naturally

occurring 3R-$MoS_2$ is consistently rich in certain minor elements such as Nb, Re etc [21]. Despite the potentially attractive fundamental research offered by Nb-doped $MoS_2$, very few studies concerning the influence of niobium dopant on the electrical and optical properties of the material have been reported.

In this study, we present piezoreflectance (PzR) measurements which has been proven to be useful in the characterization of semiconductors [22, 23] of Nb-doped $MoS_2$ which grown by chemical vapor transport method with $I_2$ as transport agent. An elaborate temperature dependence of the spectral features near the direct band-edge excitonic transitions of the Nb-doped $MoS_2$ in the range 25 to 300 K has been obtained. The derivative nature of modulation spectra suppresses uninteresting background effects and greatly enhances the precision in the determination of inter band excitonic transition energies. The sharper line shape as compared to the conventional optical techniques has enabled us to achieve a greater resolution and hence to detect weaker features. The PzR spectra are fitted with a form of the Aspnes equation of the fist derivative Lorenzian lineshape [23, 24]. From a detailed lineshape fit we are able to determine accurately the energies and broadening parameters of the excitonic transitions. The parameters which describe the temperature behaviour of excitonic transitions indicate that A-B, caused by interlayer interaction and spin-orbit splitting, correspond to excitonic transitions with different origin. The origin of A, B excitons and the effects of dopant are discussed. The temperature variation of the transition energies has been analyses by the Varshni equation [25] and an expression containing the Bose-Einstein occupation factor for phonons [26,27]. The temperature dependence of the broadening function also has been studied in term of a Bose-Einstein equation that contains the electron (exciton)-longitudinal optical (LO) phonon coupling constant [26,27]. The addition of dopant impurities to a semiconductor is what enables the fabrication of a multitude of interesting devices. The physical role of niobium in influencing the electronic states of the $MoS_2$ crystal will also be discussed.

## 2. Experimental

Niobium-doped $MoS_2$ single crystals have been grown by the chemical vapour transport method with $I_2$ as a transport agent. The total charge used in each growth experiment was about 10 g. The stoichiometrically determined weight of the doping material was added in the hope that it would be transported at a rate similar to that of Mo. The quartz ampoule containing $Br_2$ (~5 mg $cm^{-3}$) and uniformly mixed elements (99.99% pure Mo, Nb and S) was sealed at $10^{-6}$ Torr. The ampoule was then placed in a three-zone furnace and the charge prereacted for 24 h at 800 $^0$C with the growth zone at 950 $^0$C, preventing the transport of the product. The temperature of the furnace was increased slowly to avoid any possibility of explosion due to the exothermic reaction between the elements. The furnace was then equilibrated to give a constant temperature across the reaction tube, and programmed over 24 h to produce the temperature gradient at which single-crystal growth took place. Optimal result were obtained with a temperature gradient of approximately 960 → 930 $^0$C. Single crystalline platelets up to 10 x 10 $mm^2$ surface area and 2 mm in thickness were obtained. After 24 h, the furnace was allowed to cool down slowly (40$^0$C/h) to about 200$^0$C.

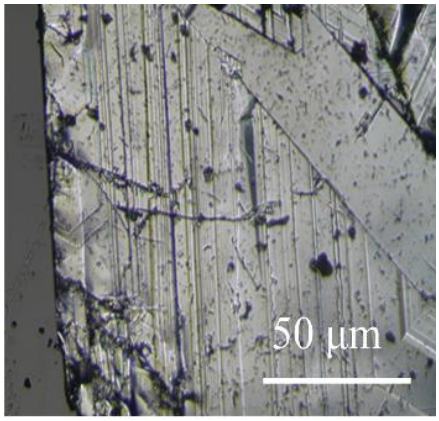


**Figure. 1** Photograph of the as-grown niobium-doped $MoS_2$ single crystal with the surface normal to ***c***-axis

The ampoule was then removed and wet tissues applied rapidly to the end away from the crystals to condense the $I_2$ vapor. When the ampoule reached room temperature, it was opened and the crystals removed. The crystals were then rinsed with acetone and deionized water. Single crystalline platelets up to $10\times10$ mm$^2$ surface area and 2 mm in thickness were obtained. The as-grown niobium-doped $MoS_2$ single crystal is shown in Fig.1. $MoS_2$ crystallizes with 2H or 3R structure, while $NbS_2$ crystallizes in a distorted C6 structure, so that only a small solubility range is to be expected. We do not expect the two solid solutions to be miscible. It was found that a 5% nominal doping of $MoS_2$ prevented the growth of single crystals.

The PzR measurements were achieved by gluing the thin single crystal specimens on a 0.15 cm thick lead-zirconate-titanate (PZT) piezoelectric transducer driven by a 200 $V_{rms}$ sinusoidal wave at 200 Hz. The alternating expansion and contraction of the transducer subjects the sample to an alternating strain with a typical rms $\Delta l/l$ value of ~ $10^{-5}$. A 150 W tungsten-halogen lamp filtered by a model 270 McPherson 0.35 m monochromator provided the monochromatic light. The reflected light was detected by EG&G type HUV-2000B silicon photodiode. The DC output of the silicon photodiode was maintained constant by a servo mechanism of a variable neutral density filter. A dual-phase lock-in amplifier was used to measure the detected signal. Modulated spectra were normalized to the reflectance to obtain $\Delta R/R$. An RMC model 22 close-cycle cryogenic refrigerator equipped with a model 4075 digital thermometer controller was used to control the measurement temperature between 25 and 300 K with a temperature stability of 0.5 K or better.

## 3. Results and Discussions

Displayed by the dashed curve in Fig. 2 are the PzR spectra near the direct band edge over the range 1.7-2.25 eV for the Au-doped $MoS_2$ single crystals. The spectra are characterized by two prominent excitonic transitions, A and B excitons. In order to determine the position of the transitions accurately, we performed a theoretical line shape fitting. The energies of both excitonic transitions show the general trend of up-shifting as the temperature is lowered. The linewidths also become narrower in the process. The functional form used in the fitting procedure correspons to a first derivative Lorenzian line shape function of the form [23, 24]

$$\frac{\Delta R}{R} = \mathrm{Re}\left[\sum_{i=1}^{n} A_i^{ex} e^{j\,\ddot{}_i^{ex}} \left(E - E_i^{ex} + j\Gamma_i^{ex}\right)^{-n_i}\right] \quad (1)$$

where $A_i^{ex}$ and $\ddot{}_i^{ex}$ are the amplitude and phase of the line shape, $E_i^{ex}$ and $\Gamma_i^{ex}$ are the energy and broadening parameters of the inter band excitonic transitions and the value of $n_i$ depend on the origin of the transition. For the first derivative functional form, $n$ = 2.0 is appropriate for the bounded states, such as excitons or impurity transition, while $n$ = 0.5 is applicable for three dimensional critical point inter band transitions [28]. The least-squares fits using equation (1) with $n = 2$ can be achieved and the fits are shown as solid curve in figure 1.The fits yield the parameters $A_i$, $E_i$ and $\Gamma_i$. The obtained values of $E_i$ are indicated as arrows and denoted as A and B. The nomenclature used here follows closely that of Wilson and Yoffe [1] and Beal *et al* [29]. The value of $E_i$ obtained here show a general agreement with slight deviation from the corresponding low temperature transmission data of Beal *et al* [29]. We believed the derivative nature of the PzR spectra should offer better accuracy. The fitted values of $E_i$ are displayed in table 1 together with the relevant works of [29-33] for comparison. The prominent A and B excitons are observed to be red-shifted. The energy position of A and B excitons are measured accurately with the PzR experiment. The splittings of excitons A and B ($\Delta_{BA} = E_B - E_A$) are determined to be 0.16 ± 0.013 eV. These number agreed well with the corresponding previously work [31,32], transmission data of Beal *et all* [29], Reflectance [33], Wavelength modulated reflectance (WMR) spectra of Fortin and Raga and Photoconductivity [30]. In the case of the WMR data of Fortin and Raga, their observed signature, $B^*$ is almost certain to be due to the presence of 3R-$MoS_2$ in their 2H-$MoS_2$ sample. From the more recent theoretical and experimental studies [34-36], the A and B excitons are attributed to the smallest direct transitions at the K point of the Brillouin zone split by interlayer interaction and spin-orbit splitting [34, 35]. The A exciton belongs to $K_4$ to $K_5$ while the B exciton corresponds to $K_1$ to $K_5$ optical transitions. The K states have been shown by Coehoorn *et al* [34, 35] to be predominantly metal *d* states with a small contribution from the non-metal *p* states. According to the figure 2, during growth of Nb-doped $MoS_2$, the niobium transition ion can interfere between two layer, according to the weak van der Waals forces which link them together. This well known process involves a reduction in stoichiometry, distortion of the crystal structure and/or a variation in the position of the Fermi level. The sandwich Nb ions creates stronger bonds than the original van der Waals forces and converts the two-dimensional structure $MoS_2$ (2H-$MoS_2$) of the compound into a three-dimension structure $MoS_2$ (3R-$MoS_2$). It is very likely that Nb ions stabilize the 3R polytype of $MoS_2$. The resulting van der Waals forces of 3R-$MoS_2$ should be weaker than the 2H polytype and this is reflected by the measured reduction in $\Delta_{BA}$.

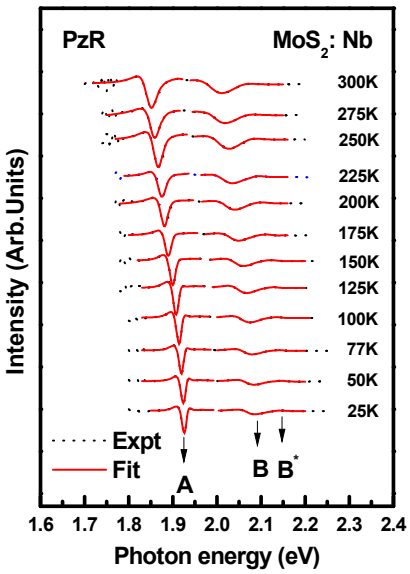


**Figure.2**. Piezoreflectance spectra of Nb-doped $MoS_2$ at several temperatures between 25 and 300 K. The dashed curves are the experimental results and the solid curves are least squares fits of Eq. (1).

**Table.1** Energies of the excitons A, B and their splitting in $MoS_2$, $MoS_2$:Au using equation (1). Relevant values for previously works are included for comparison.

| Material | A (eV) | B (eV) | $E_{A-B}$ (eV) | Temperature (K) |
|---|---|---|---|---|
| $MoS_2$:Nb [a] | 1.928 ± 0.005 | 2.167 ± 0.008 | 0.157 ± 0.013 | 25 |
| | 1.920 ± 0.005 | 2.160 ± 0.008 | 0.159 ± 0.005 | 77 |
| | 1.852 ± 0.008 | 2.086 ± 0.01 | 0.160 ± 0.018 | 300 |
| $MoS_2$:Re [b] | 1.915 | 2.066 | 0.151 | 15 |
| Undoped $MoS_2$ [b] | 1.928 | 2.136 | 0.208 | 15 |
| $MoS_2$ [c] | 1.88 | 2.06 | 0.18 | 300 |
| $MoS_2$ [d] | 1.9255 | 2.137 | 0.2115 | 4.2 |
| $MoS_2$ [e] | 1.92 | 2.124 | 0.204 | 4.2 |
| $MoS_2$ [f] | 1.929 ± 0.005 | 2.136 ± 0.008 | 0.207 ± 0.013 | 25 |
| | 1.845 ± 0.008 | 2.053 ± 0.01 | 0.208 ± 0.018 | 300 |
| 2H-$MoS_2$ [g] | 1.910 | 2.112 | 0.202 | 5 |
| 3R-$MoS_2$ [g] | 1.908 | 2.057 | 0.149 | 5 |

[a]Present work.
[b]PzR [31].
[c]Reflectance [33].
[d]WMR [30].
[e]Photoconductivity [30].
[f]PzR [32].
[g]Transmission [29].

## 4. Summary

In summary we have measured the temperature dependence of the energies and broadening parameters of the direct band-edge excitonic transitions of Nb-doped $MoS_2$ using PzR in the temperature range 25 to 300 K. From the experimental observations and detailed analysis of

the broadening parameters and energies of the excitonic features A and B, we can infer that the Nb ions are most likely intercalated between the van der Waals gap and stabilize the rhombohedral 3R phase of the $MoS_2$ crystal instead of forming the ternary $Mo_{1-x}Nb_xS_2$ system. As a result the electronic states of the $MoS_2$ crystals are modified with a reduction of energy splitting of A and B excitons.

**Acknowledgements**
The authors would like to acknowledge Professor Ying-Sheng Huang and Professor Ching-Hwa Ho for advising and providing materials and experimental equipment at Semiconductor Characterization Laboratory, National Taiwan University of Science and Technology (NTUST).

**References**
[1] Wilson J A and Yoffe A D (1969), *Adv. Phys*. **18**, 193
[2] Chang, Y. H. et al. (2013) Highly Efficient Electrocatalytic Hydrogen Production by MoSx Grown on Graphene-Protected 3D Ni Foams. Adv Mater 25, 756–760.
[3] Li, Y. et al. (2011) MoS2 Nanoparticles Grown on Graphene: An Advanced Catalyst for the Hydrogen Evolution Reaction. J Am Chem Soc 133, 7296–7299.
[4] Kong, D. et al. (2013) Synthesis of $MoS_2$ and $MoSe_2$ Films with Vertically Aligned Layers. Nano Lett 13, 1341–1347.
[5] Kam K K and Parkinson B A, (1982) *J. Phys. Cem*. **86**, 463.
[6] Li S J, Bernede J C, Pouzet J and Jamali M, (1996) *J. Phys.: Condens. Matter* **8**, 2291
[7] Shi, Y. et al. (2012) van der Waals Epitaxy of $MoS_2$ Layers Using Graphene As Growth Templates. Nano Lett 12, 2784–2791.
[8] Liu, K.-K. et al. (2012) Growth of Large-Area and Highly Crystalline $MoS_2$ Thin Layers on Insulating Substrates. Nano Lett 12, 1538–1544.
[9] Lin, Y.-C. et al. (2012) Wafer-scale $MoS_2$ thin layers prepared by $MoO_3$ sulfurization. Nanoscale 4, 6637-6641.
[10] Lee, Y.-H. et al. (2012) Synthesis of Large-Area $MoS_2$ Atomic Layers with Chemical Vapor Deposition. Adv Mater 24, 2320–2325.
[11] Zhan, Y., Liu, Z., Najmaei, S., Ajayan, P. M. & Lou, J. (2012) Large-Area Vapor-Phase Growth and Characterization of $MoS_2$ Atomic Layers on a SiO2 Substrate. Small 8, 966–971.
[12] D. S. Ginley, R. M. Biefeld, B. A. Parkinson and K. Keung-Kam, (1982) J. Electrochem. Soc., 129 145.
[13] A. Casalot, M. Chaouch and G. Vacquier, Ann. (1986) ('him.Fr., 11 509.
[14] Radisavljevic, B., Radenovic, A., Brivio, J., Giacometti, V. & Kis, A. (2011) Single-layer MoS2 transistors. Nat Nano 6, 147–150.
[15] Lembke, D. & Kis, A. (2012) Breakdown of High-Performance Monolayer $MoS_2$ Transistors. ACS Nano 6, 10070–10075.
[16] Wang, H. et al. (2012) Integrated Circuits Based on Bilayer $MoS_2$ Transistors. Nano Lett 12, 4674–4680.
[17] Eda, G. et al. (2011) Photoluminescence from Chemically Exfoliated $MoS_2$. Nano Lett 11, 5111–5116.
[18] Splendiani, A. et al. (2010) Emerging Photoluminescence in Monolayer $MoS_2$. Nano Lett 10, 1271–1275.
[19] R. Murray, B.L. Evans, (1979) J. Appl. Crystallogr. **12** 312.

[20] Clark A H 1970 N. Jahrbuchf. Mineral. Monatsheffe **3** 33
[21] J. B Legma, G. Vacquier, Traorè and A. casalot, 1991 Mater. Sci. Eng. B **8** 167.
[22] Mathieu H, Allegre J and Gil B, (1991) *Phys. Rev*. B **43**, 2218
[23] Pollak F H and Shen H, (1993) *Mater. Sci. Eng*. R **10**, 275
[24] Aspnes D E 1980 *Optical Properties of Semiconductors (Handbook on Semiconductors 2)* ed M Balkanski (Amsterdam: North-Holland) p 109
[25] Varnish Y P, (1967) *Physica* **34**, 149
[26] Lantenschlager P, Garriga M, Logothetidis S and Cardona M, (1987) *Phys. Rev*. B **35**, 9178
[27] Lantenschlager P, Garriga M, Vina L and Cardona M, (1987) *Phys. Rev*. B **36**, 4821
[28] Aspnes D E 1980 *Optical Properties of Semiconductors (Handbook on Semiconductors 2)* ed M Balkanski (Amsterdam: North-Holland) p 109
[29] Beal A R, Knights J C and Liang W Y, (1972) *J. Phys. C: Solid State Phys*. **5,** 3540
[30] Fortin E and Raga F, (1975) *Phys. Rev*. B **11**, 905
[31] Malikova L, Krystek W, Pollak F H, Dai N, Cavus A and Tamorgo M C, (1996) *Phys. Rev*. **B** 54, 1819
[32] Qiang H, Pollak F H, Sotomayor Torres C M, Leitch W, Kean A H, Stroscio M, Jafrate G J and Kim K W, (1992) *Appl. Phys. Lett*. **61**, 1411
[33] Beal A R, Liang W Y and Huges H P, (1976) *J. Phys. C: Solid State Phys*. **9,** 2449
[34] Coehoorn R, Haas C, Dickstra J, Flipse C J F, de Groot R A and Wold A, (1987) *Phys. Rev*. B **35**, 6195
[35] Coehoorn R, Haas C, and de Groot R A, (1987) *Phys. Rev*. B **35**, 6203
[36] Straub Th, Fauth K, Finteis Th, Hengsberger M, Claessen R, Steiner P, Hufner S and Blaha P, (1996) *Phys. Rev*. B **53**, 16152

*International Journal of Engineering & Technology*, 7 (2) (2018) 823-827

**International Journal of Engineering & Technology**

*Website: www.sciencepubco.com/index.php/IJET*

***Research paper***

# The Controller Design Using Local Stability Analysis on a Nonlinear Inverted Pendulum

**Timbang Pangaribuan[1, 2], Nasruddin MN[1], Eddy Marlianto[1], Mula Sigiro[3]**

[1]*Department of Physics, Faculty of Mathematics and Natural Science, Universitas Sumatera Utara, Medan, Indonesia*
[2]*Department of Electrical Engineering, Faculty of Engineering, Universitas HKBP Nommensen, Medan, Indonesia*
[3]*Department of Physics Education, Faculty of Teacher Training and Education, Universitas HKBP Nommensen, Medan, Indonesia*
**Corresponding author E-mail: timbang.pbn@gmail.com*

**Abstract**

This paper is designed for the purpose of analytic design and numerical simulation of a controller for nonlinear mobile inverted pendulum. It needs to obtain a method to overcome the difficulties in the design problem of controller for nonlinear plant. The method was using local stability analysis of two fixed points in two-dimensional ordinary nonlinear differential equation. The result provides a stable response solution using a special pole placement design, and transient stability is simulated using simulink. The response behavior can be selected according to the desired poles. The results obtained at this work are different from the optimal control problem. Indeed, our results have been summarized in the design method, target response and simulation process.

***Keywords:*** *analytic design, special pole placement, simulation, stable response*

## 1. Introduction

A nonlinear inverted pendulum model has dynamics with two movements, its angle and its wheel movements, as shown in Fig. 1. These dynamics[1]–[4] can be elaborated by two nonlinear second order differential equations shown with its arrangement as can be seen in equations (1) and (2).

$$\ddot{\theta}(t) = \frac{W\left(M_p\, g\, L\, \sin\theta - F\right) - Q\, \cos\theta \left(M_p\, L\, \dot{\theta}^2\, \sin\theta + \frac{1}{r}F\right)}{W\, P - Q^2\, \cos\theta^2} \quad (1)$$

$$\ddot{x}(t) = \frac{\left(M_p\, L\, \dot{\theta}^2\, \sin\theta + \frac{1}{r}F\right) P - \left(M_p\, g\, L\, \sin\theta - F\right) Q\, \cos\theta}{W\, P - Q^2\, \cos\theta^2} \quad (2)$$

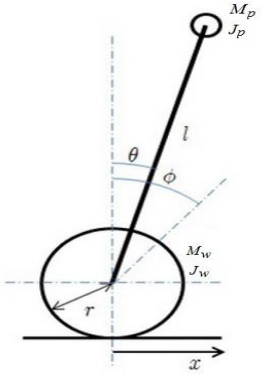


Fig. 1. Model of Inverted Pendulum

Both equations use three parameters can be seen in equation (3).

$$W = M_w + M_p + \frac{J_w}{r^2}, = J_p + M_p\, L^2\, , Q = M_p\, L \quad (3)$$

$\theta$ is the position of pendulum; $x$ is the position of the wheel. The initial position of pendulum was $\theta = \theta_0$ in the unit (rad), the initial position of the wheel with $x = x_0 = 0$ in the unit (m). The parameters $M_w$ and $M_p$ are respectively by the mass of the wheel and the pendulum in the unit (kg), and $g$ = 9.81 (m/s$^2$) is the graffiti acceleration. To do the simulation it needs the parameters: $L$ = 0.6 m, $M_p$ = 1.6 kg, $M_w$ = 1.551 kg, $J_w$ = 0.005 kg-m$^2$, $J_p$ = 0.027 kg-m$^2$, $r$ = 0.2 m[1].

The equations (1) and (2) can be modeled in the state space equation. It chooses four states, where, $x_1 = \theta, x_2 = \dot{\theta}, x_3 = x, x_4 = \dot{x}$. Based on equations (1) and (2) have been formed the state space equation (4) below[5]:

$$\begin{aligned}
\dot{x}_1 &= x_2 \\
\dot{x}_2 &= \frac{W\, Q\, g\, \sin x_1 - Q^2\, x_2{}^2 \sin x_1 \cos x_1 - \left(W + \frac{Q}{r}\cos x_1\right)F}{W\, P - Q^2\, \cos x_1{}^2} \\
\dot{x}_3 &= x_4 \\
\dot{x}_4 &= \frac{PQ\, x_2{}^2 \sin x_1 - Q^2 g\, \sin x_1 \cos x_1 + \left(\frac{P}{r} + Q\cos x_1\right)F}{W\, P - Q^2\, \cos x_1{}^2}
\end{aligned} \quad (4)$$

The behavior of the open loop inverted pendulum has been simulated using matlab-simulink[6]–[8], as shown in Fig. 2.

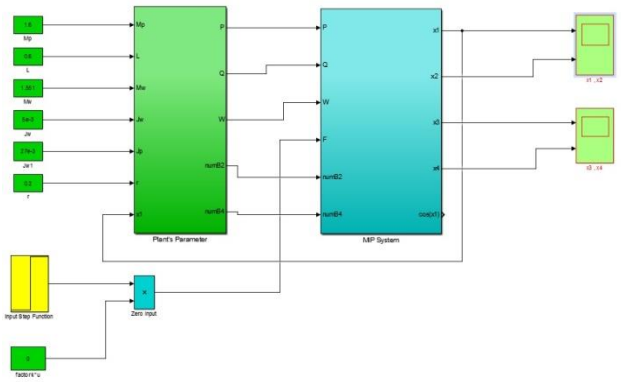

**Fig 2.** The Simulation of Open Loop System

The responses can be seen on Figs. 3 and 4. All the responses are oscillation and make the system unstable. The characteristic of the open loop system equation (4) include damping factor and natural frequency cannot be explained analytically because both these dynamics are nonlinear.

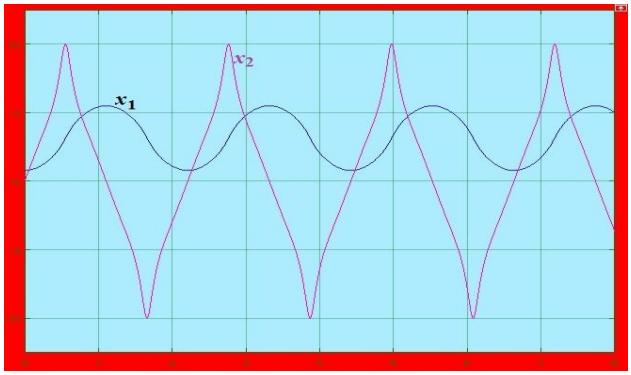


**Fig 3.** Response of $\theta(t)$ and $\dot{\theta}(t)$ on Open Loop System

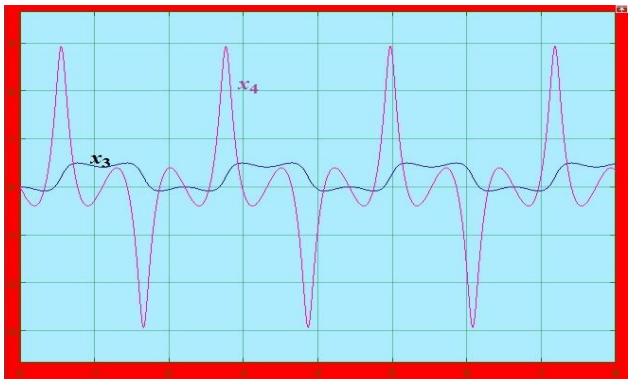


**Fig 4.** Response of $x(t)$ and $\dot{x}(t)$ on Open Loop System

To stabilize all the responses of the open-loop system it needs the state feedback. It is difficult to design feedback as a linear plant. First it needs a way to do the process for linearization of system dynamics. The local stability analysis method can be developed in model of open loop system; furthermore it needs to apply the pole assignment or pole placement to the local stability analysis.

## 2. Local Stability Analysis

The local stability analysis of fixed points in two-dimensional nonlinear ordinary differential equations such as equations (1) and (2), it is based on approximating the nonlinear equation with linear equation (5) in the following below[9]–[11]:

$$\frac{dx}{dt} = f_1(x,u), \frac{du}{dt} = f_2(x,u) \quad (5)$$

Let is assumed that there is a fixed point ($x^*$, $u^*$) for which $f_1(x^*, u^*) = f_2(x^*, u^*) = 0$, occurs on the plant. The linear analysis involves to carry out a Taylor expansion of the nonlinear functions in $f_1(x,u)$ and $f_2(x,u)$ in the neighborhood of form $f(x^*, u^*)$, as can be seen in the following below:

$$f(x,u) = f(x^*,u^*) + \frac{\partial f}{\partial x}|_{(x^*,u^*)}(x-x^*) + \frac{\partial f}{\partial u}|_{(x^*,u^*)}(u-u^*) + \dots \quad (6)$$

Based on equation (6), it can be defined:

$$X = x - x^*, U = u - u^* \quad (7)$$

Then it can expand equation (6) become,

$$\frac{dX}{dt} = A\,X + B\,U + \cdots\ , \quad \frac{dU}{dt} = C\,X + D\,U + \cdots \quad (8)$$

The equation (8) needs two functions $f_1$ and $f_2$ related to equations (1) and (2) in the form of equation (6), then it found:

$$A = \frac{df_1}{dx}|_{(x^*,u^*)}, B = \frac{df_1}{dy}|_{(x^*,u^*)}, C = \frac{df_2}{dx}|_{(x^*,u^*)},$$
$$D = \frac{df_2}{dy}|_{(x^*,u^*)} \quad (9)$$

In the first order of differential equation, the nonlinear form of equation (8) can be approximated by a linear equation (10),

$$\frac{dX}{dt} = A\,X + B\,Y\ , \quad \frac{dU}{dt} = C\,X + D\,Y \quad (10)$$

The poles of the linear approximation in equation (10) will be found with the formula below[5]:

$$M = \begin{bmatrix} A & B \\ C & D \end{bmatrix} \quad (11)$$

It found the poles $\mu_1$ and $\mu_2$ in equation (11), these are,

$$|\mu I - M| = \begin{vmatrix} \mu - A & -B \\ -C & \mu - D \end{vmatrix} = 0 \quad (12)$$

After taking determine of equation (12), both of the poles have equation as can be seen in the following below:

$$\mu_1 = \frac{A+D}{2} + \frac{\sqrt{(A-D)^2+4\,BC}}{2}$$
$$\mu_2 = \frac{A+D}{2} - \frac{\sqrt{(A-D)^2+4\,BC}}{2} \quad (13)$$

If the result of equation (13) has the real part with $\mu_1 < 0$ and $\mu_2 < 0$, the system is called stable and the responses of the system has steady-state value.

## 3. The Special Pole Placement

Based on the dynamics of nonlinear plant equation (1) and (2), it needs equation (9) and (10) to generate the linear form of nonlinear plant. Furthermore, it found the dynamics of nonlinear plant has changed into the linear equation, and the process of pole placement is explained with some steps in the following below. First, the four states have defined in equation (4), those are:

$$x_1 = \theta, x_2 = \dot{\theta}, x_3 = x, x_4 = \dot{x} \quad (14)$$

Second, refers to equation (6), it needs to make both equations (1) and (2) become $f_1$ and $f_2$. By using equations (9) and (10), it found all parameters for equation (11) as shown below:

$$A_{11} = \frac{\partial f_1}{\partial x_1}|_{(x_1,x_2,x_3,x_4,F)}, A_{12} = \frac{\partial f_1}{\partial x_2}|_{(x_1,x_2,x_3,x_4,F)},$$

$$A_{13} = \frac{\partial f_1}{\partial x_3}|_{(x_1,x_2,x_3,x_4,F)}, A_{14} = \frac{\partial f_1}{\partial x_4}|_{(x_1,x_2,x_3,x_4,F)},$$

$$A_{21} = \frac{\partial f_2}{\partial x_1}|_{(x_1,x_2,x_3,x_4,F)}, A_{22} = \frac{\partial f_2}{\partial x_2}|_{(x_1,x_2,x_3,x_4,F)}$$

$$A_{23} = \frac{\partial f_2}{\partial x_3}|_{(x_1,x_2,x_3,x_4,F)}, A_{24} = \frac{\partial f_2}{\partial x_4}|_{(x_1,x_2,x_3,x_4,F)},$$

$$C_{11} = \frac{\partial f_3}{\partial x_1}|_{(x_1,x_2,x_3,x_4,F)}, C_{12} = \frac{\partial f_3}{\partial x_2}|_{(x_1,x_2,x_3,x_4,F)},$$

$$C_{13} = \frac{\partial f_3}{\partial x_3}|_{(x_1,x_2,x_3,x_4,F)}, C_{14} = \frac{\partial f_3}{\partial x_4}|_{(x_1,x_2,x_3,x_4,F)},$$

$$C_{21} = \frac{\partial f_4}{\partial x_1}|_{(x_1,x_2,x_3,x_4,F)}, \; C_{22} = \frac{\partial f_4}{\partial x_2}|_{(x_1,x_2,x_3,x_4,F)}$$

$$C_{23} = \frac{\partial f_4}{\partial x_3}|_{(x_1,x_2,x_3,x_4,F)}, C_{24} = \frac{\partial f_4}{\partial x_4}|_{(x_1,x_2,x_3,x_4,F)}$$

$$B_1 = \frac{\partial f_1}{\partial F}|_{(x_1,x_2,x_3,x_4,F)}, B_2 = \frac{\partial f_2}{\partial F}|_{(x_1,x_2,x_3,x_4,F)}$$

$$D_1 = \frac{\partial f_1}{\partial F}|_{(x_1,x_2,x_3,x_4,F)}, D_2 = \frac{\partial f_2}{\partial F}|_{(x_1,x_2,x_3,x_4,F)} \quad (15)$$

Third, if equation (15) is applied to equation (10) then it found equation (16) in the following below:

$$\begin{bmatrix} \dot{x_1} \\ \dot{x_2} \\ \dot{x_3} \\ \dot{x_4} \end{bmatrix} = \begin{bmatrix} A_{11} & A_{12} & A_{13} & A_{14} \\ A_{21} & A_{22} & A_{23} & A_{24} \\ C_{11} & C_{12} & C_{13} & C_{14} \\ C_{21} & C_{22} & C_{23} & C_{24} \end{bmatrix} \begin{bmatrix} x_1 \\ x_2 \\ x_3 \\ x_4 \end{bmatrix} + \begin{bmatrix} B_1 \\ B_2 \\ D_1 \\ D_2 \end{bmatrix} F \quad (16)$$

To stabilize the system equation (16) it needed the feedback $F(t)$ with equation (17) in the following below[5], [12]–[14]:

$$F(t) = v(t) - K\, x(t) \quad (17)$$

Where $K = [K_1\ K_2\ K_3\ K_4]$, and $v(t)$ is the reference input to the system

This process didn't use the Riccati's equation to design the optimal feedback, but it used special pole placement method and chooses four the stable desired poles.

Furthermore, equations (15) and (16) has been completed with the fixed point $x_1 = \pi/4$, $x_2 = 0$, $x_3 = 0$, and $x_4 = 0$, it found the parameters,

$$A_{11} = 0\ ,\ A_{12} = 1\ ,\ A_{13} = 0\ ,\ A_{14} = 0$$

$$A_{21} = \frac{W\, M_p\, g\, L \sin(\frac{\pi}{4})}{W\, P - Q^2\,(\cos(\frac{\pi}{4}))^2}\ , A_{22} = 0\ \ , A_{23} = 0\ ,\ A_{24} = 0$$

$$A_{11} = 0\ ,\ A_{12} = 0\ ,\ A_{13} = 0\ ,\ A_{14} = 1$$

$$A_{41} = \frac{-M_p\, g\, L\, Q \sin\left(\frac{\pi}{4}\right)\cos\left(\frac{\pi}{4}\right)}{W\, P - Q^2\,(\cos(\frac{\pi}{4}))^2}\ , A_{42} = 0\ \ , A_{43} = 0\ ,\ A_{44} = 0\ B_1 =$$

$$0, B_2 = \frac{W + Q\cos(\frac{\pi}{4})/r}{W\, P - Q^2(\cos(\frac{\pi}{4}))^2},\ B_3 = 0, B_4 = \frac{P/r + Q\cos(\frac{\pi}{4})}{W\, P - Q^2(\cos(\frac{\pi}{4}))^2} \quad (18)$$

Now for the linearization system, equation (18) to equation (16) can be applied as written below:

$$\dot{x} = \begin{bmatrix} 0 & 1 & 0 & 0 \\ A_{21} & 0 & 0 & 0 \\ 0 & 0 & 0 & 1 \\ A_{41} & 0 & 0 & 0 \end{bmatrix} x + \begin{bmatrix} 0 \\ B_2 \\ 0 \\ B_4 \end{bmatrix} F, x = \begin{bmatrix} x_1 \\ x_2 \\ x_3 \\ x_4 \end{bmatrix} \quad (19)$$

Fourth, the next step was to perform the controller needed to stabilize the system. Define the desired closed loop system with four poles; those are $\mu_1$, $\mu_2$, $\mu_3$ and $\mu_4$. The characteristic equations to all poles are given in equation (20).

$$L(\mu) = (\mu + \mu_1)\,(\mu + \mu_2)\,(\mu + \mu_3)\,(\mu + \mu_4) \quad (20)$$

If the controller in equation (17) is substituted in equation (19), the closed loop equation can be found as below:

$$\dot{x} = \begin{bmatrix} 0 & 1 & 0 & 0 \\ A_{21} & 0 & 0 & 0 \\ 0 & 0 & 0 & 1 \\ A_{41} & 0 & 0 & 0 \end{bmatrix} x + \begin{bmatrix} 0 \\ B_2 \\ 0 \\ B_4 \end{bmatrix} [v - K_1\, x_1 - K_2\, x_2\ - K_3\, x_3 - K_4\, x_4] \quad (21)$$

Then the equation of closed loop system can be written down with equation (22) below:

$$\dot{x} = \begin{bmatrix} 0 & 1 & 0 & 0 \\ A_{21} - B_2\, K_1 & -B_2\, K_2 & -B_2\, K_3 & -B_2\, K_4 \\ 0 & 0 & 0 & 1 \\ A_{41} - B_4\, K_1 & -B_4\, K_2 & -B_4 K_3 & -B_4\, K_4 \end{bmatrix} x + \begin{bmatrix} 0 \\ B_2 \\ 0 \\ B_4 \end{bmatrix} r \quad (22)$$

In general form, the equation (22) can be written with equation (23) below:

$$\dot{x} = A_{CL}\, x + \ B_{CL}\, r \quad (23)$$

Where,

$$A_{CL} = \begin{bmatrix} 0 & 1 & 0 & 0 \\ A_{21} - B_2\, K_1 & -B_2\, K_2 & -B_2\, K_3 & -B_2\, K_4 \\ 0 & 0 & 0 & 1 \\ A_{41} - B_4\, K_1 & -B_4\, K_2 & -B_4\, K_3 & -B_4\, K_4 \end{bmatrix},$$

$$B_{CL} = \begin{bmatrix} 0 \\ B_2 \\ 0 \\ B_4 \end{bmatrix} \quad (24)$$

Finally the value for the special pole placement for state feedback should be found as $K = [K_1\ K_2\ K_3\ K_4]$ with the procedure below:

First, it needs to elaborate the equation (20) to find the characteristic equation below:

$$L(\mu) = \mu^4 + m_3\, \mu^3 + m_2\, \mu^2 + m_1\, \mu + m_0 \quad (25)$$

Where,

$m_3 = \mu_1 + \mu_2 + \mu_3 + \mu_4$

$m_2 = \mu_1\, \mu_2 + \mu_1\, \mu_3 + \mu_1\, \mu_4 + \mu_2\, \mu_3 + \mu_2\, \mu_4 + \mu_3\, \mu_4$

$m_1 = \mu_1\, \mu_2\, \mu_3 + \mu_1\, \mu_2\, \mu_4 + \mu_1\, \mu_3\, \mu_4 + \mu_2\, \mu_3\, \mu_4$

$m_0 = \mu_1\, \mu_2\, \mu_3\, \mu_4$

Next, the characteristic equation of the closed loop system in the equation (24) was found with equation below:

$$|\ \mu\ I - A_{CL}\ | = 0 \quad (26)$$

The determinant of equation (26) gave the characteristic equation was shown in equation (27) below:

$$L_{CL}(\mu) = \mu^4 + \ [B_4\, K_4 + B_2\, K_2]\ \mu^3 + \ [B_4\, K_3 + B_2\, K_1 - A_{21}]\ \mu^2 + [A_{41}\, B_2 - A_{21}\, B_4]\ K_4\ \mu + \ [A_{41}\, B_2 - A_{21}\, B_4]\ K_3 \quad (27)$$

To find the special feedback $K = [K_1\ K_2\ K_3\ K_4]$, the equation (27) must be equal to equation (25). If both equations are equal, it found these four equations below:

$$\begin{aligned} B_4\, K_4 + B_2\, K_2 &= m_3 \\ B_4\, K_3 + B_2\, K_1 - A_{21} &= m_2 \\ [A_{41}\, B_2 - A_{21}\, B_4]\ K_4 &= m_1 \\ [A_{41}\, B_2 - A_{21}\, B_4]\ K_3 &= m_0 \end{aligned} \quad (28)$$

By using the analytical process in equation (28), finally the equation to obtain the value of $K$ by the four equations was obtained below:

$$K_3 = \frac{m_0}{A_{41}\,B_2 - A_{21}\,B_4}$$

$$K_4 = \frac{m_1}{A_{41}\,B_2 - A_{21}\,B_4}$$

$$K_2 = \frac{m_3 - B_4\,K_4}{B_2}$$

$$K_1 = \frac{m_2 + A_{21} - B_4\,K_3}{B_2} \quad (29)$$

## 4. Simulation

Using the parameters of the open loop system in equations (18) and (19) it found the state-space equation below:

$$\begin{bmatrix}\dot{x_1}\\ \dot{x_2}\\ \dot{x_3}\\ \dot{x_4}\end{bmatrix} = \begin{bmatrix}0 & 1 & 0 & 0\\ 6.2843 & 0 & 0 & 0\\ 0 & 0 & 0 & 1\\ -0.1200 & 0 & 0 & 0\end{bmatrix}\begin{bmatrix}x_1\\ x_2\\ x_3\\ x_4\end{bmatrix} + \begin{bmatrix}0\\ 1\\ 0\\ 1\end{bmatrix}F \quad (30)$$

It needs to choose four the desired poles refer to the equation (25) with the value in the following below:

$[\mu_1\ \mu_2\ \mu_3\ \mu_4] = [-3\ \ -3\ \ -3\ \ -3]$

By using equations (29) and (25) it found the value of state feedback in the following below:

$$K = [-170.2331 - 68.5773 - 99.3821 - 94.4130] \quad (31)$$

The state feedback can be written as in the following below:

$$F(t) = v(t) - [k_1 \quad k_2 \quad k_3 \quad k_4]\,[x_1 \quad x_2 \quad x_3 \quad x_4]^T \quad (32)$$

By inserting $F(t)$ from the equation (32) to equation (30), the closed loop system has the result in the following below:

$$\begin{bmatrix}\dot{x_1}\\ \dot{x_2}\\ \dot{x_3}\\ \dot{x_4}\end{bmatrix} = \begin{bmatrix}0 & 1 & 0 & 0\\ 6.2843 & 0 & 0 & 0\\ 0 & 0 & 0 & 1\\ -0.1200 & 0 & 0 & 0\end{bmatrix}\begin{bmatrix}x_1\\ x_2\\ x_3\\ x_4\end{bmatrix} - \begin{bmatrix}0\\ 1\\ 0\\ 1\end{bmatrix}[k_1\ \ k_2\ \ k_3\ k_4]\begin{bmatrix}x_1\\ x_2\\ x_3\\ x_4\end{bmatrix} + \begin{bmatrix}0\\ 1\\ 0\\ 1\end{bmatrix}v(t) \quad (33)$$

Finally, with the input $v(t) = 0$, the equation (33) can be applied to the nonlinear system in equations (1) and (2) as in the following below:

$$\ddot{\theta}(t) = \frac{WM_pgL\sin\theta - QM_pL\,\dot{\theta}^2\sin\theta\cos\theta - \left(W + \frac{Q\cos\theta}{r}\right)\left[-k_1\,\theta - k_1\dot{\theta} - k_3\,x - k_4\,\dot{x}\right]}{WP - Q^2\cos\theta^2} \quad (34)$$

$$\ddot{x}(t) = \frac{PM_pL\dot{\theta}^2\sin\theta - QM_pgL\sin\theta\cos\theta + \left(\frac{P}{r} + Q\cos\theta\right)\left[-k_1\,\theta - k_1\dot{\theta} - k_3\,x - k_4\,\dot{x}\right]}{WP - Q^2\cos\theta^2} \quad (35)$$

To build the simulation using simulink diagram for the system with equations (34) and (35), it performed four sub-systems, as can be seen in Fig. 5.

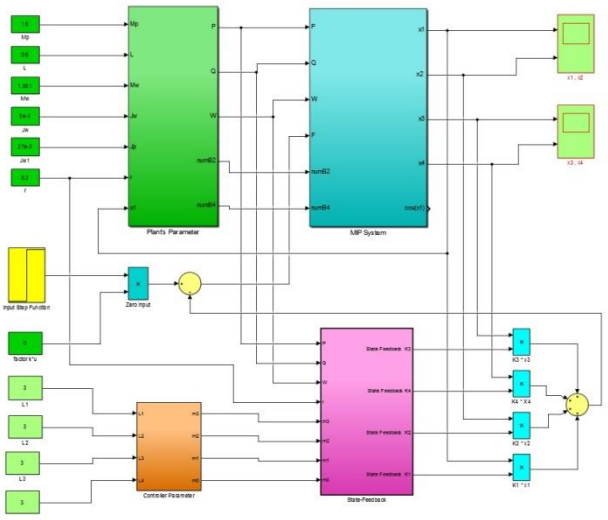


**Fig 5.** The Simulation of Closed Loop System

The sub-system consists of the plant's parameter, the nonlinear plant, the controller parameters and the state feedback as shown in Figs. 6 to 9.

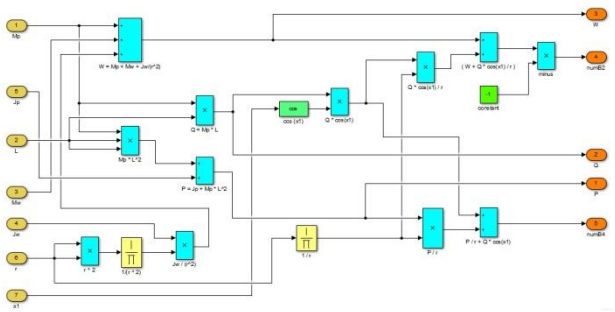

**Fig. 6.** The Plant's Parameter of Fig. 5

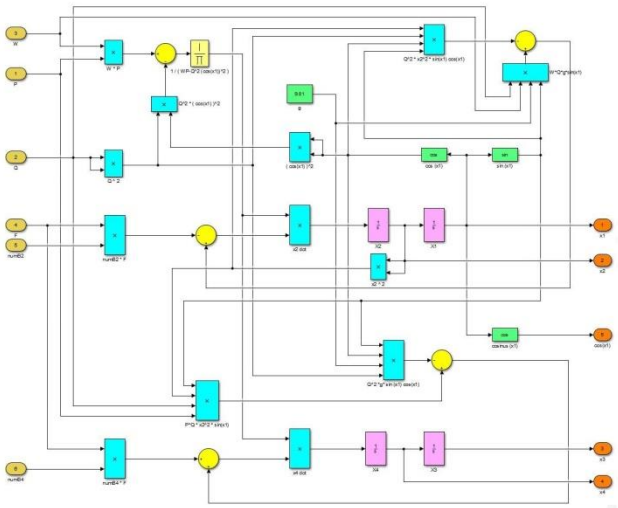

**Fig. 7.** The Nonlinear Plant of Fig. 5

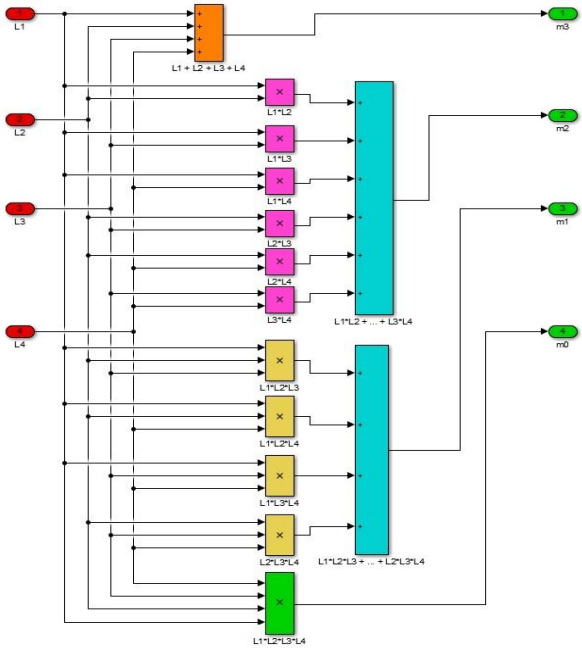


**Fig. 8.** The Controller Parameters of Fig. 5

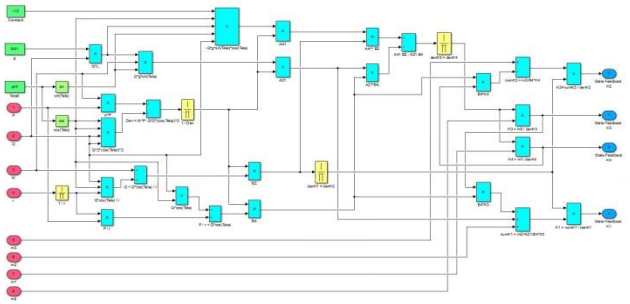

**Fig. 9.** The State Feedback of Fig. 5

There are two figures that captured by scope in the simulation, those are $x_1$, $x_2$ as can be seen in Fig. 10 and $x_3$, $x_4$ as can be seen in Fig. 11.

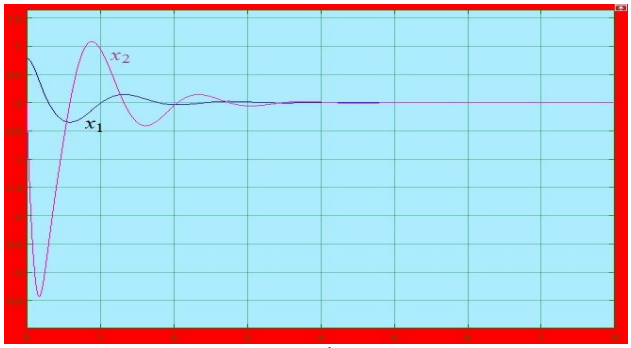


**Fig 10.** Response of $\theta(t)$ and $\dot{\theta}(t)$ on Closed Loop System

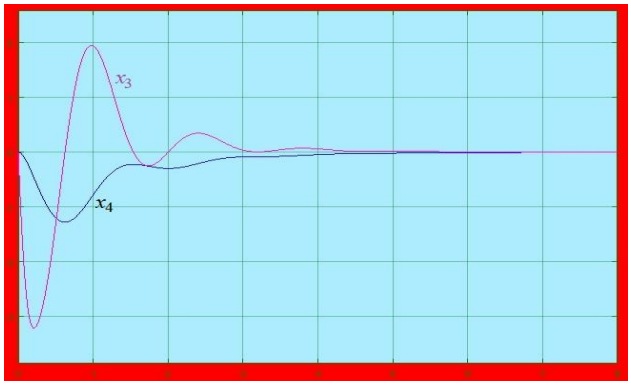


**Fig 11.** Response of $x(t)$ $\dot{x}(t)$ on Closed Loop System

Based on the results in Fig. 10 and 11, all the responses of the nonlinear plant will run toward stable with oscillation damped until the responses toward zero, and all the responses are eligible.

## 5. Conclusion

Based on the result, it can be described that responses of linearization of the nonlinear plant has been adequate. Then the controller has been produced for the nonlinear plant by using the local stability analysis. The process needed the special feedback pole placement method like equation (21) to (32) that should be applied at simulink process. Lastly, the controller has been simulated by using simulink techniques. All the behavior of the responses was stable revering to the poles given. The results of these responses on the Fig. 10 and 11 have been taken after choosing the best poles by the trial and error process..

## References

[1] K. K. and S. B. Kwak Sangfeel, Song Eunji, "Design of Fuzzy Logic Controller for Inverted Pendulum-type Mobile Robot using Smart In-Wheel Motor," *Indian J. Sci. Technol.*, vol. 8, no. April, pp. 493–503, 2015.

[2] Z.-Q. Guo, J.-X. Xu, and T. H. Lee, "Design and implementation of a new sliding mode controller on an underactuated wheeled inverted pendulum," *J. Franklin Inst.*, vol. 351, no. 4, pp. 2261–2282, 2014.

[3] F. Grasser, A. D'Arrigo, S. Colombi, and A. C. Rufer, "JOE: A mobile, inverted pendulum," *IEEE Trans. Ind. Electron.*, vol. 49, no. 1, pp. 107–114, 2002.

[4] T. Pangaribuan, M. N. Nasruddin, E. Marlianto, and M. Sigiro, "The influences of load mass changing on inverted pendulum stability based on simulation study," in *IOP Conference Series: Materials Science and Engineering*, 2017, vol. 237, no. 1.

[5] K. Ogata, *Modern control engineering*. Prentice-Hall, 2010.

[6] A. Morgado, V. J. Rivas, R. del Río, R. Castro-López, F. V. Fernández, and J. M. de la Rosa, "Behavioral modeling, simulation and synthesis of multi-standard wireless receivers in MATLAB/SIMULINK," *Integr. VLSI J.*, vol. 41, no. 2, pp. 269–280, Feb. 2008.

[7] Y. Zhan and J. A. Clark, "A search-based framework for automatic testing of MATLAB/Simulink models," *J. Syst. Softw.*, vol. 81, no. 2, pp. 262–285, Feb. 2008.

[8] C. Pan and Y. Guo, "Design and simulation of ex-range gliding wing of high altitude air-launched autonomous underwater vehicles based on SIMULINK," *Chinese J. Aeronaut.*, vol. 26, no. 2, pp. 319–325, Apr. 2013.

[9] J. M. Ramirez, F. V. Arroyave, and R. E. Correa Gutierrez, "Transient stability improvement by nonlinear controllers based on tracking," *Int. J. Electr. Power Energy Syst.*, vol. 33, no. 2, pp. 315–321, 2011.

[10] Y. Yuan and H. Liu, "An iterative updating method for damped structural systems using symmetric eigenstructure assignment," *J. Comput. Appl. Math.*, vol. 256, pp. 268–277, 2014.

[11] D. Kaplan and L. Glass, *Understanding nonlinear dynamics*. Springer-Verlag, 1995.

[12] S. Bezzaoucha, B. Marx, D. Maquin, and J. Ragot, "State constrained tracking control for nonlinear systems," *J. Franklin Inst.*, vol. 352, no. 7, pp. 2866–2886, Jul. 2015.

[13] L. Maniar, M. Oumoun, and J.-C. Vivalda, "On the stabilization of quadratic nonlinear systems," *Eur. J. Control*, vol. 35, pp. 28–33, May 2017.

[14] C.-F. Lin, *Advanced control systems design*. PTR Prentice Hall, 1994.